

# The Greenland ice sheet in a warming climate

De Groenlandse ijskap in een opwarmend klimaat

(met een samenvatting in het Nederlands)

**PROEFSCHRIFT**

ter verkrijging van de graad van doctor aan de Universiteit Utrecht op  
gezag van de rector magnificus, prof. dr. G.J. van der Zwaan,  
ingevolge het besluit van het college voor promoties in het openbaar te  
verdedigen op

woensdag 6 november 2013 des middags te 2.30 uur

door

**Jan Henk van Angelen**

geboren op 15 mei 1983 te Utrecht

Promotor: Prof. dr. M.R. van den Broeke  
Co-promotor: Dr. W.J. van de Berg

Copyright © 2013, J.H. van Angelen, Utrecht, The Netherlands

Typeset in L<sup>A</sup>T<sub>E</sub>X

Cover design Rens Batist

Printed by proefschriftmaken.nl, Uitgeverij BOXPress

ISBN 978-90-8891-720-2

Institute for Marine and Atmospheric research Utrecht (IMAU)  
Department of Physics, Faculty of Science, Utrecht University

Financial support was provided by funding from the ice2sea programme from the European Union 7th Framework Programme, grant number 226375, en het Nederlands Polair Programma (NPP) van de Nederlandse Organisatie voor Wetenschappelijk Onderzoek (NWO).

We cannot change the weather, we are changing the climate.



# Contents

---

<b>Samenvatting</b>	<b>ix</b>
<b>1 Arctic climate</b>	<b>1</b>
1.1 Background . . . . .	1
1.1.1 Arctic sea ice . . . . .	2
1.2 The Greenland ice sheet . . . . .	4
1.2.1 Mass Balance . . . . .	5
1.2.2 Contemporary GrIS mass balance . . . . .	7
1.3 Regional Atmospheric Climate Models . . . . .	8
1.4 This thesis . . . . .	9
<b>2 Momentum budget of the atmospheric boundary layer over the Greenland ice sheet and its surrounding seas</b>	<b>13</b>
2.1 Introduction . . . . .	14
2.2 Methods . . . . .	15
2.2.1 Model and evaluation . . . . .	15
2.2.2 Momentum budget . . . . .	16
2.2.3 Data analysis . . . . .	17
2.3 Results: winter . . . . .	19
2.3.1 Pressure, wind and temperature . . . . .	19
2.3.2 Momentum budget . . . . .	20
2.3.3 Northern Transect . . . . .	23
2.4 Results: summer . . . . .	27
2.4.1 Pressure, wind and temperature . . . . .	27
2.4.2 Momentum budget . . . . .	30
2.4.3 Northern transect . . . . .	30
2.5 Conclusions . . . . .	31
<b>3 The Greenland Sea Jet: A mechanism for wind-driven sea ice export through Fram Strait</b>	<b>35</b>

## Table of contents

---

3.1	Introduction . . . . .	36
3.2	Methods . . . . .	37
3.2.1	Data . . . . .	37
3.2.2	Momentum Budget . . . . .	38
3.3	Results . . . . .	39
3.3.1	Vertical Profiles . . . . .	39
3.3.2	Momentum Budget . . . . .	39
3.3.3	Sea Ice Area Flux Through FS . . . . .	41
3.3.4	Temporal Variability . . . . .	42
3.4	Conclusions . . . . .	43
<b>4</b>	<b>Sensitivity of Greenland ice sheet surface mass balance to surface albedo parameterization: a study with a regional climate model</b>	<b>47</b>
4.1	Introduction . . . . .	48
4.2	Data and methods . . . . .	49
4.2.1	AWS Observations . . . . .	49
4.2.2	Melt days . . . . .	49
4.2.3	Regional Atmospheric Climate Model . . . . .	49
4.2.4	Albedo parameterization . . . . .	51
4.2.5	MODIS background ice albedo . . . . .	54
4.2.6	Model experiments . . . . .	55
4.3	Results . . . . .	55
4.3.1	Albedo time series . . . . .	55
4.3.2	SMB components . . . . .	58
4.3.3	SMB along the K-transect . . . . .	63
4.4	Summary and Conclusions . . . . .	63
<b>5</b>	<b>Contemporary (1960-2012) evolution of the climate and surface mass balance of the Greenland ice sheet</b>	<b>67</b>
5.1	Introduction . . . . .	68
5.2	Data . . . . .	69
5.2.1	Regional Atmospheric Climate Model (RACMO2) . . . . .	69
5.2.2	Automatic Weather Station . . . . .	70
5.2.3	GRACE . . . . .	70
5.3	Model evaluation using GRACE . . . . .	71
5.4	Atmospheric circulation and GrIS temperature . . . . .	73
5.5	Surface Energy Balance . . . . .	77
5.6	Surface mass balance . . . . .	79

---

5.6.1	Melt duration . . . . .	79
5.6.2	Surface mass balance components . . . . .	81
5.7	Conclusions . . . . .	86
<b>6</b>	<b>Rapid loss of firn pore space accelerates 21st century Greenland mass loss</b>	<b>89</b>
6.1	Introduction . . . . .	90
6.2	Methods . . . . .	90
6.2.1	21st century scenario . . . . .	90
6.2.2	Regional atmospheric climate model RACMO2 . . . . .	92
6.3	Model evaluation . . . . .	95
6.4	Results . . . . .	98
6.4.1	Temperature and circulation . . . . .	98
6.4.2	Surface energy balance . . . . .	99
6.4.3	Surface mass balance . . . . .	102
6.5	Conclusions . . . . .	106
<b>7</b>	<b>Conclusions, ongoing and future work</b>	<b>111</b>
7.1	General conclusions . . . . .	112
7.2	Case study: the Greenland firn aquifer . . . . .	113
7.3	Future work . . . . .	116
	<b>Bibliography</b>	<b>119</b>
	<b>Publications</b>	<b>129</b>
	<b>Dankwoord</b>	<b>133</b>
	<b>Curriculum vitae</b>	<b>137</b>





# Samenvatting

---

De barre omstandigheden in het noordpoolgebied maken het één van de dunst bevolkte gebieden op aarde. Desalniettemin vormt het in het klimaatsysteem van het noordelijk halfrond een belangrijke component. De Arctische Oceaan beslaat het grootste deel van het noordpoolgebied, omgeven door land met de uitzondering van de open verbinding naar de Atlantische (Framstraat) en Grote Oceaan (Beringstraat). De poolcirkel ( $\sim 67^\circ\text{N}$ ), waar ten noorden de zon in de zomer niet ondergaat, wordt vaak gezien als de grens van het noordpoolgebied. Klimatologisch is dat echter de 10 graden juli isotherm. De grote variabiliteit in zonne-instraling zorgt voor een sterke seizoenscyclus in het Arctisch klimaat. Ondanks het gebrek aan zonne-energie in de winter blijven extreem lage temperaturen, vanwege de nabijheid van open oceaanwater en de lage ligging, meestal uit.

Sneeuw en ijs spelen een belangrijke rol in het klimaat van het noordpoolgebied, in de vorm van permafrost, de voor een groot deel van het jaar met zee-ijs bedekte Arctische Oceaan, vele gletsjers en de Groenlandse ijskap. De hoge mate waarin sneeuw en ijs zonlicht terugkaatsen, het zogenoemde albedo, geeft het klimaat van het noordpoolgebied een zeer sterke gevoeligheid. Verse sneeuw weerkaatst meer dan 80% van het zonlicht terug de ruimte in, terwijl vervuild ijs ongeveer 30% terugkaatst en oceaanwater nog maar  $<10\%$ .

Door de opwarming van de aarde is de zee-ijs bedekking met name in de zomer veel minder uitgestrekt dan drie decennia geleden. Tevens smelt het winter sneeuwdek vroeger in het seizoen. Als bijkomend effect wordt er dus meer zonne-energie geabsorbeerd, hetgeen de voornaamste oorzaak is dat het noordpoolgebied ongeveer twee keer zo snel opwarmt in vergelijking met het mondiale gemiddelde.

Centraal in dit proefschrift staat het klimaat van Groenland. Het grootste eiland op aarde ( $2,1$  miljoen  $\text{km}^2$ ) is voor 80% bedekt door de ijskap. Wanneer de ijskap in zijn geheel smelt, zal de zeespiegel gemiddeld met ongeveer 7 m stijgen. Door een hoogste punt van  $\sim 3200$  m heeft Groenland een sterke invloed op de atmosferische circulatie. Bovenop de ijskap blijft de temperatuur bijna het gehele jaar onder het vriespunt en de gemiddelde temperatuur neemt toe met afnemende hoogte richting de kust. Beneden de  $\sim 1500$  m is de ijskap gedurende de zomermaanden juni,

juli en augustus continu onderhevig aan smelt. Boven de sneeuwvrije toendra kan het in de zomer makkelijk opwarmen richting de 15 °C. Deze hoge temperaturen en bijkomende smelt vormen een schril contrast met het klimaat op Antarctica, waar het gedurende het gehele jaar diep winters is, met uitzondering van het Antarctisch Schiereiland. Dit grote verschil in klimaat tussen Groenland en Antarctica maakt dat Groenland veel gevoeliger is voor klimaatveranderingen.

Een belangrijk onderdeel in het klimaatsysteem is de massabalans van de Groenlandse ijskap, welke direct invloed heeft op de zeespiegel. De massabalans wordt bepaald door processen aan de bovenkant van de ijskap, de oppervlaktemassabalans (OMB), en door de hoeveelheid ijs die aan de rand van de ijskap via gletsjers afkalft. Accumulatie verminderd met sublimatie en smeltwater runoff geeft de OMB. Echter, andere processen zoals herbevrozing van smeltwater en sneeuwdrift (-sublimatie) spelen hierin een indirecte maar belangrijke rol. De oppervlakte energiebalans bepaalt de temperatuur van de bovenste sneeuw of ijslaag van de ijskap. Wanneer deze laag het smeltpunt bereikt, zal overtollige energie gebruikt worden voor smelten.

Het afgelopen decennium is de onzekerheid in schattingen van de massabalans van de Groenlandse ijskap, door de combinatie van verschillende en langere reeksen van satellietwaarnemingen en modelstudies, sterk verminderd. Zowel het afkalven van ijs als het smelten aan de bovenkant van de ijskap zijn de afgelopen jaren zeer sterk toegenomen. Dit heeft geresulteerd in een bijdrage aan de zeespiegelstijging van 0,4 mm per jaar gemiddeld over de afgelopen 20 jaar (~15% van de totale stijging).

Om het klimaat van Groenland en de OMB van 1960-2012 te analyseren is gebruik gemaakt van een regionaal atmosferisch klimaatmodel (RACMO2). Het model is feitelijk een weermodel, welke temperatuur, luchtdruk, wind en neerslag simuleert. De basis van RACMO2 is dan ook het Europese weermodel van het European Centre for Medium Range Weather Forecast (ECMWF). Aan de rand van het regionale domein wordt het model geforceerd door de toestand van de atmosfeer die op basis van observaties is bepaald. Om het klimaat boven Groenland realistisch te kunnen simuleren is het atmosferisch model gekoppeld aan een sneeuwmodel. De sneeuwroutine simuleert de bovenste meters van het sneeuw/ijspakket en berekent eigenschappen als temperatuur, dichtheid en het albedo. Naast het recente verleden is er met RACMO2 ook een toekomstsimulatie gedaan tot aan het eind van de 21e eeuw. RACMO2 wordt hierbij aangedreven door de resultaten van een mondiaal klimaatmodel.

In hoofdstuk 2 wordt aan de hand van impulsbehoud de optredende atmosferische circulatie boven de Groenlandse ijskap geanalyseerd. De circulatie rondom de ijskap kent drie belangrijke aandrijfmechanismen. Ten eerste de grootschalige forcering op basis van drukverschillen hoger in de atmosfeer welke over het algemeen een westelijke stroming genereren. De Groenlandse ijskap vormt een barrière in deze

---

westcirculatie, met als resultaat een hogedrukgebied als gevolg van de verticale compressie van de atmosfeer boven de ijskap. Dit leidt tot een meer zuid-westelijke stroming over de ijskap. Ten tweede de katabatische forcering, welke het gevolg is van het sterke afkoelende effect dat de ijskap op de atmosferische grenslaag heeft. De ontstane drukgradiënten in combinatie met de rotatie van de aarde genereren de persistente katabatische winden evenwijdig aan de hoogtelijnen. Over de westelijke en noordelijke helft van Groenland werken de grootschalige en katabatische forcering samen. Hier worden dan ook de sterkste winden waargenomen. Tenslotte is er de thermische forcering, welke ontstaat door temperatuur- en dus drukverschillen in de atmosferische grenslaag. Met name op de grens tussen de sneeuwvrije toendra en de ijskap kunnen in de zomer de temperatuurverschillen flink oplopen.

In hoofdstuk 3 wordt dieper ingegaan op de atmosferische circulatie boven de Groenland Zee ten oosten van Groenland. De circulatie wordt hier gekarakteriseerd door een persistente noord-zuid stroming als gevolg van temperatuurverschillen in de grenslaag. De grenslaag koelt boven het met zee-ijs bedekte westelijke deel van de Groenlandse zee af, terwijl deze boven het zee-ijs vrije oostelijke deel relatief warm blijft. Variabiliteit in de sterkte van deze ‘Groenlandse Zee Stroming’ is sterk gecorreleerd aan zee-ijs transport door Framstraat, welke het leeuwendeel van de zee-ijs export uit de Arctische Oceaan omvat.

Aan de hand van een nieuw albedo schema in RACMO2 wordt in hoofdstuk 4 de gevoeligheid van de oppervlaktemassabalans componenten voor parameters in het albedo schema getest. Het nieuwe albedo schema is afhankelijk van de korrelgrootte van de sneeuw, welke verandert onder invloed van droge (samenpakking) en natte (smelt en herbevrozing) verdichting. Voor het eerst wordt ook de ruimtelijke variabiliteit van het ijsalbedo meegenomen. Op basis van satellietwaarnemingen is er een achtergrond albedoveld geïmplementeerd. Bij vergelijking met albedo-observaties van weerstations op de ijskap geeft het nieuwe schema een flinke verbetering van het gemodelleerde albedo. Het nieuwe albedo, en dus ook de OMB, is met name gevoelig voor veranderingen in de herbevrozingsparameters. De reden hiervoor is de grote onzekerheid in deze parameters, omdat er geen directe metingen van herbevrozing bestaan. Indirecte metingen, zoals het aantal dagen dat er smelt plaatsvindt aan het oppervlak van de ijskap, zijn gebruikt om deze onzekerheid te verkleinen.

Met de optimale afstelling van RACMO2, gebaseerd op de resultaten uit hoofdstuk 4, is een continue simulatie gedaan van 1960-2012, waarvan de resultaten in hoofdstuk 5 beschreven staan. Van 1960-1990 is de oppervlaktemassabalans van Groenland redelijk constant rond de 410 Gt per jaar. De grenslaag boven Groenland is gemiddeld over de zomermaanden van 2007-2012 ongeveer 2 °C warmer in vergelijking met 1960-1990. Het versterkte broeikaseffect, in combinatie met advectie van

warme, continentale lucht naar de ijskap ligt hieraan ten grondslag. Niet zozeer de opwarming van de grenslaag heeft gezorgd voor de sterke toename in smelt en runoff de afgelopen decennia, als wel het terugkoppelingseffect via het verlaagde albedo. Gemiddeld over de zomermaanden van 2007-2012 is er 11% meer kortgolvlige straling geabsorbeerd. Tot aan 2005 werd de toename in runoff grotendeels gecompenseerd door een positieve accumulatie anomalie. Sindsdien is de accumulatie echter weer afgenomen, leidend tot de record lage OMB in de afgelopen jaren. Tussen 1991 en 2011 heeft de Groenlandse ijskap in totaal  $1800 \pm 300$  Gt aan massa verloren door veranderingen in de OMB.

In hoofdstuk 6 worden de resultaten voor een toekomst scenario van het Groenlandse klimaat tot aan 2100 gepresenteerd. Hiervoor is RACMO2 aangedreven met uitvoer van een mondiaal klimaatmodel voor een gemiddeld opwarmingscenario. Ten opzichte van de afgelopen 20 jaar zal het volgens deze modelberekening boven Groenland in de zomermaanden de laatste 20 jaar van deze eeuw  $2,6$  °C warmer worden. Als gevolg hiervan vindt er over de gehele ijskap jaarlijks significante smelt plaats en de OMB laat een versnelde afname zien, waarbij deze rond 2070 negatief zal worden in dit scenario. Een belangrijke reden voor de versnelde afname van de OMB is de relatieve afname van herbevrozing van smeltwater in het firnpakket. Nu herbevroest 38% van het vloeibare water (smeltwater en regen), tegen het eind van deze eeuw is dat nog 29%. De voornaamste reden hiervoor is dat de hoeveelheid lucht in de firnlaag met meer dan 50% afneemt en deze laag dus sneller verzadigd is. In totaal zal het afsmelten van Groenland ongeveer 4 keer zo veel aan de zeespiegelstijging bijdragen als gemiddeld over de afgelopen 20 jaar.

Het laatste hoofdstuk beschrijft de resultaten van een studie naar vloeibaar water in de firnlaag. Tijdens de Arctic Circle Traverse expeditie, georganiseerd om de accumulatie in zuidoost Groenland te bepalen, werd er bij het boren van ijskernen vloeibaar water aangetroffen terwijl de temperatuur ver onder het vriespunt lag en het smeltseizoen nog niet begonnen was. Dit vloeibare water is dus ondanks de lage temperaturen in de winter ( $-30$  °C) niet bevroren. Aan de hand van radarmetingen, zowel aan de grond als vanuit de lucht, is in kaart gebracht dat het geen lokaal fenomeen is, maar met name in zuidoost Groenland uitgebreid aanwezig is. Ook in het sneeuwmodel van RACMO2 blijkt vloeibaar water op ongeveer dezelfde locaties gesimuleerd te worden. De gebieden waar vloeibaar water aanwezig is worden gekenmerkt door zowel sterke accumulatie als smelt. In de zomer raakt het firnpakket verzadigd met smeltwater, waarna in de herfst de verse sneeuwval deze laag van de koude atmosfeer isoleert.

De afgelopen jaren is het begrip van de interactie tussen de atmosfeer en de Groenlandse ijskap sterk verbeterd, desalniettemin blijven er nog vraagstukken lig-

---

gen. Zo is het onzeker of de veranderingen in atmosferische circulatie de afgelopen jaren boven Groenland het gevolg zijn van de opwarming van de aarde, of toe te schrijven zijn aan natuurlijke variabiliteit. Wat betreft oppervlaktemassabalansprocessen zit de grootste onzekerheid in herbevrozing, met name omdat hier geen directe observaties van bestaan. De komende tijd wordt hier meer onderzoek naar gedaan aan de hand van een hoge resolutie firnmodel, waarin ook horizontaal en verticaal watertransport meegenomen worden. Daarnaast worden er momenteel test-simulaties gedaan met een nieuwe, verbeterde versie van RACMO2. Ondanks de toegenomen rekenkracht van computers en de verbetering in kwaliteit van mondiale klimaatmodellen, blijft het gebruik van resultaten van regionale klimaatmodellen in veel studies onmisbaar.

1



# Arctic climate

---

## 1.1 Background

The Arctic is generally defined as the region north of the Arctic Circle ( $\sim 67^\circ\text{N}$ ), where the sun remains above the horizon during summer solstice. Climatologically, the Arctic is often defined as the region where average July temperature remains below  $10^\circ\text{C}$ , or north of the tree line, which nearly coincide on most land areas. The centre of the Arctic is formed by the Arctic Ocean, mostly surrounded by land, with the exception of the open connection to the Atlantic Ocean (Fram Strait, between Norway and Greenland) and the Pacific Ocean (Barentsz Strait, between Alaska and Russia, Fig. 1.1). The absence of solar radiation in winter and the long summer days result in a strong seasonal cycle in the Arctic Climate. However, the vicinity of warm ocean water and the low elevation keep the winters relatively mild compared to Antarctica, and lowest winter temperatures on the Northern Hemisphere are not reached near the North Pole.

The cryosphere forms a prominent feature in the Arctic climate system, with large expanses of permafrost, numerous ice caps and glaciers, the Greenland ice sheet (GrIS, section 1.2), snow covered land in winter and sea ice (section 1.1.1) in the Arctic Ocean. The high reflectivity of snow and ice is the major reason for the high climate sensitivity in the Arctic. Both measured over recent decades as well as reconstructed since the industrial revolution, warming in the Arctic has been almost twice as large as averaged over the northern hemisphere (*Bekryaev et al.*, 2010), a phenomenon known as polar amplification (*Screen and Simmonds*, 2010). The strong warming in the Arctic is reflected in reduced (summer) sea ice cover and higher Arctic Ocean temperatures (*Steele et al.*, 2008), enhanced melting of the GrIS and a northward migration of the permafrost and tree lines in North America and Siberia (*Soja et al.*, 2007).

Via atmosphere and ocean, the Arctic is connected to the climate of southern latitudes. Cold Arctic waters form an important component of the deep water formation in the North Atlantic and the forcing of the thermohaline circulation *Hatun* (2005),

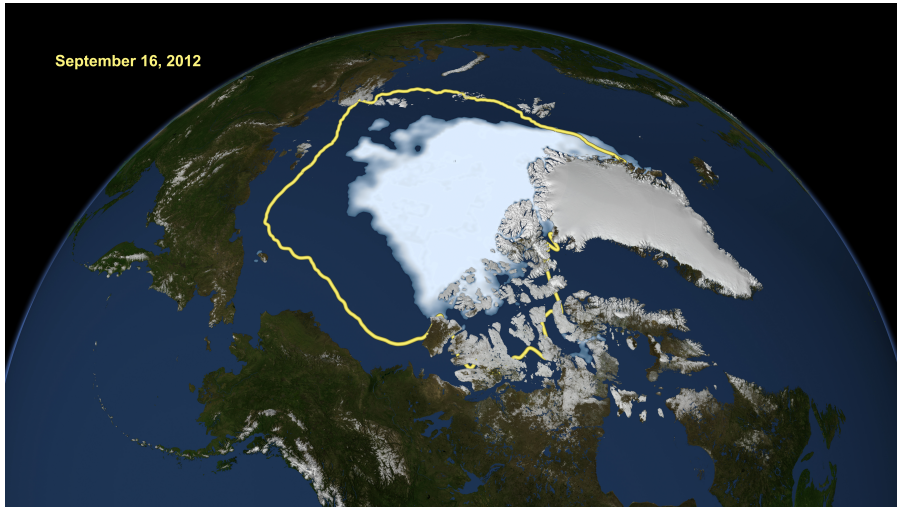


**Figure 1.1:** Satellite image of the Arctic region constructed by NASA from the special sensor microwave/imager (SSM/I), with minimum sea ice extent on September 13 2012. The yellow line indicates the 1979-2010 average minimum September sea ice extent.

which is likely to weaken upon increased freshwater input (*Dickson et al.*, 2002), resulting in a negative feedback (cooling) for the climate over the North Atlantic and surrounding land areas (*Rahmstorf and Ganopolski*, 1999). In the atmosphere, variability in the large scale circulation strongly influences Arctic climate. The Arctic Oscillation (AO), closely related to the North Atlantic Oscillation (NAO), explains a large part of the variability in sea level pressure in the Arctic (*Thompson and Wallace*, 1998). A positive AO-index indicates a stronger than normal pressure difference between the Arctic and southern latitudes; this pressure distribution is associated with stronger westerlies and greater cyclone activity over the Arctic ocean. Sea ice motion is also influenced by variability in the pressure distribution and associated near-surface winds (*Rigor et al.*, 2002).

### 1.1.1 Arctic sea ice

A key player in the Arctic climate system is sea ice in the Arctic Ocean and its surrounding seas. Arctic sea ice cover, especially its minimum extent, which is generally reached in September, has shown a rapid decline over the past twenty years. Records were set in 2002, 2005, 2007 and again in 2012 (*Comiso*, 2012; *Stroeve et al.*, 2007,



2012). Figure 1.1 compares average September sea ice extent for 1979-2010 with 2012, when extent was more than 30% lower compared to the 1979-2010 average. Not only the extent of Arctic sea ice is shrinking, so is its thickness and thus volume (*Kwok and Rothrock, 2009*). The fraction of first and second year sea ice in winter gradually decreases; sea ice of more than four years old is now only found north of Canada. The amount of multiyear sea ice is decreasing at a pace of more than 15% per decade in winter (*Comiso, 2012*).

Although the loss of sea ice has no significant impact on sea level rise, because it is afloat already, the increased area of open water introduces positive feedbacks; the most important is the ice-albedo feedback. Sea ice reflects more solar radiation back to the atmosphere than open water. If the sea ice is snow covered, this difference can be as much as 400%: more than 80% of the solar radiation is absorbed by open water, compared to less than 20% for sea ice covered by a fresh snow layer. This feedback has been identified as the most important cause of polar amplification, i.e. the enhanced warming in the Arctic (*Bekryaev et al., 2010; Flanner et al., 2011; Screen and Simmonds, 2010*).

A second feedback involves the reduction of the effect the sea ice has on heat and momentum exchange between atmosphere and ocean. The reduced and thinned sea ice cover results in a larger heat exchange from the ocean to the lower atmosphere, especially in fall, with higher near-surface air temperatures as a result (*Kurtz et al., 2011*). Near-surface winds also have a larger impact on thinner sea ice, resulting in increased drift speeds of sea ice over the last decade (*Kwok et al., 2013*). For instance in August 2012, a low pressure system over the Arctic ocean caused strong winds that led to the break up of large areas of sea ice (*Parkinson and Comiso, 2013*).

Besides the impact on the Earth's climate, the reduction of sea ice cover also presents an opportunity for exploration of the Arctic Ocean and economical benefits. Already since the 16th century, sailors have searched for a shipping lane north of Russia (e.g. the Dutch explorer Willem Barentsz), known as the Northeast Passage. In 2009, it was traversed successfully by two German cargo vessels. This route greatly shortens the distance over water between Europe and Asia. With improved technology, ever growing energy demands and melting of the sea ice, exploration of the natural resources in the Arctic has led to a heated debate in Arctic countries, putting claims on the rich grounds in that area.

## 1.2 The Greenland ice sheet

Greenland, the largest island on Earth, stretches ~2600 km from Cape Farewell (~60° N) to its northern extremity at ~83° N, and ~1000 km from east to west. Its surface of ~2.1 million km<sup>2</sup> is for 80% covered by ice. With a potential global average sea level rise of approximately 7 m, the Greenland ice sheet (GrIS), after Antarctica (~56 m potential sea level rise), represents the largest volume of land ice on Earth. The GrIS has a maximum elevation of ~3200 m with two domes in the south and centre (Fig. 1.2). Owing to its high elevation, the GrIS has a strong influence on atmospheric circulation (*Petersen et al.*, 2004). The vertical compression of the west-east flow over Greenland results in a local high pressure system and meridional distortion of this circulation (Chapter 2). Regional flow patterns, such as katabatic winds (*Heinemann*, 1999), barrier winds (*Petersen et al.*, 2009; *Van den Broeke and Gallée*, 1996) and tip jets (*Moore and Renfrew*, 2005) in the vicinity of Greenland also have a strong influence on the regional climate.

Although most of Greenland is covered by ice, with the associated low temperatures at high elevations, low lying coastal regions are characterized by a relatively mild summer climate. Over the snow-free tundra in summer, near-surface air temperatures can reach 10-20°C, but on average are 5-10 °C. Temperature gradually decreases with elevation over the ice sheet (Fig. 1.2a). Below ~1500 m, the ice sheet experiences melt during most of summer *Fettweis et al.* (2011), reflected by a 2 m temperature ( $T_{2m}$ ) close to the melting point. From Fig. 1.2a, the averaged extent of summer sea ice around Greenland can also be deduced, with summer  $T_{2m}$  close to the melting point, whereas open water is characterized by clearly positive values.

Fig 1.2b displays averaged 1960-2012 precipitation rates over Greenland (snow and rain). Up to 3 meter of water equivalent (m w.e.) of mostly solid precipitation is falling over the steep south-eastern ice sheet (*Box et al.*, 2013), under the influence of orographic lifting combined with frequent passages of low pressure systems in that region (*Tsukernik et al.*, 2007). A decreasing precipitation gradient from south to north is present over the ice sheet, with the lowest rates for northeast Greenland (<100 mm yr<sup>-1</sup>); this region is situated at the lee side for the (mostly) western flow over the northern part of Greenland.

The relatively mild climate, associated strong summer melt and high precipitation rates over Greenland are in sharp contrast with the Antarctic ice sheet, which, especially in East Antarctica, is very dry and cold. Global warming therefore represents a much larger threat to the GrIS, where increased summer temperatures will directly enhance melting, whereas for Antarctica temperatures will remain below freezing for most of the continent, with the exception of the Antarctic Peninsula and parts of West

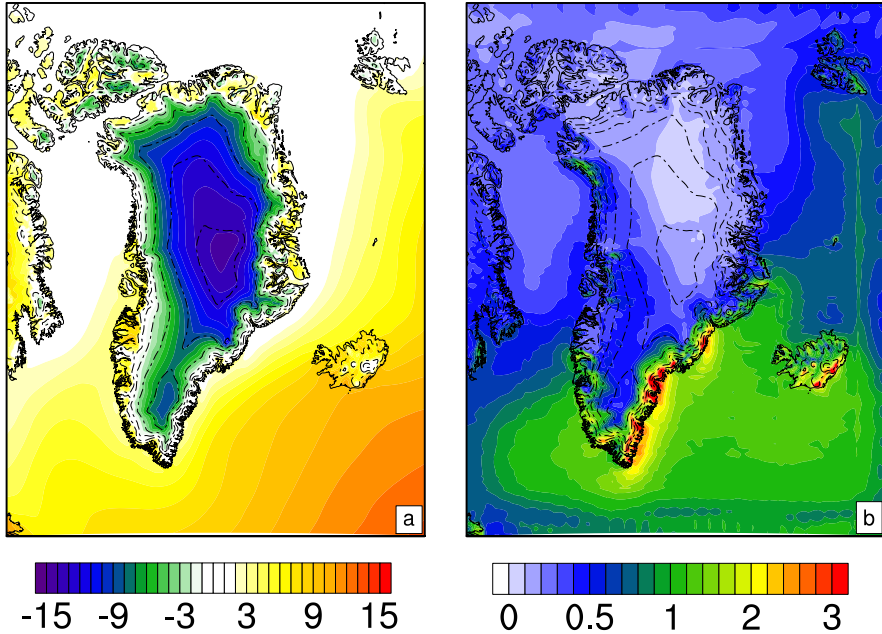


**Figure 1.2:** Averaged 1960-2012 summer (JJA)  $T_{2m}$  (a) and yearly precipitation [m w.e.] (b) from RACMO2. Height contours every 500 m.

Antarctica (Hanna *et al.*, 2013).

### 1.2.1 Mass Balance

Neglecting mass fluxes at its base, the mass balance of an ice sheet is determined by net accumulation/ablation at its surface, called the surface mass balance (SMB), and mass loss by solid ice discharge across the grounding line, the location where the ice starts to float. An ice sheet is in balance if SMB equals discharge. To estimate the mass balance of an ice sheet, three independent methods are currently being applied. The first method is based on a volumetric approach in which height changes of an ice sheet are determined using repeat radar (Davis, 2005) or laser altimetry measurements (Zwally *et al.*, 2011). When elevation changes are converted to mass changes, the delicate densification processes in the firn layer covering the GrIS should be taken into account (Zwally and Jun, 2002). The second approach makes use of changes in the Earth's gravity field as a result of the displacement of mass from the ice sheets

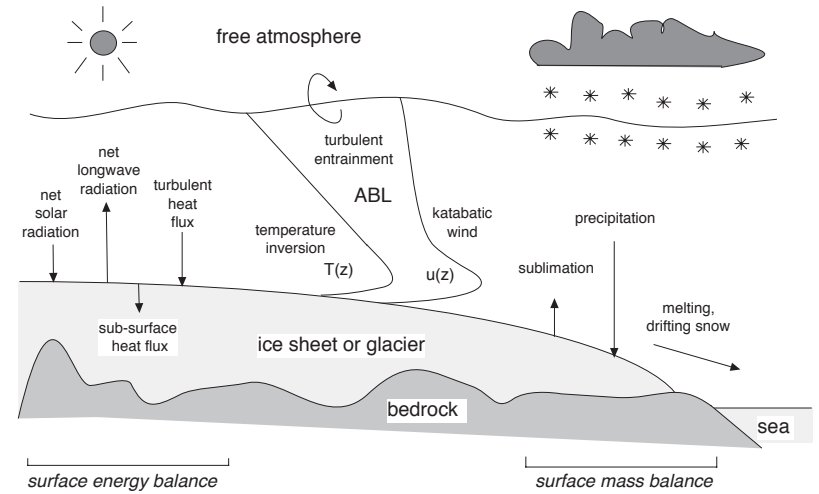


**Figure 1.3:** Surface energy and mass balance processes in the atmospheric boundary layer over an ice sheet (Van den Broeke, 1996).

to the oceans. For this, the twin satellites of the Gravity Recovery and Climate Experiment (GRACE) are used (Wahr *et al.*, 2004; Wouters *et al.*, 2008). Finally, in the mass budget method, SMB and solid ice discharge are determined separately, and differenced. For fast flowing parts: satellite radar feature tracking is used to determine ice velocities (Joughin and Winebrenner, 1995; Rignot, 2006) and integrated over the ice thickness to calculate ice discharge at the grounding line (Moon *et al.*, 2012). The SMB of an ice sheet is commonly determined by interpolation of sparse *in situ* observations or the application of regional or global climate models, which explicitly calculate the mass gain by precipitation and mass loss through sublimation and meltwater runoff by solving the surface energy and mass balance equations (e.g. Ettema *et al.* (2009); Fettweis *et al.* (2012a); Van de Berg *et al.* (2006)).

The SMB is the difference between total solid and liquid precipitation (PR), meltwater runoff (RU) and sublimation (SU):

$$SMB = PR - RU - SU. \quad (1.1)$$

Meltwater runoff is the flux of liquid water that is lost from the ice sheet to the ocean:

$$RU = ME + RN - RF, \quad (1.2)$$

with ME surface meltwater production, RN rain flux and RF the amount of liquid water that is refrozen and retained within the ice sheet. The amount of produced meltwater is determined by the amount of energy available for melt (M), which in turn is determined by the surface energy balance:

$$M = R_{net} + LHF + SHF + G_s, \quad (1.3)$$

with  $R_{net}$  the net radiation, the sum of incoming and outgoing short- and long wave radiation,  $LHF$  the latent heat flux,  $SHF$  the sensible heat flux and  $G_s$  the subsurface heat flux. As soon as the surface temperature reaches the melting point, i.e. 273.15 K, the surplus energy is used for surface melting. An important parameter in the surface energy balance and thus ice sheet mass balance is surface albedo, which determines the amount of absorbed solar radiation. For fresh snow, the albedo ranges between 0.8 and 0.9, indicating that only 10-20% of the incoming solar radiation is absorbed. Dirty bare ice can have an albedo as low as 0.2, which absorbs up to eight times more radiation than fresh snow; this stresses the strong positive albedo-melt feedback, when snow is replaced by bare ice at the surface. Figure 1.3 summarizes the processes in the lower atmospheric boundary layer that are important for the surface energy and mass balance of an ice sheet.

## 1.2.2 Contemporary GrIS mass balance

During 1960-1990, the GrIS is assumed to have been in approximate balance (*Van den Broeke et al.*, 2009), with discharge and SMB both in the order of 450 Gt yr<sup>-1</sup> (*Ettema et al.*, 2009; *Rignot et al.*, 2008a). SMB is made up of total precipitation in the order of 750 Gt yr<sup>-1</sup> (*Box et al.*, 2013), meltwater runoff ~250 Gt yr<sup>-1</sup> and sublimation ~50 Gt yr<sup>-1</sup> (*Ettema et al.*, 2009). The latter component can be divided between surface sublimation (~40%) and drifting snow sublimation (~60%) (*Lenaerts et al.*, 2012a).

Since the early 90's, the GrIS has been in a state of imbalance, with a strong acceleration of mass loss since 2005 (*Rignot et al.*, 2011; *Shepherd et al.*, 2012). Contributing to this accelerated mass loss are increased meltwater production at the surface (*Fettweis et al.*, 2011; *Tedesco et al.*, 2011), acceleration of outlet glaciers leading to increased discharge rates (*Moon et al.*, 2012; *Nick et al.*, 2009), and relatively small accumulation rates in recent years with the exception of 2012 (*Van Angelen et al.*, 2013). The increased melt rates at the surface are also reflected in

a decrease of surface albedo in summer, further enhancing surface melt (*Box et al., 2012a*).

The combination of various methods to estimate ice sheet mass balance and longer records of satellite measurements have greatly reduced the uncertainty in mass loss estimates for the GrIS. Between 1992 and 2011, the GrIS has lost  $2700 \pm 930$  Gt of mass, equivalent to  $7.5 \pm 2.6$  mm of sea level rise (*Shepherd et al., 2012*). The average contribution from the GrIS to global sea level rise of  $\sim 0.7$  mm yr<sup>-1</sup> over the last six years is as large as that from all glaciers and ice caps outside Greenland and Antarctica (*Chen et al., 2013; Hanna et al., 2013*).

### 1.3 Regional Atmospheric Climate Models

The application of regional atmospheric climate models has greatly improved our understanding of the climate of Greenland (*Ettema et al., 2009; Fettweis et al., 2012b*) and Antarctica (*Van de Berg et al., 2008; Van den Broeke et al., 2002*). Although these models are called climate models, in reality they simulate weather. Averaging these weather data over longer timescales gives the climate of the studied region, and by assessing different epochs the impact of climate change is quantified.

One of the big advantages of regional modeling is the relatively high horizontal resolution ( $\sim 10$  km) at which the simulations are generally performed. This way, spatially strongly varying climate variables, such as the steep SMB gradient along the margins of the GrIS are realistically simulated. Furthermore, regional climate models can be adjusted to better represent conditions for a specific region. For example, to simulate climate over an ice sheet, the atmospheric part of the model can be coupled to a (high-resolution) snow model, such that the interaction between the atmosphere and the snow/ice surface is better resolved. Another advantage of models compared to observational data is the continuous (long) time series it creates on a regular grid. This makes the model output very useful to assess climate variability but also as forcing in other, for example ice dynamical, studies.

An important and difficult part of climate modeling is the evaluation of the output. The increasing amount of observational data from (automatic) weather stations helps to improve the model settings and in understanding the results. Also remote sensing by ground and airborne radar and satellites has greatly improved the evaluation of climate model output for Greenland. The combination of different remote sensing techniques in recent years has resulted in a complete coverage and almost continuous monitoring of the state of the GrIS. However, for a robust physical understanding of what is measured climate models remain essential. Regional climate models also

have an important role in projections of future climate change and mass loss.

## 1.4 This thesis

In this thesis, we assess various aspects of the present day and future climate and surface mass balance of the GrIS and its surrounding areas. For this, we use the regional atmospheric climate model RACMO2, supported by automatic weather station (AWS) observations and satellite retrievals. The core of the model is based on the ECMWF weather forecast model. Relevant details of the RACMO2 model are described in the different chapters. In Chapters 2 and 3 we use output of RACMO2 version as described in *Ettema et al. (2010a)*. The results in Chapters 4-6 are based on the same model, but with the inclusion of a drifting snow scheme (*Lenaerts et al., 2012a*) and an upgraded, grain size dependent, albedo scheme (*Kuipers Munneke et al., 2011; Van Angelen et al., 2012*).

In Chapter 2 output of RACMO2 is used to explicitly solve the momentum budget of the atmospheric boundary layer over the GrIS. The results explain in detail the near-surface wind patterns and the interaction between the near-surface forcing of the characteristic katabatic winds over the ice sheet and the large scale circulation, as well as the impact of the snow free tundra in summer on local winds.

Chapter 3 is a continuation of Chapter two, with focus on the persistent northerly flow along the east coast of Greenland. This flow, called 'The Greenland Sea Jet', is of special interest, because it is the main forcing mechanism for sea ice transport through Fram Strait, the most important gateway for sea ice out of the Arctic Ocean (*Kwok et al., 2004*).

Chapters 4-6 deal with the SMB of the GrIS and related processes. In Chapter 4 a new grain size dependent albedo scheme for RACMO2 is used, to study the sensitivity of SMB components to parameters in this scheme. In surface energy and mass balance studies, a correct simulation of surface albedo is crucial, because small changes in snow and ice albedo have a large impact on the amount of absorbed radiation, and there is a strong positive feedback between albedo, melt, refreezing and retention.

In Chapter 5 the contemporary (1960-2012) SMB of the GrIS and its individual components is analyzed. The atmospheric circulation and changes therein are assessed to explain the rapid acceleration of surface mass loss from the GrIS since 2005. Retrievals from the Gravity Recovery And Climate Experiment (GRACE) are used to evaluate the seasonal cycle of mass of the GrIS as calculated by RACMO2.

Chapter 6 addresses the question: What can we expect if Greenland will be sub-

ject to a certain warming scenario? To that end, RACMO2 is forced with output of a Global Climate Model (GCM) to study a realistic scenario for the SMB of the GrIS in the 21st century. Focus of this chapter is on the firn layer, the layer of compressed snow that covers the ice sheet. The firn layer shields the ice sheet from direct contact with the atmosphere, but upon warming this layer will be removed by melting, after being saturated by meltwater.

The final Chapter (7) gives a summary of the main findings in this thesis, presents ongoing work (a case study concerning liquid water in the Greenland firn) and gives recommendations for future work.





2



# Momentum budget of the atmospheric boundary layer over the Greenland ice sheet and its surrounding seas

---

*The atmospheric circulation patterns over the Greenland ice sheet and its surrounding seas are studied by explicitly calculating the momentum budget components, using data of a high-resolution regional atmospheric climate model. In winter (DJF), the katabatic pressure gradient force (PGF) dominates the momentum budget of the atmospheric boundary layer (ABL) over the ice sheet. Over the western slopes of the ice sheet, the large scale PGF acts in the same direction as the katabatic PGF, resulting in a strong southerly jet of up to  $12 \text{ m s}^{-1}$ . In winter, the accumulation of cold air over the sea ice along the northeast coast leads to a thermally induced northerly flow. This circulation facilitates southward sea ice transport in this area, and is enhanced by the large scale circulation. Along the west coast, a similar west-east temperature gradient also forces a northerly flow. In the summer months, sea ice is absent and thermal wind forcing is largely reduced over the ocean. Summer insolation also reduces katabatic forcing, the large scale forcing dominates the ABL momentum budget over the ice sheet. Heating of the ABL over the snow free tundra induces thermal contrasts with the ice sheet and ocean, forcing barrier winds in the coastal regions. Throughout the year, strong surface layer winds along the southeast coast of Greenland are forced by the large scale PGF.*

## 2.1 Introduction

Regional atmospheric circulations are very important for the climate and mass balance of ice sheets and fringing ice shelves. Local winds determine the occurrence, size and shape of polynya's and the rate of sea ice and deep water formation. Through katabatic and thermal wind forcing, wind and temperature are strongly coupled in the mostly stably stratified surface layer (SL) over the ice sheets, modifying the free atmospheric signal when it is transferred to the surface of the ice sheet. It is therefore important to assess in detail the momentum and heat budgets of the near-surface atmosphere over the ice sheets (*Van de Berg et al.*, 2008).

The high shortwave reflectivity (albedo) of the ice/snow surface in combination with the high longwave emissivity create a surface based temperature inversion, which is most pronounced in wintertime. The resultant negatively buoyant air drives the katabatic wind, which is so characteristic for sloping, ice covered surfaces. *Ball* (1956) and *Mahrt* (1982) provided a theoretical framework for the momentum budget of katabatic (gravity) flows. Since then, several field campaigns (*Heinemann*, 1999; *Steffen and Box*, 2001; *Van den Broeke et al.*, 1994) and modeling studies (*Bromwich et al.*, 1996; *Ettema et al.*, 2010b; *Heinemann and Klein*, 2002) have been performed to study the katabatic wind regime over Greenland.

With a height of up to 3200 m and located just north of the northern hemisphere Atlantic storm track, the Greenland ice sheet (GrIS) has a strong influence on the atmospheric circulation in the North Atlantic region (*Petersen et al.*, 2004; *Scorer*, 1988). Owing to its size, the GrIS creates its own regional climate; beside katabatic winds, several other interesting atmospheric circulation patterns are present in the vicinity of Greenland. The atmospheric circulations along the southeastern and southern coasts have been extensively studied during the Greenland Flow Distortion experiment (*Petersen et al.*, 2009; *Renfrew et al.*, 2008, 2009). High windspeed events, known as tip jets, occur south of Cape Farewell (*Doyle and Shapiro*, 1999; *Moore and Renfrew*, 2005; *Vage et al.*, 2009). The topography along the east coast induces convergence of the katabatic winds leading to the strong Piteraq winds (*Klein and Heinemann*, 2002). *Van den Broeke and Gallée* (1996) observed and simulated barrier winds over the western margins of the GrIS.

In this study we calculate, for the first time explicitly in space and time, the components of the momentum budget of the lower atmosphere to provide a theoretical framework for the atmospheric circulation over and around the GrIS. For this we use a well evaluated 51-year run of the high resolution regional climate model RACMO2.1/GR. The next section briefly describes the model, the various components in the momentum budget and the data analysis applied to calculate these com-

ponents. Section 2.3 presents results of the wintertime momentum budget and associated temperature and wind fields, with special focus on a cross-section through Northern Greenland, while section 2.4 presents results for the summer months. Conclusions are given in section 2.5.

## 2.2 Methods

### 2.2.1 Model and evaluation

We use data of the regional atmospheric climate model RACMO2.1/GR for the period 1958-2008 (Van Meijgaard *et al.*, 2008). RACMO2 is hosted by the KNMI (Royal Netherlands Meteorological Institute) and based on the ECMWF physics package cycle 23r4 (White, 2004), which is implemented in the numerical weather prediction model HIRLAM 5.0.6 (Unden *et al.*, 2002). Several adjustments have been made to make the model suitable for polar climates (Ettema *et al.*, 2010a). RACMO2.1/GR is a hydrostatic model with 40 sigma levels in the vertical and a horizontal grid spacing of 11 km. Model output from this and preceding versions has been successfully used for mass balance and atmospheric boundary layer studies in Antarctica (Reijmer *et al.*, 2004; Van de Berg *et al.*, 2006; Van den Broeke *et al.*, 2002), and Greenland (Ettema *et al.*, 2009; Van den Broeke *et al.*, 2009). The model is forced at the lateral boundaries by ECMWF reanalysis (ERA-40) data every 6 hours. From August 2002 onwards, operational data of the ECMWF are used. The area where the model evolves freely covers Greenland and the surrounding oceans, including Iceland and Svalbard (Figure 2.1). The quality of RACMO2.1/GR output (temperature, wind, moisture and surface energy balance) has been extensively evaluated in Ettema *et al.* (2010a) and it is shown that the model is capable of realistically resembling the (katabatic) wind regime in the Greenland area.

It is obvious that a model with a grid of 11 km is not capable of solving small scale processes like glacier winds, small scale circulations in the Fjord areas and the occurrence of multiple stratified layers under very stable conditions. Such processes occur on small spatial scales, but also on small time scales (hours to days). In this study we focus on the climatology of the atmospheric circulation and the previously discussed small scale phenomena are of weak influence on the 45 year averages of the momentum budget components analysed in this study.

2. Momentum budget of the atmospheric boundary layer over the Greenland ice sheet and its surrounding seas

---

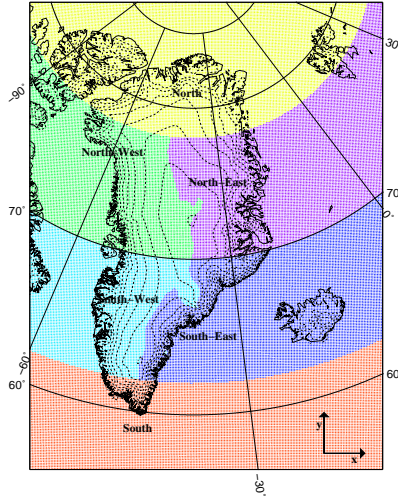


**Figure 2.1:** Definition of different areas for analysis, north (N), northeast (NE), southeast (SE), south (S), southwest (SW) and northwest (NW). Also shown are x, y coordinates used in this work.

### 2.2.2 Momentum budget

An important component in the momentum budget of the Greenland atmospheric boundary layer (ABL) is the katabatic pressure gradient force (PGF). We use a standard x-y-coordinate system and concentrate on the momentum budget in the x-direction, because the Greenland slopes are mostly oriented in this direction (Figure 2.1). The approximate momentum balance in the x-direction, with surface slope  $\alpha$ ,  $U$  and  $V$  the wind velocity components in the x- and y-direction respectively, and  $\theta_0$  the background potential temperature, is as follows:

$$\frac{\partial U}{\partial t} = \overbrace{-U \frac{\partial U}{\partial x} - V \frac{\partial U}{\partial y}}^{\text{HADV}} - W \frac{\partial U}{\partial z} + \frac{g}{\theta_0} \frac{\partial \hat{\theta}}{\partial x} + fV - fV_{LSC} - \frac{\partial \overline{uw}}{\partial z} + \frac{g}{\theta_0} \Delta_\theta \sin \alpha, \quad (2.1)$$

with  $\Delta_\theta$  the temperature perturbation:

$$\Delta_\theta(z) = \theta(z) - \theta_0(z), \quad (2.2)$$

and  $\hat{\theta}$  the vertically integrated temperature perturbation of the temperature deficit layer (TDL); in which  $|\Delta\theta| > 0$ :

$$\hat{\theta}(z) = \int_z^{h_f} \Delta_\theta(z) dz, \quad (2.3)$$

where  $h_f$  is chosen well above the TDL top. The advantage of this method is that the interface between the stable boundary layer and the free troposphere does not have to be precisely defined.

The components of the momentum balance can be divided into active and passive forces. The latter are only present if atmospheric motion exists; these are the horizontal (HADV) and vertical advection (VADV), the Coriolis force (COR) and friction (FDIV). The active forces are the thermal wind (THW), katabatic (KAT) and large scale (LSC) pressure gradient forces. KAT represents the downslope PGF resulting from a negative temperature perturbation over sloping terrain. THW is driven by horizontal variations in  $\hat{\theta}$ . It must be noted that these definitions for KAT and THW can lead to strong opposing forces over steep slopes if the top of the TDL is horizontal (*Van den Broeke and van Lipzig, 2003*). This is the situation along the east coast of Greenland, where the rough topography is engulfed in cold air; over a topographic disturbance  $\hat{\theta}$  increases rapidly in the downslope direction, leading to an upslope THW forcing; on the other hand  $\Delta_\theta$  generates a strong downslope KAT forcing. If the TDL top is horizontal these two effects exactly cancel.

By calculating the different forcing components in the momentum budget explicitly, a decoupling between the free atmosphere and the ABL may also be made. THW and KAT drive flows in the ABL, whereas LSC describes flows forced by the large scale atmospheric circulation.

### 2.2.3 Data analysis

In this study, a 45 year model climatology (1963-2007) of the ABL momentum budget for winter (DJF) and summer (JJA) is presented. To analyze the differences in wind patterns and climate over and around the GrIS, the model domain is subdivided into six regions (Figure 2.1). The boundary between east and west follows the ridge of the ice sheet. The distance to the coast is also used as parameter: bins of 25 km distance intervals are generally used, but in the coastal regions where the topography is steep and gradients in climate variables large, 10 km distance bins are used.

To determine the large-scale wind components, it is assumed that  $U_{LSC}$  and  $V_{LSC}$  are in thermal wind balance with the background potential temperature  $\theta_0$  (Van den Broeke *et al.*, 2002):

$$\frac{\partial U_{LSC}}{\partial \ln p} = + \frac{R_d}{f} \left( \frac{p}{p_0} \right)^{R_d/c_p} \frac{\partial \theta_0}{\partial y}, \quad (2.4)$$

$$\frac{\partial V_{LSC}}{\partial \ln p} = - \frac{R_d}{f} \left( \frac{p}{p_0} \right)^{R_d/c_p} \frac{\partial \theta_0}{\partial x}. \quad (2.5)$$

$\theta_0$  is found by linearly extrapolating the free tropospheric potential temperature to the surface with respect to pressure. For this procedure, we use 5 vertical model layers, located in the free troposphere. Furthermore a constant lapse rate ( $\gamma_\theta$ ) for the potential temperature in the free troposphere is assumed. This assumption is realistic since a maximum root-mean-square-difference of 0.2 K between the five interpolated and real potential temperature values is found for a single grid point. We get:

$$\theta_0(p) = \theta_0(p_0) + \gamma_\theta p. \quad (2.6)$$

The final results are not sensitive to the interpolation method used. Interpolation with respect to height instead of pressure is also tested, leading to qualitatively the same results. The number of model levels used for interpolation was also tested and likewise did not greatly affect the results.

Figure 2.2a shows vertical profiles of the (background) potential temperature averaged over NE Greenland for the 200-225 km inland distance bin (red area in Figure 2.5). This result serves as example here and will be discussed more extensively in section 2.3.3. At the surface, the magnitude of  $\Delta_\theta$  reaches a maximum and is as large as 16 K. Figure 2.2b displays wind profiles and the associated large scale winds, Figure 2.2c the vertical profiles of the different components in the momentum budget. Due to the strong negative surface temperature perturbation, the katabatic forcing (KAT) dominates in the lowest 500 m of the atmosphere, resulting in a windspeed maximum 100-200 m above the surface. In this example the katabatic PGF dominates the momentum budget in the TDL, and is mainly balanced by surface friction (FDIV, which is parameterized by the numerical model). The large scale pressure gradient force (LSC) becomes small near the surface, because the large scale wind is mainly in the x-direction ( $U$ ) in this area. THW is a small opposing force. The FDIV profile is according to what we expect: highest values close to the surface and a changing sign at the height of the windspeed maximum. The momentum budget is closed by the residual component (RES), which represents horizontal and vertical advection of



momentum and model diffusion of momentum. Advection is generally small on the spatial and time scales used in this study. Direct calculation of the horizontal and vertical advection components from model output (not shown) confirms these small values. Model diffusion of momentum is generally also small, except for the steep coastal regions, where strong gradients result in more model diffusion (see section 2.3.3).

## 2.3 Results: winter

### 2.3.1 Pressure, wind and temperature

The 500 hPa height contours show a southwesterly large scale flow over the GrIS in wintertime (Figure 2.3a). A pressure ridge is found over the ice sheet at 500 hPa as a result of the vertical compression of the column of air moving over the elevated ice sheet interior, resulting in more southerly flow over the western part of the ice sheet, and more westerly flow over the eastern part. The surface pressure distribution over the ocean is dominated by the Icelandic Low, and results in northerly and easterly flow near the surface. The change from southwesterly flow at 500 hPa to northwesterly flow near the surface underlines the strong baroclinicity in this region. Also visible in the surface pressure distribution is the effect of cold air pooling, increasing the surface pressure over eastern Canada and along the north and east coasts of Greenland. Over the ice sheet, near-surface winds are highly constant in direction, and strongest over the western and northeastern ice sheet (Figure 2.3b). Along the east and west coasts of Greenland, persistent regional northerly flows are visible. Although high wind speeds, associated with the so called 'tip jet', often occur south of Cape Farewell, they do not show up in the average vector mean wind field, because the directional constancy of the tip jet is low (*Moore, 2003*).

Over the GrIS, radiative cooling is strongest in winter, resulting in a large temperature deficit (Figure 2.3c). The average surface magnitude of  $\Delta_\theta$  over the GrIS increases from 8 K in the south to values of up to 20 K in the NE. This local maximum is due to low cloud-cover in this region, resulting in highly negative values of  $LW_{net}$  (*Ettema et al., 2010b*). A strong temperature deficit of typically 6-12 K is also found over the sea ice covered ocean, where the atmosphere is isolated from the ocean and the surface is flat, so cold air can accumulate. Tundra areas also show large temperature deficits, for example the west coast between 65° N and 68° N and the east coast just north of 70° N. In these flat areas, no sustained katabatic wind can develop, and strong surface based inversions develop over the snow-covered tundra.

## 2. Momentum budget of the atmospheric boundary layer over the Greenland ice sheet and its surrounding seas

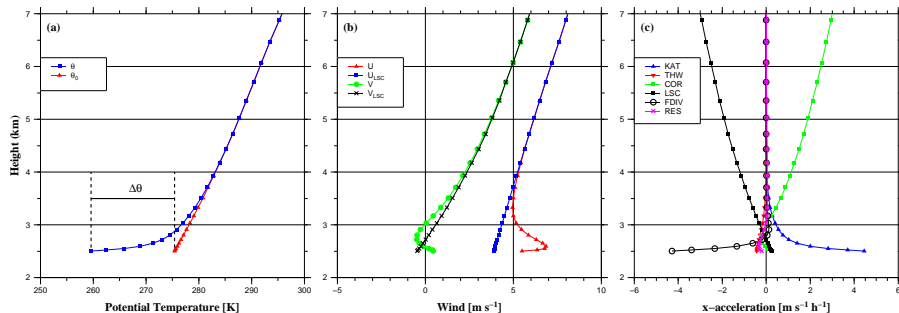
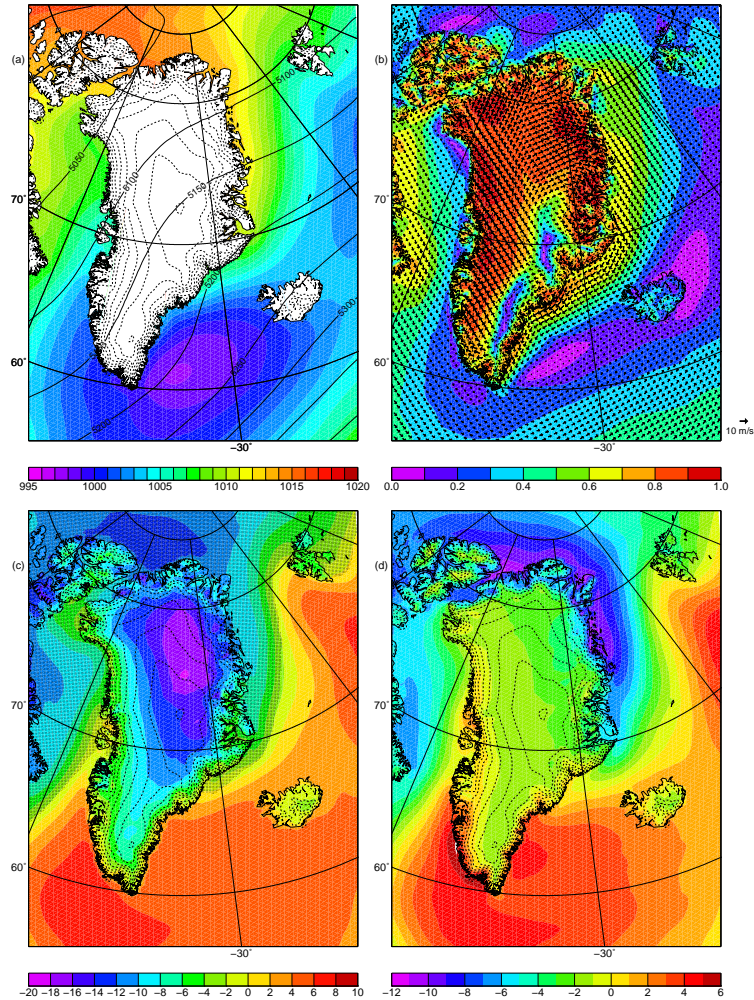


**Figure 2.2:** Average 1962-2007 (DJF) vertical profiles for the 200-225 km inland bin in the NE (red area in Figure 2.5); a) potential temperature ( $\theta$ ) and background potential temperature ( $\theta_0$ ), b) (large scale) wind components and c) the momentum budget components. Local gridpoint surface elevation is 2.5 km.

Figure 2.3d shows the average vertically integrated temperature perturbation ( $\hat{\theta}$ , units  $1000 \text{ K m}$ ) in winter. Surprisingly, small  $|\hat{\theta}|$ -values are found over the ice sheet, including areas where  $|\Delta\theta|$  at the surface is large. The reason is that the katabatic winds transport air radially away from the ice sheet interior, inducing mass divergence and subsidence. This keeps the TDL shallow and limits  $|\hat{\theta}|$  (Van den Broeke *et al.*, 2002). Highest magnitudes of  $|\hat{\theta}|$  are found over the sea ice covered ocean along the N and NE coasts. Cold air from the ice sheet accumulates over the flat surface of the sea ice, resulting in a deep TDL and hence large  $|\hat{\theta}|$ . A gradual decrease in  $|\hat{\theta}|$  is found in the offshore direction along the NE coast towards the sea ice free ocean. Over the GrIS, the highest magnitudes of  $|\hat{\theta}|$  are found in the NE as a result of strong temperature deficits in combination with a concave surface, limiting subsidence. Furthermore, an increase in  $|\hat{\theta}|$  is present in the downslope direction over the entire ice sheet, associated with a deepening of the TDL towards the ice sheet margins.

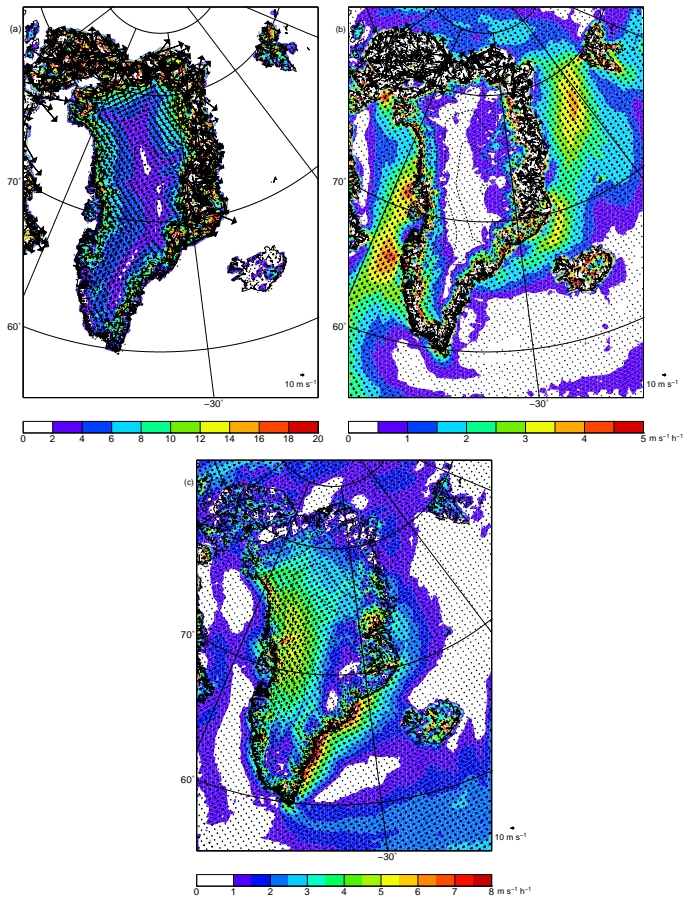
### 2.3.2 Momentum budget

Figure 2.4a shows the magnitude and the associated geostrophic wind field of the wintertime katabatic forcing (KAT) at the first model level ( $\sim 7 \text{ m}$  above the surface). Small values prevail over the relatively flat interior, rapidly increasing towards the coast. The strongest katabatic forcing is found in the NE, where values locally exceed  $20 \text{ m s}^{-1} \text{ h}^{-1}$ . This is the location with the largest temperature deficits in combination with steep slopes, in agreement with Steffen and Box (2001), who reported the strongest near-surface winds to occur in the NE.



**Figure 2.3:** Averaged wintertime (DJF) (a): sea-level pressure [hPa] (colors), 500 hPa height [m] (contours). (b): Wintertime 10 m winds [ $\text{m s}^{-1}$ ] and directional constancy, arrows every 9 gridpoints. (c): Surface temperature perturbation [K]; dotted area represents ocean with more than 50% sea ice concentration. (d): Vertically integrated potential temperature perturbation [ $10^3 \text{ K m}$ ]. Dashed contours are 400 m surface elevation intervals.

## 2. Momentum budget of the atmospheric boundary layer over the Greenland ice sheet and its surrounding seas



**Figure 2.4:** Spatial distribution of winter averaged magnitude of KAT (a), THW (b), LSC (c) for the lowest model layer ( $\sim 7$  m). Arrows indicate the associated geostrophic winds. Note the different scales.

The strength and associated geostrophic wind field of the thermal forcing (THW) is displayed in Figure 2.4b. Gradients in  $\hat{\theta}$  drive THW, therefore THW peaks in the orographically rough coastal regions, where, as explained earlier, KAT and THW become large but opposite in sign, and thus cancel. Interesting to note is that, due to the well-defined gradients in  $|\hat{\theta}|$  over the northern Atlantic Ocean, THW forces very persistent southward flows along the east as well as along the west coast of

Greenland. On the east coast, the accumulation of cold air above the sea ice covered ocean (for sea ice cover, see Figure 2.3c) results in a negative  $|\hat{\theta}|$  gradient, directed away from the coast. The associated THW forces a persistent southward geostrophic flow that facilitates the export of Arctic sea ice through Fram Strait, which is the main discharge of sea ice for the Arctic Ocean (Kwok *et al.*, 2004). Along the west coast of Greenland, the gradient in  $|\hat{\theta}|$  is also in the west-east direction (Figure 2.3d). We conclude that sea ice is more attached to eastern than western coastlines in the Northern Hemisphere, because a) cold continental air is available for sea ice growth; b) the resulting offshore directed pressure gradient force results in a northerly flow, resulting in an Ekman transport towards the coast. Due to this asymmetric distribution of sea ice, more cold air can accumulate along the western coasts, maintaining THW and the associated southward geostrophic flow.

The third active term in the momentum budget is the large scale pressure gradient force (LSC). Figure 2.4c shows the magnitude and the equivalent geostrophic wind field of LSC in the surface layer. Over the ice sheet, the largest values (over  $5 \text{ m s}^{-1} \text{ h}^{-1}$ ) are found over the western half, where the large scale wind follows the height contours. In this area, LSC acts in the same direction as KAT (Fig. 2.4a), resulting in a strong and persistent southerly jet. Over the ocean along the southeast coast, LSC dominates the momentum budget, with values up to  $8 \text{ m s}^{-1} \text{ h}^{-1}$ . It thus appears that the associated persistent along-shore winds are not barrier winds, since THW is small. Rather, these winds are predominantly forced by the large scale pressure gradient, partly a result of the strong baroclinicity in this area and the vicinity of the Icelandic Low.

### 2.3.3 Northern Transect

In this section we discuss horizontal and vertical profiles of the momentum budget and associated vertical wind and temperature distributions for a transect in North Greenland. The location of the cross section is shown in Figure 2.5. Potential temperature and wind speed cross sections are displayed in Figure 2.6a. Three well-defined boundary-layer jets characterize the near-surface atmospheric circulation; two jets over both flanks of the GrIS and one over the ocean along the east coast. Average vertical profiles for the 150-175 km inland bin of temperature, (large scale) winds and momentum budget components, in the NW (green area in Figure 2.5), are shown in Figure 2.7. In the free troposphere, the momentum budget reflects a simple geostrophic balance between COR and LSC (Figure 2.7c) with winds from the southwest. At a height of approximately 750 m above the surface,  $\theta$ ,  $U$  and  $V$  start to deviate from their background values (Figure 2.7a, b). Below this level the katabatic

## 2. Momentum budget of the atmospheric boundary layer over the Greenland ice sheet and its surrounding seas

---

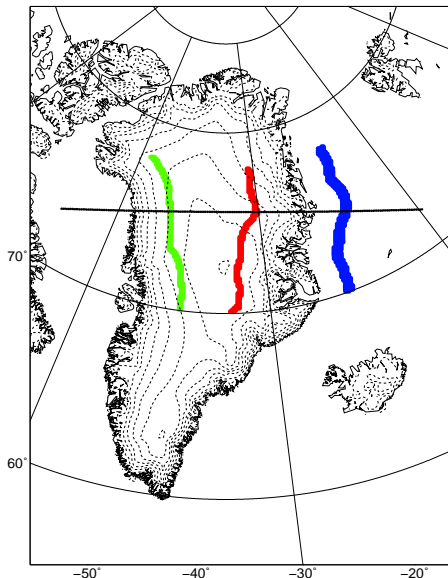


**Figure 2.5:** Location of the transect through Northern Greenland, and the three areas for which winter average vertical profiles are shown.

forcing becomes significant. At the surface, the temperature deficit ( $|\Delta\theta|$ ) is  $\sim 10$  K, leading to a katabatic forcing of  $-5 \text{ m s}^{-1} \text{ h}^{-1}$ . This makes KAT the dominant forcing in the surface layer, but it is interesting to note that the large scale forcing (LSC) is of similar magnitude and acts in the same direction. This results in a strong and persistent southerly low level jet with a wind maximum in excess of  $10 \text{ m s}^{-1}$ . This jet is only recently identified and named the 'Greenland Plateau Jet' (Moore, personal communication). Here we demonstrate that the jet is a result of a combination of equally important KAT and LSC forcing, comparable to strong winds found in the escarpment region of East Antarctica (Van den Broeke and van Lipzig, 2003). The difference between the large scale and actual wind at the height of the wind speed maximum is approximately  $3 \text{ m s}^{-1}$ .

Figure 2.2 showed vertical profiles for the 200-225 km inland bin in the NE sector (red area in Figure 2.5). At the surface,  $|\Delta\theta|$  becomes as large as 15 K, and the TDL is more than 1 km deep. Upper air winds are again from the southwest, however close to the surface LSC in the x-direction is small in this area, because the large scale flow is mainly oriented in the zonal direction. As a result the katabatic forcing dominates the momentum budget in the x-direction and the wind profile is typically katabatic,

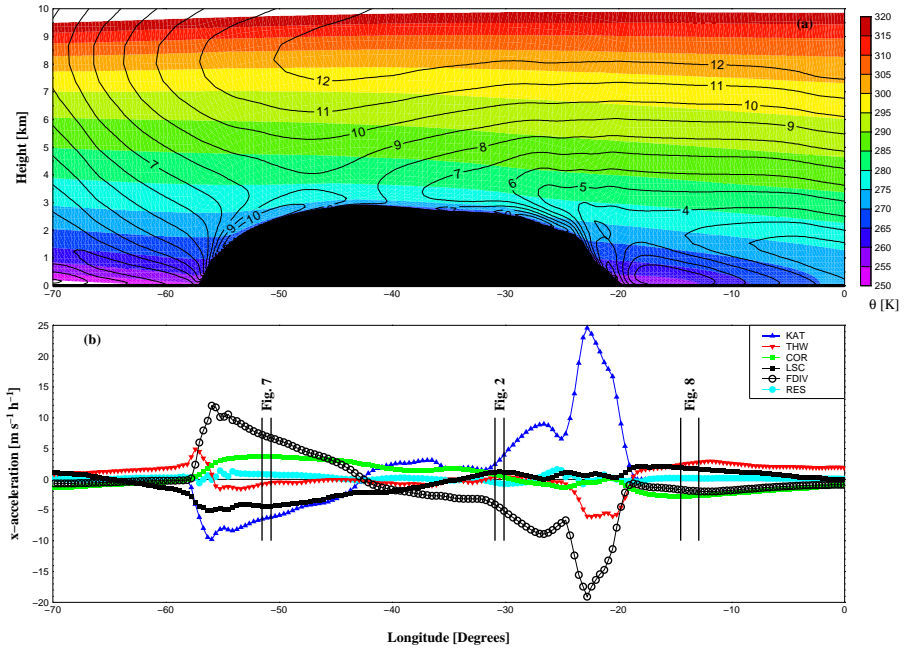
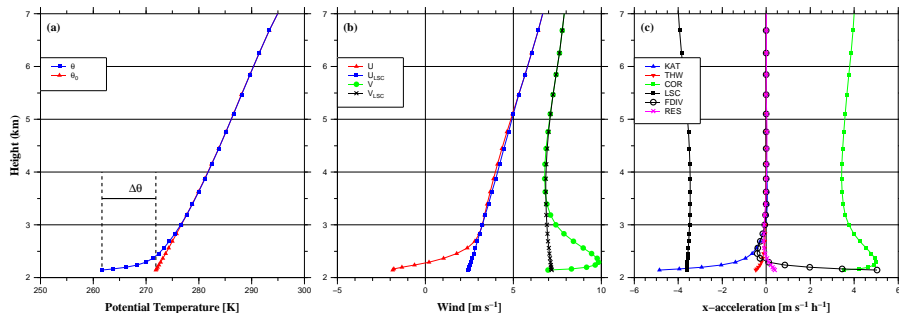


**Figure 2.6:** Transect through North Greenland for the winter months (see Fig. 2.5); a: potential temperature and wind speed, b: momentum budget components in the lowest model layer ( $\sim 7$  m). Vertical lines indicate positions of profiles presented in Figures 2.2, 2.7 and 2.8.

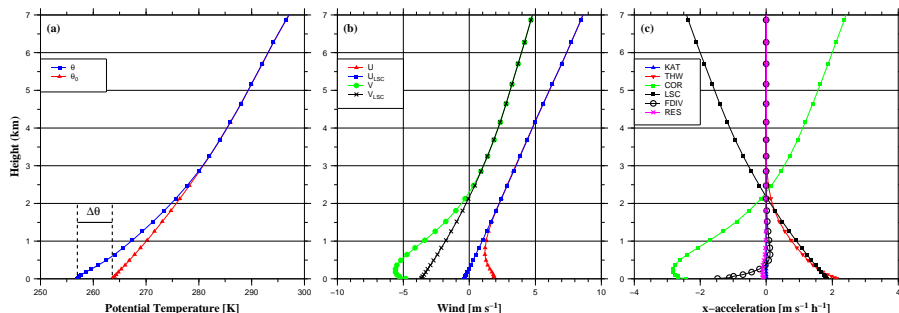
with a sharp wind speed maximum close to the surface ( $7 \text{ m s}^{-1}$ ). Due to surface friction and the downslope large scale flow, the wind has a significant component in the downslope (U) direction, whereas on the west side of the ice sheet the jet is directed more along the height contours (Figure 2.3b).

Figure 2.8 shows wintertime vertical profiles above the (sea ice covered) ocean between 100 and 150 km offshore in the NE sector (blue area in Figure 2.5). The temperature profiles show a thick layer of cold air, which has accumulated over the flat, sea ice covered ocean. As a result, the TDL is more than 2 km deep, much deeper than over the ice sheet. Because of the pronounced gradient in  $|\hat{\theta}|$ , THW is very significant in the boundary layer momentum budget (Figure 2.8c), with a forcing of  $2 \text{ m s}^{-1} \text{ h}^{-1}$  at the surface. LSC has a similar magnitude and is also acting in the E-W direction. As a result, a persistent northerly flow is present throughout the boundary

## 2. Momentum budget of the atmospheric boundary layer over the Greenland ice sheet and its surrounding seas



**Figure 2.7:** Average 1962-2007 (DJF) vertical profiles for the 150-175 km inland bin in the NW (green area in Figure 2.5); a) potential ( $\theta$ ) and background potential temperature ( $\theta_0$ ), b) (large scale) wind components and c) the momentum budget components. Local gridpoint surface elevation 2.2 km.



**Figure 2.8:** Average 1962-2007 (DJF) vertical profiles for the 100-150 km offshore bin in the NE (blue area in Figure 2.5); a) potential ( $\theta$ ) and background potential temperature ( $\theta_0$ ), b) (large scale) wind components and c) the momentum budget components.

layer, with a wind speed maximum of up to  $6 \text{ m s}^{-1}$ , and a difference between real and large scale wind of  $3 \text{ m s}^{-1}$ .

The momentum budget along the transect at the lowest model layer (Figure 2.6b), together with the vertical profiles just discussed, can be used to explain the wind distribution in Figure 2.6a. Over the ice sheet, katabatic forcing (KAT) is the dominant component of the near-surface momentum budget. Although the magnitude of KAT is largest in the steep coastal regions, wind speeds do not necessarily peak there. Especially on the east coast, THW is an important opposing force. The large scale



pressure gradient force (LSC) in the x-direction is important over the western ice sheet but rather small on the east side; this is reflected in wind speed maxima that occur at a greater height above the surface than over the eastern ice sheet. To both sides of the ice sheet, colder air is present to the west, and the magnitude of THW peaks in these areas (Figure 2.6b). Along the east coast, LSC is enhancing THW, explaining the southward jet over the sea ice covered ocean (Figure 2.8b). This jet reaches up to 2 km into the atmosphere, and is as deep as the layer of cold air. Along the northern transect the residual component (RES) is quite small (Figure 2.6b), which indicates the successful separation of the components in the momentum budget and underlines that horizontal and vertical advection and model diffusion are small on the time scales used in this study.

## 2.4 Results: summer

### 2.4.1 Pressure, wind and temperature

In the summer months (June, July, August) the 500 hPa height contours (Figure 2.9a) show a much weaker and more westerly upper air flow over and around the Greenland ice sheet. As in winter, the pressure ridge over the GrIS is also present in summer. At the surface, the Icelandic Low is less deep. The near-surface winds (Figure 2.9b) are weaker than in winter, but still have high directional constancy over the ice sheet, indicative of non-zero katabatic forcing. Due to the high albedo of the ice sheet and nocturnal cooling, a temperature deficit remains present in the summer months and reaches up to 6-8 K in the NE (Figure 2.9c). In ice free regions, a weakly positive value of  $\Delta_\theta$  indicates convection over the snow free tundra. Although sea ice is only present along the far NE coast, there is still a strong temperature deficit (6 K) over the coastal waters, which indicates the presence of warm air being advected over and cooled by cold water, deriving from melting sea ice, advection of cold arctic waters from the north and runoff from the ice sheet. The positive values of  $\Delta_\theta$  that were found in winter over the Atlantic Ocean south of Greenland are not present in summer. This indicates that the ocean is colder than the atmosphere, resulting in a stable boundary layer. For  $\hat{\theta}$  (Figure 2.9d) the most pronounced difference compared to winter is the absence of the pronounced E-W gradients along the east and west coasts. Furthermore, values over the ice sheet are smaller, reflecting weaker radiative cooling.

## 2. Momentum budget of the atmospheric boundary layer over the Greenland ice sheet and its surrounding seas

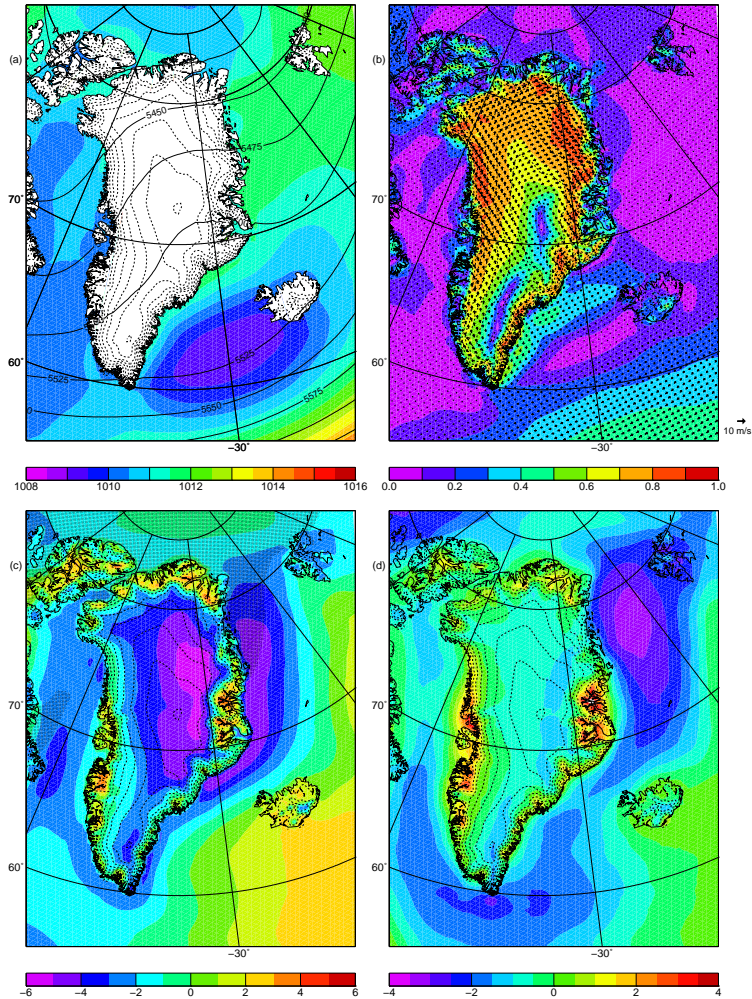


**Figure 2.9:** Averaged summertime (JJA) (a): sea-level pressure [hPa], 500 hPa height [m]. (b): Summertime 10 m winds [ $m s^{-1}$ ] and directional constancy, arrows every 9 gridpoints. (c): Surface temperature perturbation [K]; dotted area represents ocean with more than 50% sea ice concentration. (d): Vertically integrated potential temperature perturbation [ $10^3 K m$ ]. Dashed contours are 400 m surface elevation intervals.

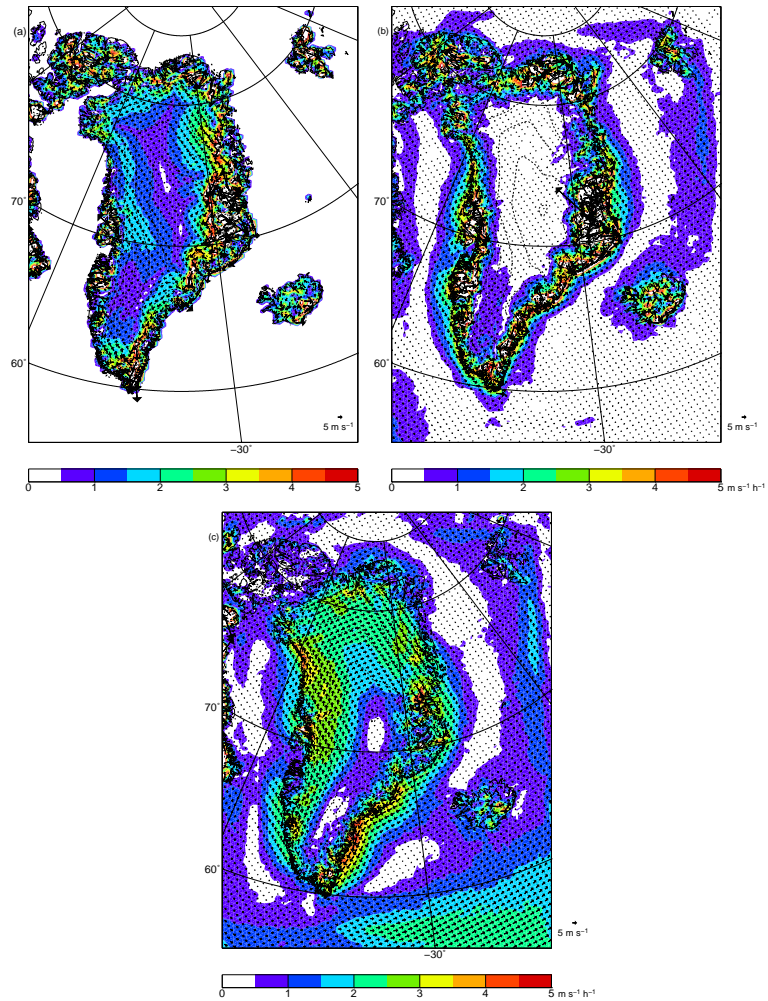


**Figure 2.10:** Spatial distribution of summer averaged magnitude of KAT (a), THW (b), LSC (c) for the lowest model layer ( $\sim 7m$ ). Arrows indicate the associated geostrophic winds.

### 2.4.2 Momentum budget

Over the ice sheet a weaker katabatic forcing is found in summer compared to winter (Figure 2.10a). For example, values around  $2 \text{ m s}^{-1} \text{ h}^{-1}$  are found over the western slopes, compared to  $10 \text{ m s}^{-1} \text{ h}^{-1}$  in winter. Spatial patterns of KAT-forced geostrophic winds are similar: a clockwise atmospheric circulation with increasing magnitude towards the coast. In the coastal regions, THW (Figure 2.10b) again represents an opposing force to KAT. Over the ocean, THW is small at the surface; sea ice, the main source of radiative cooling in winter, is not present in summer, so that the atmosphere is no longer insulated from the ocean. As a result, THW only forces rather weak regional atmospheric circulations over the ocean. In a small band around the ice sheet, nonzero THW forcing can be ascribed to heating of the tundra and relatively colder air over the ocean (sea-breeze effect). The resulting PGF is directed towards the coast, driving an anti-clockwise circulation. Although weaker than in winter, LSC (Figure 2.10c) is now relatively more important in the momentum budget, with patterns comparable to winter: a clockwise atmospheric circulation is found as a result of the high pressure over the ice sheet due to the radiative cooling of the free troposphere. Over the ocean, the strongest forcing by LSC (up to  $5 \text{ m s}^{-1} \text{ h}^{-1}$ ) is again found along the SE coast.

### 2.4.3 Northern transect

Figure 2.11a displays potential temperature and wind speed for the northern cross section (Figure 2.5) in the summer months. Figure 2.12 shows vertical profiles for the 150-175 km inland bin in the NW sector (green area in Figure 2.5). Over the GrIS the jets over the east and west flank are still present in summer, but weaker, with maximum wind speeds of  $7 \text{ m s}^{-1}$ . On the westside in summer, LSC is now the dominant forcing (Figure 2.11b, 2.12b). The reason is that the TDL is less developed in summer, and  $|\Delta\theta|$  at the surface is less than 3 K, resulting in relatively small magnitude of KAT ( $\sim 1 \text{ m s}^{-1} \text{ h}^{-1}$ ). Otherwise, the wind profiles look rather similar to winter, with upper air winds from the southwest and the katabatic maximum in the TDL of  $5.5 \text{ m s}^{-1}$ . The same qualitative results hold for the east side (not shown).

Over the ocean (Figure 2.13) the layer of cold air is more shallow in summer, with a depth of less than 1 km. A THW signal is however still present in the momentum budget, but it is now directed towards the coast. Since LSC works in the opposite direction, average near-surface winds are weak. A closer look at the summertime momentum budget in the coastal areas show some interesting features. First of all, KAT in Figure 2.11b changes sign on the east side, because the ice and snow free

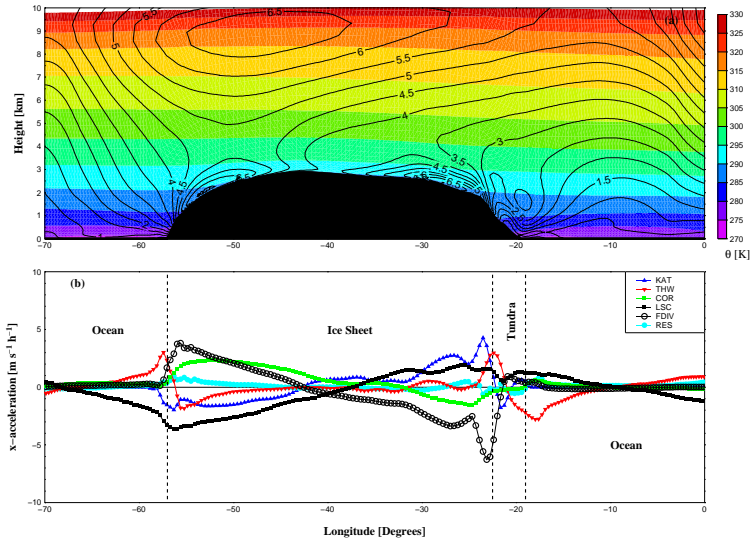


**Figure 2.11:** Transect through North Greenland for the summer months (see Figure 2.5). a: potential temperature and wind speed. b: momentum budget components in the lowest model layer ( $\sim 7\text{m}$ ).

tundra is heated, resulting in a positive  $\Delta\theta$ . This availability of warm air also has its effect on THW. With relatively cold air above the melting ice sheet margins, warm air over the tundra and cold air again over the ocean, THW changes sign over the tundra (Figure 2.11b). In the northern half of Greenland, this effect is most pronounced in the east and far north, where the tundra is widest and summer insolation greatest. In the southern half of Greenland, the effect is most pronounced in the wide strip of ice free tundra in the west. The associated barrier flow has been observed over the western tundra and melting zone during the GIMEX-90/91 field campaigns (*Van den Broeke and Gallée, 1996*).

## 2.5 Conclusions

We use 45 years of output from a high resolution regional atmospheric climate model to explicitly calculate the driving forces behind the atmospheric circulation over Greenland and its surrounding seas. In winter (DJF), the ice sheet surface cools the near-surface air, forcing the characteristic katabatic winds. However, the large scale

## 2. Momentum budget of the atmospheric boundary layer over the Greenland ice sheet and its surrounding seas

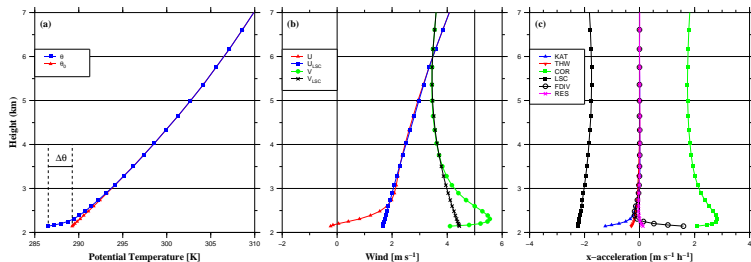


**Figure 2.12:** Average 1962-2007 (JJA) vertical profiles for the 150-175 km inland bin in the NW (green area in Figure 2.5); a) potential ( $\theta$ ) and background potential temperature ( $\theta_0$ ), b) (large scale) wind components and c) the momentum budget components. Local gridpoint surface elevation 2.2 km.

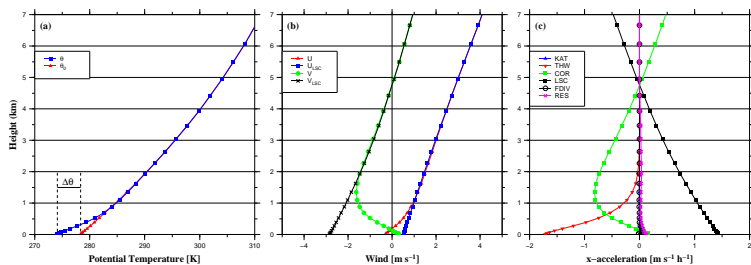


**Figure 2.13:** Average 1962-2007 (JJA) vertical profiles for the 10-50 km offshore bin in the NE; a) potential ( $\theta$ ) and background potential temperature ( $\theta_0$ ), b) (large scale) wind components and c) the momentum budget components.

circulation also plays a major role in the momentum budget over the western slopes of the ice sheet. Hence, the large scale and katabatic pressure gradient forces drive a strong and persistent low level jet, the so called Greenland Plateau Jet that was recently identified. Over the eastern slopes, katabatic forcing dominates. In the summer months (JJA) the large scale forcing is weaker than in winter but more dominant in the momentum budget, because katabatic forcing has decreased even more. In spite of this, a persistent low level jet with katabatic characteristics, is still found over both the western and eastern slopes. This jet is associated with katabatic forcing through the melting ice surface and nocturnal cooling.

Important atmospheric circulation patterns are also identified over the surrounding oceans. Although the wintertime upper air circulation is persistently from the

southwest, surface winds over the Greenland Sea along the NE coast are mainly from the north. This circulation is driven by cold air that originates from the ice sheet and accumulates over the sea ice. The associated pressure perturbation (thermal wind) forces a southward jet along the Greenland coast, which represents an important mechanism for southward sea ice transport. Along the west coast, where colder air over the Canadian islands and warmer air over the open waters along the Greenland west coast meet, a similar thermally induced northerly flow is found. In the summer months, these thermally induced circulation patterns are not present over the ocean. Heating of the snow free tundra, however, forces thermally driven barrier flows along the tundra/ocean and tundra/ice sheet transition zones.

Finally, according to our analysis, the persistent winds along the SE coast of Greenland are of large-scale origin, both during winter- and summertime.

3





# The Greenland Sea Jet: A mechanism for wind-driven sea ice export through Fram Strait

---

*We present a mechanism for wind-driven sea ice export from the Arctic Ocean through Fram Strait for the period 1979-2007, using the output of a high-resolution regional atmospheric climate model. By explicitly calculating the components of the atmospheric momentum budget, we show that not large scale synoptic forcing (LSC), but mainly thermal wind forcing (THW) causes the persistent northerly jet (the Greenland Sea Jet) over Fram Strait. The jet results from horizontal temperature gradients in the atmospheric boundary layer (ABL), set up between cold ABL-air over the sea ice covered western Greenland Sea and the relatively warmer ABL over the ice-free eastern Greenland Sea. From 1993 onwards we find a negative trend in THW, due to a stronger response to climate warming of the ABL over the sea ice covered ocean, compared to that over the ice free ocean. Although on average LSC is smaller than THW, year to year variations in LSC explain most of the inter-annual variability in the sea ice area flux through Fram Strait ( $R = 0.81$ ). A small positive trend is found for LSC, partly compensating the decrease in THW in recent years.*

## 3.1 Introduction

Sea ice forms an important component of the Arctic climate system. It reflects a significant amount of incoming solar radiation, limits the interaction between ocean and atmosphere and the relatively fresh meltwater impacts ocean circulation. Since the start of continuous observations in 1979 (*Johannessen et al.*, 2004; *Parkinson and Cavalieri*, 2008), Arctic sea ice extent has strongly decreased, especially in summer with record low values in 2005 and 2007 (*Comiso*, 2006; *Comiso et al.*, 2008). Recent years also saw a decline in winter ice extent (*Comiso*, 2006), with a record low January 2011 extent of  $13.55 \times 10^6 \text{ km}^2$ , 8.5% less than the 1979-2000 average [<http://nsidc.org>].

Although direct melt also is a significant factor (*Kwok and Cunningham*, 2010), export through Fram Strait (FS) is the dominant sink for Arctic sea ice (*Kwok*, 2009; *Kwok et al.*, 2004). Variations in sea ice export are related to the surface pressure gradient over FS (*Hilmer et al.*, 1998; *Koenigk et al.*, 2006; *Kwok et al.*, 2004; *Lemke and Hilmer*, 1998; *Tsukernik et al.*, 2009; *Vinje*, 2001), motivating several studies that investigated the relation between FS sea ice export and variability in atmospheric circulation patterns. No consistent relations were found between the North Atlantic Oscillation (NAO) (*Jung and Hilmer*, 2001; *Kwok et al.*, 2004), the Arctic Oscillation (AO) (*Rigor et al.*, 2002; *Wu et al.*, 2006), cyclone activity (*Brümmer et al.*, 2001, 2003) and FS sea ice export. None of these studies completely explained the persistent west-east pressure gradient over Fram Strait, with the associated northerly geostrophic wind over the Greenland Sea (GS) (Figure 3.1).

Here, we explicitly resolve the components of the lower atmospheric momentum budget over the GS region, to provide a theoretical framework for year-to-year variations in wind-driven sea ice export through FS. For this, we use output of the high resolution regional atmospheric climate model RACMO2.1/GR (*Van Meijgaard et al.*, 2008), for the period 1979-2007, and yearly averaged sea ice area flux data through FS (1979-2007) (*Kwok*, 2009). The next section briefly describes the climate model output and sea ice data used. The calculation of the momentum budget components is also discussed. Section 3.3 gives results of the momentum budget components and the relation to sea ice export. Conclusions are given in section 3.4.

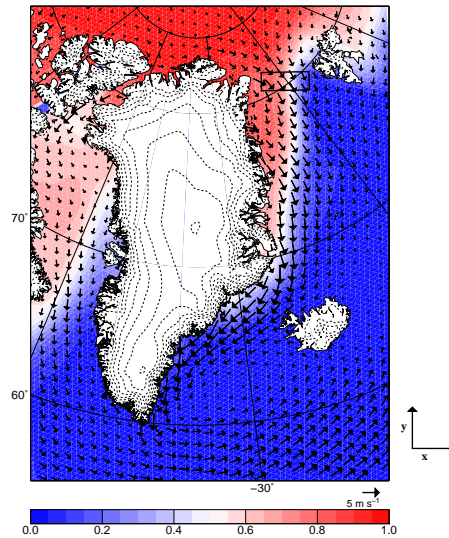


**Figure 3.1:** Average (1979-2007) sea ice concentration (color) and near-surface winds. The square defines the FS area as used in this study. Dashed contours are 400 m surface elevation intervals.

## 3.2 Methods

### 3.2.1 Data

For this study we use output of the regional atmospheric climate model RACMO2.1/GR for the period 1979-2007 (Van Meijgaard *et al.*, 2008). Figure 3.1 shows the full model domain, covering Greenland and its surrounding oceans. RACMO2.1/GR is a hydrostatic model, has a horizontal grid spacing of 11 km and 40 sigma levels in the vertical. The quality of the model output has been extensively evaluated in *Ettema et al.* (2010a), and the model has been successfully used for atmospheric boundary layer studies in Antarctica (Van de Berg *et al.*, 2008; Van den Broeke and van Lipzig, 2003; Van den Broeke *et al.*, 2002) and Greenland (Van Angelen *et al.*, 2011a). RACMO2.1/GR is forced at the lateral boundaries by ECMWF reanalysis (ERA-40) data every 6 hours (Uppala *et al.*, 2005). From August 2002 onwards, operational data of the ECMWF are used. Sea ice cover and sea surface temperature are also prescribed from ERA-40.

Yearly averaged (September to October) sea ice area fluxes through FS for the 1979-2007 period were determined by combining sea ice motion and sea ice concentration retrievals from satellite data (Kwok, 2009). The average area flux of sea ice through FS is  $706 \times 10^3 \text{ km}^2 \text{ yr}^{-1}$ , with a standard deviation of  $113 \times 10^3 \text{ km}^2 \text{ yr}^{-1}$ . The uncertainty in the annual estimates is  $28 \times 10^3 \text{ km}^2$ .

### 3.2.2 Momentum Budget

Over a flat surface, the momentum budget in the x-direction can be approximated as follows:

$$\frac{\partial U}{\partial t} = -\overbrace{U \frac{\partial U}{\partial x} - V \frac{\partial U}{\partial y}}^{\text{HADV}} - \overbrace{W \frac{\partial U}{\partial z}}^{\text{VADV}} + \frac{g}{\theta_0} \frac{\partial \hat{\theta}}{\partial x} + fV - fV_{LSC} - \frac{\partial \overline{uw}}{\partial z}, \quad (3.1)$$

with  $U$  and  $V$  the wind velocity components in the x- and y-direction, and  $\theta_0$  the background potential temperature, which is calculated by linearly extrapolating the potential temperature in the free troposphere towards the surface.  $\hat{\theta}$  is defined as the vertically integrated temperature perturbation of the temperature deficit layer (TDL):

$$\hat{\theta}(z) = \int_z^{h_f} \Delta_\theta(z) dz, \quad (3.2)$$

with  $\Delta_\theta(z) = \theta(z) - \theta_0(z)$ , the temperature perturbation.  $h_f$  is chosen well above the TDL top in the free atmosphere. For this study we adopted the coordinate system as used in the RACMO2.1/GR model;  $U$  wind is in the x-direction as displayed in Figure 3.1 and not the easterly component. In this paper we present results for the lowest model layer at approximately 7 m above the surface.

Equation 3.1 contains two active forcing components, the thermal wind (THW) and the large scale (LSC) forcing. Near the surface, LSC depends on the strength and direction of the flow above the TDL ( $U_{LSC}$  and  $V_{LSC}$ ) and on the vertical gradient in the background potential temperature ( $\theta_0$ ) via the thermal wind balance. THW is driven by horizontal gradients in  $\hat{\theta}$ , i.e. horizontal gradients in the ‘cold content’ of the TDL. Chapter 2 provides a detailed discussion of LSC, THW,  $\theta_0$  and  $\hat{\theta}$  over the larger Greenland region. The other terms (horizontal and vertical advection (HADV, VADV), the coriolis force (COR) and momentum flux divergence (FDIV) are passive forces, i.e. they only become important once flow has been initiated.

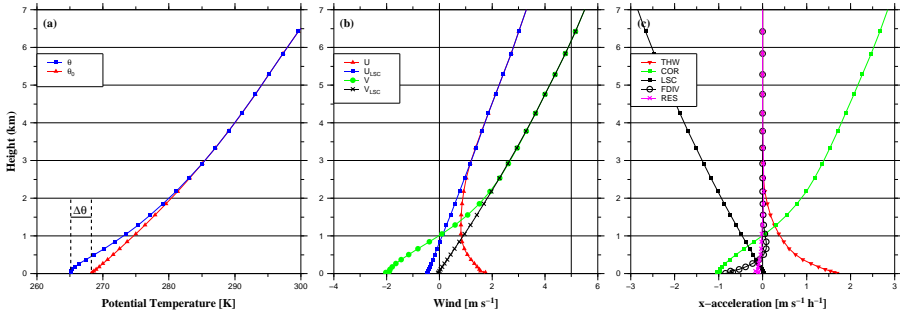


**Figure 3.2:** Average vertical profiles over FS for the period October 1999 to September 2000 of a) potential ( $\theta$ ) and background potential temperature ( $\theta_0$ ), b) (large scale) wind components and c) the momentum budget components.

## 3.3 Results

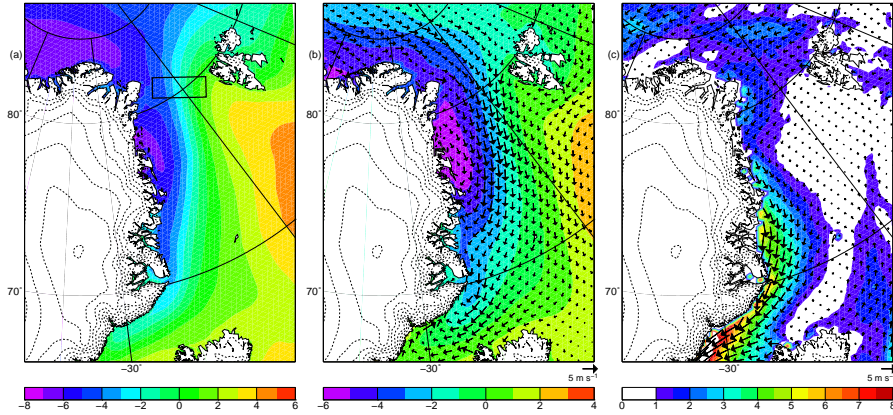
### 3.3.1 Vertical Profiles

Figure 3.2 shows average vertical profiles of  $\theta$  and  $\theta_0$  (a),  $U$  and  $V$  (b) and the momentum budget components (c) over FS for the period October 1999 to September 2000.  $\theta$  starts to deviate from  $\theta_0$  approximately 2.5 km above the surface (Figure 3.2a), signifying the large depth of the TDL. This is also the level where  $U$  and  $V$  start to deviate from their large scale components (Figure 3.2b). Large scale winds in the free troposphere are from the southwest and become near-zero close to the surface. In the free troposphere, the momentum budget (Figure 3.2c) shows a simple geostrophic balance. Closer to the surface, however, the momentum budget is dominated by THW, which drives a persistent northerly jet over FS and the Greenland Sea. Figure 3.1 clearly identifies this boundary-layer jet (70-85°N), which from now on we will refer to as the Greenland Sea Jet (GSJ).

### 3.3.2 Momentum Budget

Figure 3.3a shows the average surface temperature perturbation ( $\Delta\theta$ ) over the region of interest. The strongest negative perturbations are found over the sea ice, with values of up to -7 K along the north and northeast coast of Greenland; cold air from the ice sheet transported by katabatic winds (Chapter 2) accumulates over the sea ice covered ocean, and can maintain its low temperature owing to the insulating properties of the sea ice.  $\Delta\theta$  increases away from the coast, reaching positive values of up to 5 K

### 3. The Greenland Sea Jet: A mechanism for wind-driven sea ice export through Fram Strait



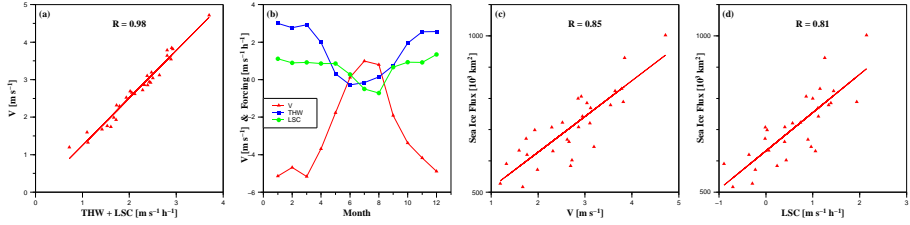
**Figure 3.3:** Average (1979-2007) a) Surface temperature perturbation [K] ; b) Vertically integrated temperature perturbation [ $10^3 \text{ Km}$ ] and geostrophic winds associated with THW forcing; c) LSC forcing [ $\text{m s}^{-1} \text{ h}^{-1}$ ] and associated geostrophic winds. Wind vectors are plotted every 20th model grid point.

over the eastern Greenland Sea, where the ocean surface is sea ice free throughout the year. Here, the air is colder than the relatively warm sea surface, leading to a positive temperature perturbation at the surface.

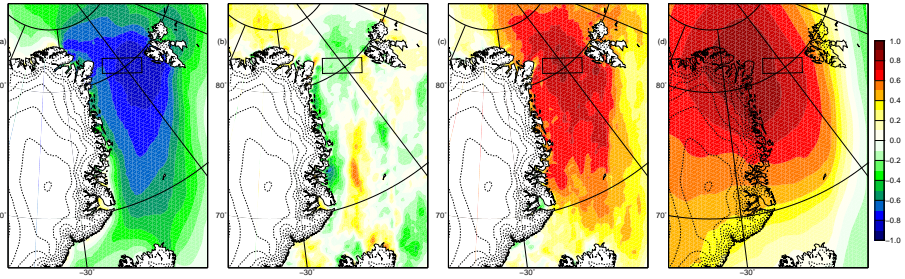
The vertically integrated temperature perturbation  $\hat{\theta}$  (Figure 3.3b) shows the same features, with a pool of cold air over the western Greenland Sea. The associated gradient in  $\hat{\theta}$  results in THW forcing of up to  $2 \text{ m s}^{-1} \text{ h}^{-1}$ . If balanced by COR, this forces a northerly geostrophic near-surface wind of up to  $5 \text{ m s}^{-1}$ , representing the GSJ. The GSJ is strongest over FS and the central Greenland Sea, coinciding with the boundary between the sea ice covered and sea ice free ocean (Figure 3.1).

Figure 3.3c displays LSC and the associated geostrophic wind. Although LSC is important in the higher atmosphere (Figure 3.2b), it is on average small near the surface in the FS region, less than  $2 \text{ m s}^{-1} \text{ h}^{-1}$ . LSC becomes large along the east coast further south, which explains the far southward extent of sea ice along the east coast of Greenland, and is in agreement with the findings during the Greenland Flow Distortion Experiment (Petersen *et al.*, 2009).

Figure 3.4a shows that yearly averaged total forcing in the x-direction (THW + LSC) is a very robust predictor of the yearly averaged wind in the y-direction (V) over FS. V varies between 1 and  $5 \text{ m s}^{-1}$ , and this inter-annual variability is fully explained by variations in total forcing ( $R = 0.98$ ). The seasonal variability in V is pronounced



**Figure 3.4:** a) Yearly average values over FS for wind forcing vs. wind speed; b) Average seasonal variation in  $V$ , THW and LSC; c) Yearly average values for windspeed vs. sea ice flux and d) Yearly average values for LSC vs. sea ice flux.



**Figure 3.5:** Correlation fields of annual total sea ice flux through FS with: a)  $V$  (wind in the  $y$ -direction); b) Thermal wind forcing (THW) near the surface; c) Large scale forcing (LSC) near the surface; d) Large scale forcing in the free troposphere ( $\sim 5000$  m height).

(Figure 3.4b), with strongest southward winds in winter up to  $5 \text{ m s}^{-1}$  and a weak northward flow in summer ( $1 \text{ m s}^{-1}$ ). This seasonality can be ascribed to both THW and LSC forcing, with a dominant contribution of THW (Figure 3.4b). In summer, a combination of less sea ice cover along the Greenland coast and weaker katabatic winds from the ice sheet, diminishes the accumulation of cold air in this region. As a result, the gradient of  $\theta$  in the offshore direction is small, resulting in a weaker or absent GSJ.

### 3.3.3 Sea Ice Area Flux Through FS

Figure 3.4c shows the correlation and Figure 3.5a the correlation field of yearly averaged  $V$  with the sea ice area flux through FS. Correlation magnitude is largest over the eastern FS, close to Svalbard. Correlations are strong over the entire Greenland

Sea, indicating a single forcing, in this case the GSJ. Figures 3.5b and c display correlation fields of yearly sea ice fluxes, LSC and THW. THW is the dominant forcing of the GSJ; it is also rather constant from year to year, in contrast to LSC. As a result, no significant correlation exists of THW with the sea ice flux (Figure 3.5b). Figure 3.5c shows that year to year variations in sea ice flux can be mainly ascribed to variations in LSC, with correlation in the FS  $> 0.8$  (Figure 3.4d). By definition, LSC near the surface and in the upper air are strongly connected. As a result, correlations between LSC at  $\sim 5000$  m elevation and sea ice flux through FS is still strong (Figure 3.5d). Compared to the surface, the center of action has shifted to the west as a result of the average westward tilt of the pressure field with height in response to the large scale SE-NW temperature gradient over Greenland. These results are not sensitive to the size or location of the FS averaging window.

#### 3.3.4 Temporal Variability

Figure 3.6 shows 1979-2007 time series of annual total sea ice fluxes through FS and annual average THW and LSC: No significant trend in sea ice export is present; inter-annual variability is large ( $\sigma = 16\%$ ) and driven by LSC (red line); THW (blue line) is relatively constant from year to year. The pool of cold air that sets up THW is continuously replenished by katabatic winds flowing off the ice sheet, which is a rather steady phenomenon in NE Greenland. Moreover, large scale winds that may disperse the cold air are weak in this region (Figure 3.3c).

Between 1979 and 1993, THW is rather constant and significantly larger than LSC. From 1993 onwards, a downward trend in THW is visible, which is significant at the 99% level. This trend is the result of the different response of the ABL to upper air warming over a sea ice covered ocean, compared to a sea ice free ocean. Figure 3.6b compares the temperature trend over the west and east side of FS, close to the surface and at 500 hPa (for the definition of the east and west side of FS, see Fig. 3.7). Upper air temperatures show a strong increase of  $+0.9$  K/decade from 1993 onwards, both on the west and on the east side of FS. Close to the surface, temperature trends are much more variable. Over the almost continuously sea ice covered west side of FS we find a positive trend of  $+0.7$  K/decade (similar to the upper air trend), compared to a negative trend of  $-0.4$  K/decade on the east side. This negative trend is the result of a small increase in sea ice cover in recent years over the east side of FS, limiting the heating of the ABL by the ocean. As a result of this differential heating over FS, the gradient in  $\hat{\theta}$  is reduced, leading to a weakening of THW. Temperature trends for the entire region are shown in Figure 3.7. In general, temperature trends are strongest over sea ice covered regions (up to  $+1.5$  K/decade), whereas over the ice free



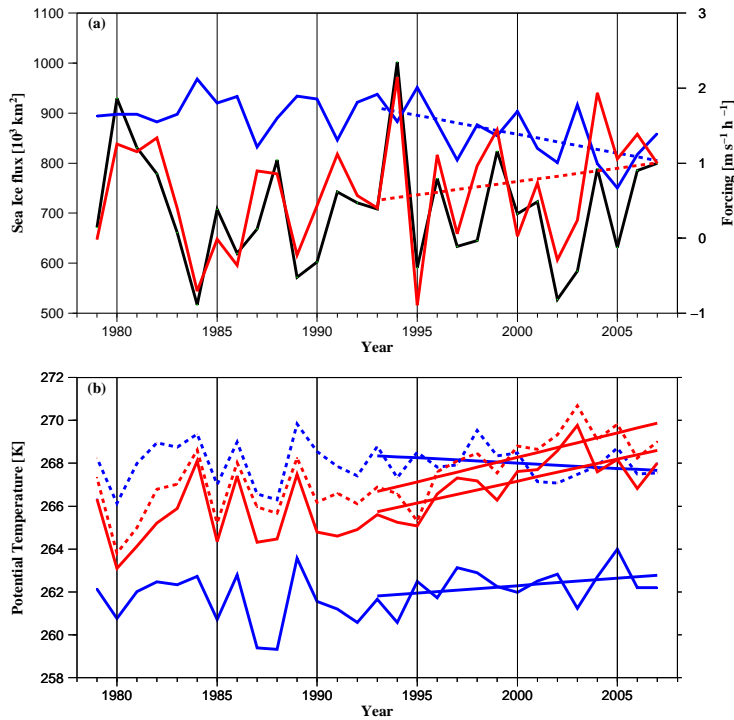


**Figure 3.6:** Yearly averaged values for a) sea ice flux through Fram Strait (black), LSC (red) and THW (blue); b) Yearly averaged temperature at 500 hPa (red) and near the surface (blue) over the western (solid) and eastern (dashed) FS.

ocean trends are reduced due to the large heat capacity of the ocean water column. These findings are in agreement with the strong surface heating in the Arctic region in wintertime and reduced heating in summertime (Graversen *et al.*, 2008), as a result of the seasonality in sea ice cover. The weakening of THW is partly compensated by a (less significant) positive trend in LSC.

### 3.4 Conclusions

These results show that FS sea ice export is maintained by the GSJ, forced by the pooling of cold air, that originates from the Greenland ice sheet, over sea ice in the

### 3. The Greenland Sea Jet: A mechanism for wind-driven sea ice export through Fram Strait

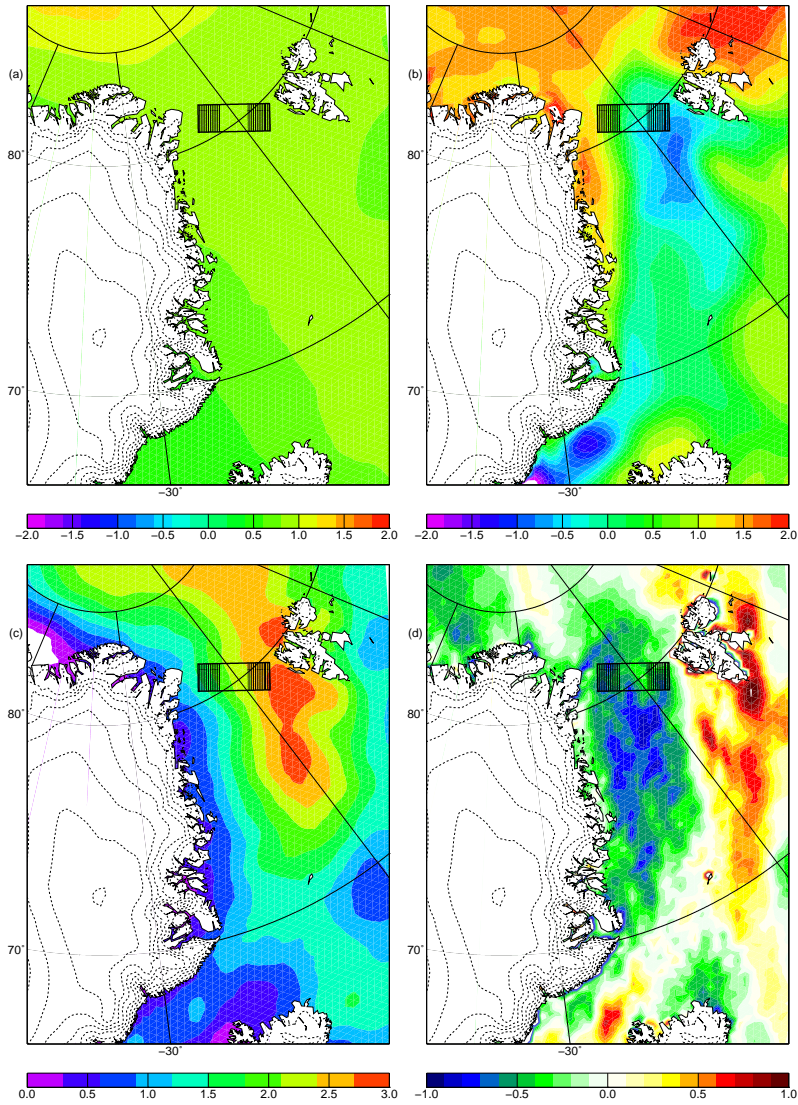


**Figure 3.7:** Trend (1993-2007) in a) 500 hPa temperature [K/decade]; b) surface temperature [K/decade]; c) integrated temperature perturbation [ $10^3$  K m/decade] and d) THW [ $2 \text{ m s}^{-1} \text{ h}^{-1}$ /decade]. The square defines the averaging area over FS, the hatched parts defines the east and west sides of FS.

western GS, and the absence of this pooling further east over the open ocean. This implicates that in the absence of sea ice in FS, or when the FS was uniformly covered by sea ice, the southward transport by the GSJ would be less efficient, which is qualitatively supported by the absence of THW in summer. This represents a negative feedback of Arctic sea ice decline.

The fact that the atmospheric boundary layer plays a pivotal role in FS sea ice transport implicates that thermal adjustment with the surface is important in explaining long term variability. In the case of the rapidly warming free atmosphere over the GS and Greenland, this has led to a weakening of the THW over FS, which represents another negative feedback on Arctic Sea ice loss.

A close-up, high-angle photograph of a glacier's surface. The ice is heavily crevassed, forming a complex, textured pattern of ridges and valleys. The color is a pale, milky blue, with some darker, brownish streaks visible in the crevasses, likely due to sediment or rock fragments. A large, bold, black number '4' is superimposed on the left side of the image, partially overlapping the ice's texture.

4

# Sensitivity of Greenland ice sheet surface mass balance to surface albedo parameterization: a study with a regional climate model

---

*We present a sensitivity study of the surface mass balance (SMB) of the Greenland ice sheet, as modeled using a regional atmospheric climate model, to various parameter settings in the albedo parameterization. The snow albedo parameterization uses grain size as a prognostic variable and further depends on cloud cover, solar zenith angle and black carbon concentration. For the control experiment the overestimation of absorbed shortwave radiation (+6%) at the K-transect (west Greenland) for the period 2004-2009 is considerably reduced compared to the previous density-dependent albedo parameterization (+22%). To simulate realistic snow albedo values, a small concentration of black carbon is needed. A background ice albedo field derived from MODIS imagery improves the agreement between the modeled and observed SMB gradient along the K-transect. The effect of enhanced retention and refreezing is a decrease of the albedo due to an increase in snow grain size. As a secondary effect of refreezing the snowpack is heated, enhancing melt and further lowering the albedo. Especially in a warmer climate this process is important, since it reduces the refreezing potential of the firn layer covering the Greenland ice sheet.*

## 4.1 Introduction

Mass loss from the Greenland ice sheet (GrIS) is expected to become a major contributor to sea level rise this century (IPCC-AR4). After a 30 year period (1960-1990) during which the GrIS was in approximate mass balance (i.e. the mass gain by precipitation was approximately equal to the mass loss by surface runoff and ice discharge), the mass balance has turned negative in the last 20 years, with a larger melt extent (*Fettweis et al.*, 2011), increasing surface runoff (*Ettema et al.*, 2009; *Hanna et al.*, 2008) and increased glacier discharge (*Nick et al.*, 2009; *Rignot et al.*, 2011). In the last decade, the contributions made to the total mass loss of ~2400 Gt, were for ~ 60% accounted for by enhanced runoff and for ~ 40% by enhanced discharge (*Rignot et al.*, 2008a; *Van den Broeke et al.*, 2009). With outlet glaciers retreating and near-surface air temperature increasing further, mass loss in the near future will likely remain dominated by surface runoff.

The most important energy source for surface runoff is the absorption of solar radiation (*Van den Broeke et al.*, 2008a), which is mainly determined by cloud cover and surface albedo. Modeled surface mass balance (SMB) of the GrIS is highly sensitive to surface albedo (*Bougamont and Bamber*, 2005; *Fitzgerald et al.*, 2012; *Tedesco et al.*, 2011), owing to the positive melt-albedo feedback, which results in lower albedos in high-melt years (*Stroeve*, 2007). Following recent warming, a persistent drop in albedo has been observed in satellite data and climate models (*Box et al.*, 2012b).

Any physically-based approach to project future GrIS mass balance requires a high resolution climate model that represents surface albedo adequately, including all processes that influence its evolution (*Bougamont et al.*, 2007). For a proper interpretation of SMB projections it is essential to understand the physical processes in the snowpack, their influence on albedo and ultimately on the surface mass balance.

In this chapter we address the sensitivity of the SMB of the GrIS to changes in the different parameter settings of a particular albedo parameterization scheme. For this we use the high resolution climate model RACMO2 (*Ettema et al.*, 2010a; *Van Meijgaard et al.*, 2008), recently extended with a new albedo parameterization scheme (*Kuipers Munneke et al.*, 2011). The next section will briefly describe in situ albedo observations, RACMO2 and the albedo parameterization and lists the sensitivity tests performed in this study. Results are discussed in section 4.3 and conclusions and a future outlook is given in section 4.4.

## 4.2 Data and methods

### 4.2.1 AWS Observations

Since 1990, the Institute for Marine and Atmospheric research Utrecht (IMAU) has performed mass balance and meteorological measurements along a transect (Kangerlussuaq transect or K-transect), located on the western margin of the GrIS at 67°N (Van de Wal *et al.*, 2005). The ablation area here is up to 150 km wide with gentle slopes, representing the largest ablation region of the GrIS. In August 2003, three automatic weather stations were installed along the transect (Van den Broeke *et al.*, 2008a), indicated by the three black dots in the inset of Figure 4.1. The measurements of incoming and outgoing shortwave radiation are used for evaluation of RACMO2. The lowest station (S5) is located ~5 km from the ice sheet margin at an altitude of 420 m. This site experiences an average mass loss of ~3.5 m of water equivalent (m w.e.) per year. Station S6 is located ~40 km from the margin, at an altitude of approximately 1000 m, in rough terrain with meltwater channels in summer (Figure 4.2a) and an average mass loss of ~2 m w.e. year<sup>-1</sup>. Station S9 (Figure 4.2b) is situated ~80 km from the margin, at an altitude of around 1500 m. At the onset of the stake measurements, S9 was close to the equilibrium line, but in the most recent 5 years an average mass loss of 0.5 m w.e. year<sup>-1</sup> has been observed here. In this study only data from stations S6 and S9 are used, because S5 is located on the outlet of Russell Glacier, which is not resolved in RACMO2.

### 4.2.2 Melt days

As a second evaluation method, we use the amount of melting days in the summer of 2007 based on satellite retrievals. Daily values of brightness temperature from the Special Sensor Microwave/Imager (SSM/I) F-13 (1995-2009) are regridded on a 25 x 25 km EASE-grid, as distributed by the National Snow and Ice Data Center (Armstrong and Brodzik, 1995). The brightness temperatures are derived as in Abdalati and Steffen (1997, 2001). As a threshold to determine whether melt is present a brightness temperature of 227.5 K is used, see Fettweis *et al.* (2011).

### 4.2.3 Regional Atmospheric Climate Model

We use the Regional Atmospheric Climate Model (RACMO2) (Van Meijgaard *et al.*, 2008), developed by the Royal Netherlands Meteorological Institute (KNMI). Over the last decade, RACMO2 has been adapted to realistically simulate ice sheet SMB

#### 4. Sensitivity of Greenland ice sheet surface mass balance to surface albedo parameterization: a study with a regional climate model

---

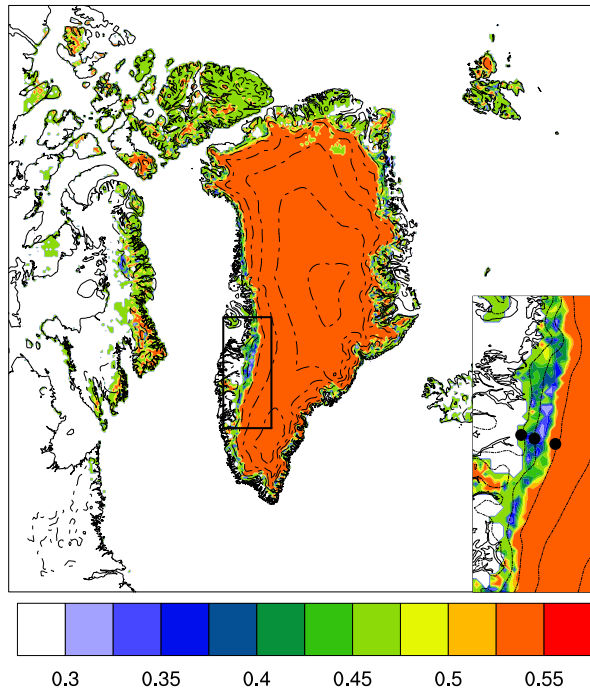


**Figure 4.1:** Domain used in the RACMO2 simulations. The colors denote background ice albedo as derived from MODIS satellite data, with a fixed value of 0.55 assumed for areas currently covered by a permanent snowcover. Contour lines are at a 500 m surface elevation intervals. The area of the K-transect with the locations of the three automatic weather stations is expanded in the inset.

by the implementation of a multilayer snow model (Ettema *et al.*, 2010a) and a drifting snow scheme (Lenaerts *et al.*, 2010). In this study RACMO2 is applied with a horizontal grid spacing of approximately 11 km and 40 sigma levels in the vertical. The domain covers Greenland and its surrounding seas, including the Canadian Arctic Archipelago, Iceland and Svalbard (Fig. 4.1). At the lateral boundaries RACMO2 is forced every 6 hours by ERA-Interim reanalysis data (Simmons *et al.*, 2007). At the surface boundary sea surface temperature and sea ice extent are prescribed. Ettema *et al.* (2010a,b) evaluated RACMO2 for the period 1958-2008 over Greenland. Recently, output of RACMO2 has been successfully used to solve for the total mass budget of the GrIS (Van den Broeke *et al.*, 2009), to describe the momentum budget





**Figure 4.2:** Automatic weather stations along the K-transect in West Greenland. On the left S6, on the right S9. For locations see Figure 4.1. The photographs are taken at the end of August 2011.

of the katabatic boundary layer (*Van Angelen et al.*, 2012) and to explain the wind-driven sea-ice export through Fram Strait (*Van Angelen et al.*, 2011b).

#### 4.2.4 Albedo parameterization

The most important physical property influencing snow albedo is snow grain size (*Wiscombe and Warren*, 1980): larger grains are both more absorptive and scatter solar radiation preferentially in the forward direction, into the snowpack, enhancing the chances that photons are absorbed. Clouds, solar zenith angle and impurities due to soot and dust also have an impact on the albedo. In previous model versions of RACMO2, broadband albedo was snow density-dependent (*Greuell and Konzelmann*, 1994). Although the density of snow is a measure for snow metamorphism, as it increases with increasing grain size, a density dependent albedo scheme is unphysical (*Wiscombe and Warren*, 1980). Especially for wet snow conditions, a density dependent albedo parameterization tends to underestimate albedo, resulting in an overestimation of absorbed solar radiation, and consequently a too early and too long exposure of bare ice at the surface (*Ettema et al.*, 2010a). Figure 4.3 compares measured and modeled albedo at S9, using the previous, density dependent albedo scheme. In reality, only for a short period in August bare ice was present at the surface, whereas the modeled albedo predicts ice at the surface from mid July until the end of September. Too low albedos in June resulted in a rapid melt of the snowcover.

The new albedo parameterization as implemented in RACMO2 is presented in *Kuipers Munneke et al.* (2011), who discusses its successful implementation in RACMO2

4. Sensitivity of Greenland ice sheet surface mass balance to surface albedo parameterization: a study with a regional climate model

---

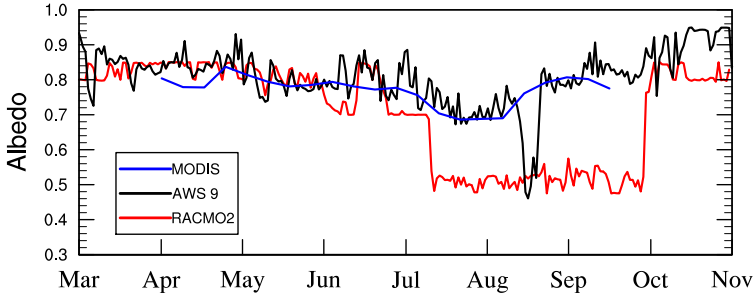


**Figure 4.3:** Surface albedo for the year 2006 at S9 along the K-transect. Black line shows AWS measurements, red line shows RACMO2 results using the previous, density-dependent albedo scheme, and blue shows MODIS-derived albedo.

for the Antarctic ice sheet. The new albedo scheme is based on the parameterization developed by *Gardner and Sharp* (2010), in which a broadband albedo is calculated depending on snow grain size, solar zenith angle, cloud cover and contamination of the snowpack by black carbon:

$$\alpha = \alpha_S + d\alpha_u + d\alpha_c + d\alpha_\tau. \quad (4.1)$$

The final broadband albedo ( $\alpha$ ) is the sum of a base albedo ( $\alpha_S$ ) that depends on snow grain size, corrected for solar zenith angle ( $d\alpha_u$ ), contamination ( $d\alpha_c$ ) and clouds ( $d\alpha_\tau$ ). Solar zenith angle and cloud cover are readily available from RACMO2. *Kuipers Munneke et al.* (2011) introduced a new prognostic variable in RACMO2, the effective snow grain size ( $r_e$ ). The effective snow grain size itself is a mass weighted average of the snow grain size of fresh snow ( $f_n$ ), old snow ( $f_o$ ) and refrozen liquid water ( $f_r$ ) in a snow layer:

$$r_e(t) = [r_e(t-1) + dr_{e,dry} + dr_{e,wet}]f_o + r_{e,0}f_n + r_{e,r}f_r. \quad (4.2)$$

The snow grain size of fresh snow ( $r_{e,0}$ ) and refrozen snow ( $r_{e,r}$ ) is chosen constant in time and space. The grain size of old snow is based on the snow grain size in the previous time step ( $r_e(t-1)$ ) corrected for dry and/or wet snow metamorphism. The ageing of dry snow ( $dr_{e,dry}$ ) is parameterized from the microphysical snow grain growth Snow, Ice, and Aerosol Radiative model (SNICAR) (*Flanner and Zender*, 2006). Since the complete SNICAR model is computationally too expensive, a parameterization is used that has temperature, temperature gradient and density of the specific snow layer as input. Wet snow metamorphism ( $dr_{e,wet}$ ) is based on *Brun et al.*

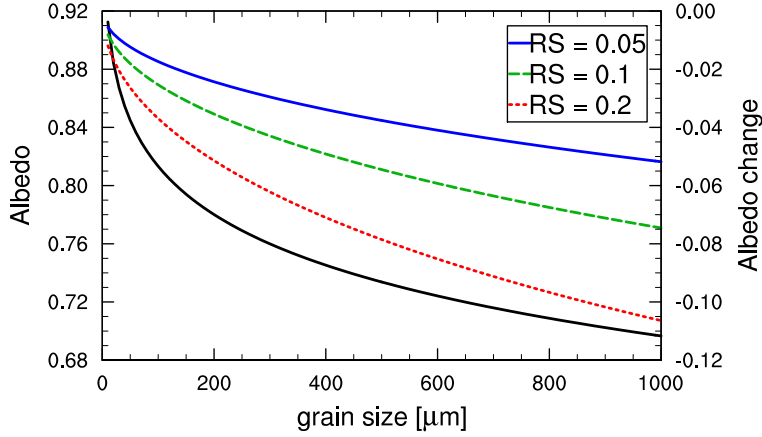


**Figure 4.4:** Snow albedo as function of grain size (black, left axis) and the change of albedo as function of grain size for three different concentrations of black carbon in the snowpack: 0.05 ppmv (blue, right axis), 0.1 ppmv (green) and 0.2 ppmv (red).

(1989), in which the growth of the snow grains is dependent on the amount of liquid water present in the snowpack.

Black carbon concentrations in Antarctic snow are very low (*Grenfell et al.*, 1994; *Warren and Clarke*, 1990), so a correction for black carbon was not applied by *Kuipers Munneke et al.* (2011). In contrast, black carbon concentrations of 0.05 ppmv have been measured at Summit (*Flanner et al.*, 2007), Greenland, and probably even higher concentrations are present in the lower regions. This will have a significant impact on snow albedo (*Flanner et al.*, 2007; *Hansen and Nazarenko*, 2004). The effect of black carbon on broadband snow albedo in RACMO2 follows Equation 8 in *Gardner and Sharp* (2010):

$$d\alpha_c = \max(0.04 - \alpha_s, \frac{-c^{0.55}}{0.16 + 0.6S^{0.5} + 1.8c^{0.6}S^{-0.25}}), \quad (4.3)$$

in which  $S$  is the specific surface area of the snow grains ( $\text{m}^2 \text{kg}^{-1}$ ) and  $c$  the carbon loading (ppmv).

The black line in Figure 4.4 shows broadband albedo for a range of snow grains between 20 and 1000  $\mu\text{m}$ , without correcting for black carbon, cloud cover or solar zenith angle. Fresh snow albedo is as high as 0.85, but drops rapidly with increasing snow grain size to a value of 0.7 for 1 mm grains (typical for wet snow). The colored lines show  $d\alpha_c$  for three different values of carbon loading: 0.05 ppmv (blue), 0.1

ppmv (green) and 0.2 ppmv (red). The effect of black carbon on albedo increases with increasing grain size. The reason is that photons are preferentially scattered forward by larger grains and thus have a longer pathway in snow with larger grain sizes, increasing the chances to meet a black carbon particle and being absorbed by it. For a snowpack consisting of grains with an average grain size of 1 mm, a carbon loading of 0.1 ppmv will decrease the albedo from 0.7 to 0.63, equivalent to an increase in the absorption of shortwave radiation of 20 %.

#### 4.2.5 MODIS background ice albedo

The albedo of bare ice in the ablation area of the GrIS is not constant in space and time (Box *et al.*, 2012b). In the southwestern region of the ice sheet, the so called dark band (Wientjes *et al.*, 2011) shows albedo values  $<0.4$ , while similarly strong spatial albedo variability is found in other parts of the GrIS (Boggild *et al.*, 2010). This motivated us to compile an ice albedo field that can serve as background ice albedo in RAMCO2.

Figure 4.1 shows the background ice albedo (BIA) field used in the CONTROL simulation. The BIA is used if the density of the top two layers of the snow model is equal to the density of ice ( $910 \text{ kg m}^{-3}$ ). The BIA is based on the moderate-resolution imaging spectroradiometer (MODIS) white sky albedo product (NASA Land Processes Distributed Active Archive Center (LP DAAC). Albedo 16-Day L3 Global 0.05Deg CMG. USGS/Earth Resources Observation and Science (EROS) Center, Sioux Falls, South Dakota, 2012). The satellite data are based on a 16 day integration period, with a time resolution of 8 days at a horizontal resolution of  $0.05^\circ$  ( $\sim 5 \text{ km}$ ). The MODIS albedo product has been evaluated by Stroeve *et al.* (2005); MODIS derived albedos are accurate for albedo values  $<0.7$  over Greenland and as such they are suitable for determining a background ice albedo field.

The BIA field is calculated using 10 years of MODIS data (2001-2010), taking the average of the lowest 5% of data at every grid point. A minimum value is set to 0.3, and a maximum to 0.55. The latter value is also used for locations which are snow covered throughout the year, but are expected to become snow free in the coming years. For grid points with missing MODIS data, a problem occurring only at high latitudes ( $> 80^\circ\text{N}$ ), the BIA is set to 0.47, being the average albedo of all the ice points. Note that this value is significantly lower than the ice albedo value of 0.52 used in the previous version of RACMO2 (Ettema *et al.*, 2010a).

Although ice albedos as observed by MODIS are reasonably stable from year to year, some inter-annual variability remains. For example, at the location of S6, the lowest MODIS-derived ice albedo values range between 0.34 and 0.44 in the

period 2004–2010. This variability is partly due to measuring uncertainties (mainly due to cloud cover), and partly a real phenomenon, possibly associated with delayed supraglacial runoff of meltwater (*Van den Broeke et al.*, 2008b).

#### 4.2.6 Model experiments

To tune and evaluate the new albedo parameterization, we have performed seven RACMO2 simulations for the year 2007. Performing these experiments is computationally expensive and time consuming, therefore a single year is chosen. The year 2007 is the record melt year in the last decade and thus the best resemblance for future warmer years with an increasing ablation area, and thus important to simulate correctly. Evaluation is done with the emphasis on melt extent and station S9, located close to the equilibrium line where the local SMB is very sensitive to small changes in the albedo scheme. Radiation measurements have been performed at several other locations on the GrIS (*Steffen and Box*, 2001), but most of these are located in the accumulation area at  $\sim 2000$  m where albedo variations are small.

Table 4.1 summarizes the different albedo experiments with RACMO2. The ANT settings are the settings used for the Antarctica integration (*Kuipers Munneke et al.*, 2011). With every new experiment one parameter is changed. In FSGRAIN the specific surface area of fresh snow is decreased from 80 to 60  $\text{m}^2 \text{kg}^{-1}$ , equivalent to an increase in effective radius of the grain size ( $r_{e,0}$ ) from 41 to 55  $\mu\text{m}$ . In the previous RACMO2 snow albedo scheme, the maximum amount of liquid water in the snowpack was limited to 2%. In the new snow albedo scheme, this artificial limit is no longer needed, and the amount of liquid water in the snowpack is calculated following *Coléou and Lesaffre* (1998). In their expression, the maximum amount of liquid water is related to the available pore space in the snowpack and can reach values of up to 13% of the weight of the snowpack (experiment LWMAX). Next, in RFGRAIN, the grain size of refrozen snow is increased from 1 to 2 mm, followed in ICEALB by a decrease of the ice albedo from 0.5 to 0.45. In RSOOT black carbon is added to the snowpack (0.1 ppmv), and in the final simulation (CONTROL) MODIS background ice albedos are used instead of a spatially constant value.

### 4.3 Results

#### 4.3.1 Albedo time series

Figure 4.5 displays time series of modeled and measured albedo at locations S6 (4.5a) and S9 (4.5b) for the year 2007. In winter the rough ice surface at S6 is snow covered,

4. Sensitivity of Greenland ice sheet surface mass balance to surface albedo parameterization: a study with a regional climate model

---

**Table 4.1:** Summary of the model settings applied in the different simulations with RACMO2.

Experiment	FS Grain $m^2 kg^{-1}$	RF grain $mm$	Max liquid water	Ice Albedo	Soot $ppmv$
ANT	80	1000	2%	0.5	-
FSGRAIN	60	1000	2%	0.5	-
LWMAX	60	1000	C&S <sup>1</sup>	0.5	-
RFGRAIN	60	2000	C&S	0.5	-
ICEALB	60	2000	C&S	0.45	-
RSOOT	60	2000	C&S	0.45	0.1
CONTROL	60	2000	C&S	MODIS <sup>2</sup>	0.1

<sup>1</sup>Maximum liquid water content based on Coléou and Lesaffre (1998)

<sup>2</sup>Background ice albedo based on MODIS retrievals

resulting in albedo values of 0.8-0.9 until the end of May. The thin (~40 cm) snow-cover at S6 disappears rapidly and at the beginning of June ice appears at the surface, the timing of this is well simulated in CONTROL. In ANT, melting the snowpack takes two weeks longer, due to a higher snow albedo in spring. In both ANT and CONTROL, the end of the melt season at the end of August is well timed. The background ice albedo in CONTROL is slightly too low compared to the observations (AWS and MODIS) for this specific year.

Results for S9 are displayed in Figure 4.5b. In this specific year, bare ice is exposed at the end of June, about two weeks later than at S6. In experiment CONTROL the onset of the melt season is again well timed. In ANT, the snow layer does not fully melt, which emphasizes the fact that close to the equilibrium line, small changes in the albedo can have a strong impact on the surface mass balance. At S9 the background albedo is 0.55, in good agreement with the weather station and the MODIS observations. Note that the snowfall events at the end of June and August are well represented in RACMO2.

Figure 4.6a compares albedo time series at S9 with MODIS and CONTROL for the period 2004-2009. Overall, RACMO2, the in situ measurements and MODIS observations are in good agreement. Averaged albedo over the months March to September is 0.774 (modeled) compared to 0.794 (measured at the AWS). This represents a large improvement compared to the simulation with the density dependent albedo scheme (0.721). In that scheme an artificial minimum snow albedo of 0.7 was imposed to prevent an unrealistic decrease in snow albedo during periods of strong snowmelt. This limit is no longer needed in the new parameterization.

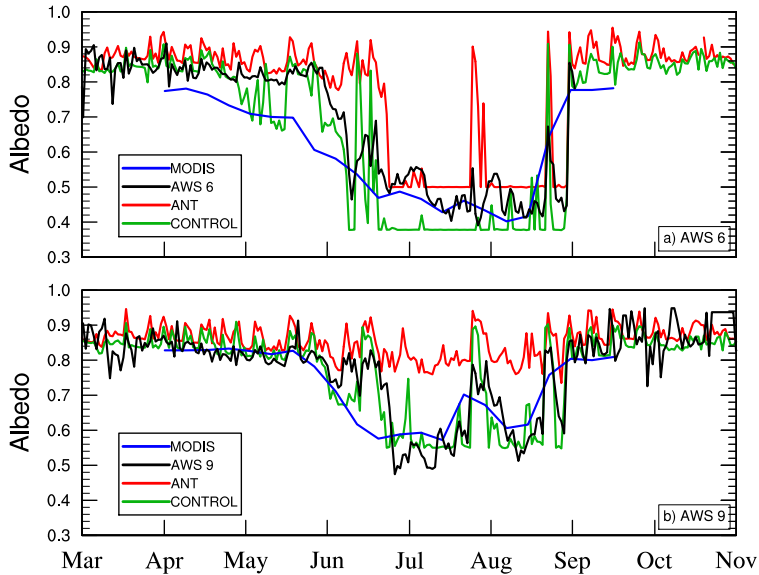


**Figure 4.5:** Albedo for the year 2007 at AWS 6 (top) and AWS 9 (bottom). Black line shows AWS measurements, red line shows RACMO2 albedo in the ANT experiment, green line shows RACMO2 albedo in the CONTROL experiment and blue line shows MODIS-derived albedo.

In most years, the MODIS inferred albedo shows a higher minimum albedo compared to both the AWS measurements and the RACMO2 results. MODIS uses a 16 day time span to calculate a single albedo value; the exposure of bare ice at S9 in a regular melt season is seldom continuous for a 16 day period, but interrupted by snowfall events. An exception is the year 2007, where MODIS albedo decreases to values close to 0.55.

Figure 4.6b depicts measured (red) and modeled (black) net shortwave radiation, Figure 4.6c shows the differences. The numbers in Figure 4.6c denote the mean bias and root-mean-square error (RMSE) for the individual years. Averaged over the 6 year period, modeled net shortwave radiation is  $3.0 \text{ W m}^{-2}$  or 6% larger than the measured values. This discrepancy can be ascribed mainly to the two years 2004 and 2005 where the albedos in spring (May) are underestimated. This result compares favorably to the offset in the simulation with the previous, density-dependent albedo scheme ( $11.4 \text{ W m}^{-2}$ ).

The RMSEs are on average  $24.0 \text{ W m}^{-2}$ , which, compared to the average mean

4. Sensitivity of Greenland ice sheet surface mass balance to surface albedo parameterization: a study with a regional climate model

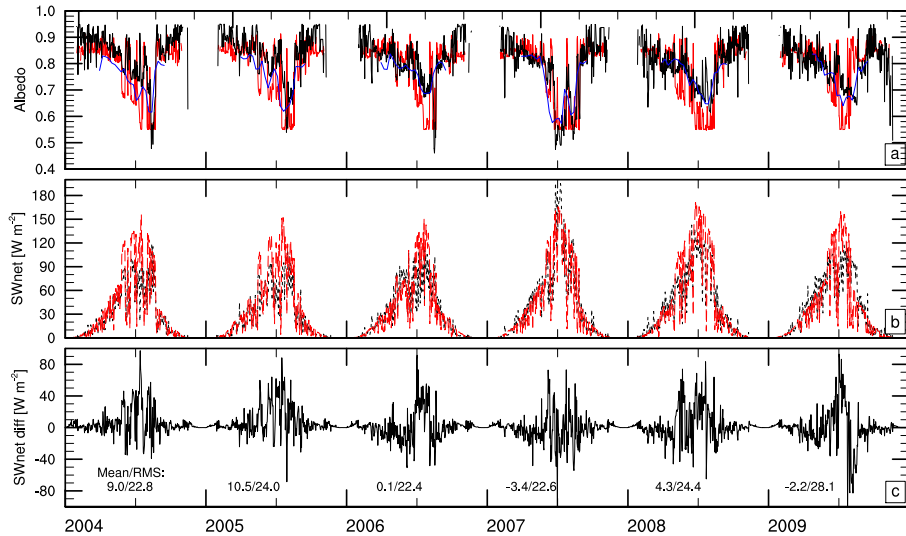


**Figure 4.6:** a) Albedo at location S9 for AWS data (red), MODIS observations (blue) and final (CONTROL) RACMO2 simulation (black). b) Net shortwave radiation at location S9 for AWS data (red) and RACMO2 (black). c) difference between RACMO2 and AWS in net short wave radiation. The numbers represent mean and root mean square difference (on a daily basis) for the individual years.

bias, is still significant. This remains a consequence of carrying out climate simulations, because the exact timing of snowfall events remains difficult. However, it is important to simulate the average net radiation correctly, such that the right amount of energy is available for melting and a correct estimate of snow melt is obtained.

### 4.3.2 SMB components

To assess the effect of the individual experiments on snow melt, the total number of melt days for the period according to SSM/I brightness temperatures is displayed in Figure 4.7a, and for the RACMO2 simulations in Figures 4.7b-h. Figure 4.8 shows the percentage increase of melt in a new simulation compared to the preceding simulation in Table 4.1. Table 4.2 lists SMB and its components for the seven simulations for calendar year 2007, integrated over the entire GrIS.

In all simulations, total precipitation is around 715 Gt of which  $50 \pm 3$  Gt (7%) falls as rain. The ANT run shows a total sublimation of 27 Gt and 340 Gt melt. 156 Gt



**Table 4.2:** SMB components for different model runs, year 2007. Relative changes in parentheses.

Experiment	Precip	Subl	Melt	Refreeze	Runoff	SMB	Melt area <sup>1</sup>
ANT	713	27	340	156	242	444	9.2%
FSGRAIN	710	30 (+11%)	374 (+10%)	167 (+7%)	265 (+10%)	415 (-7%)	10.1%
LWMAX	711	31 (+3%)	406 (+9%)	191 (+14%)	271 (+2%)	410 (-1%)	11.1%
RFGRAIN	712	32 (+3%)	480 (+18%)	217 (+14%)	318 (+17%)	362 (-12%)	13.0%
ICEALB	715	32 (+0%)	503 (+5%)	218 (+0%)	341 (+7%)	341 (-6%)	13.0%
RSOOT	719	41 (+28%)	742 (+48%)	295 (+35%)	501 (+47%)	177 (-48%)	17.7%
CONTROL	720	42 (+2%)	715 (-4%)	297 (+1%)	473 (-6%)	205 (+16%)	17.4%

<sup>1</sup>Averaged melt area for the period May to August 2007. SSMI data gives 17.3%

(40%) of the available liquid water refreezes in the snowpack, and 242 Gt runs off as meltwater, resulting in a positive surface mass balance of 444 Gt, two-thirds of the total mass gained by precipitation. For the year 2007, this value for total SMB is too high (*Van den Broeke et al.*, 2009). The lack of melt is reflected in the number of melt days for the period March to April 2007 compared to SSMI (Figure 4.7).

Increasing the snow grain size of fresh snow from 41 to 55  $\mu\text{m}$  ('FSGRAIN' simulation), results in an increase in melt to 374 Gt (+10%). The additional liquid water flux is equally divided between refreezing and runoff, resulting in a SMB decrease of 29 Gt (-7%). Figure 4.8a shows that a larger grain size for fresh snow results in  $\sim 30\%$  more melt in the accumulation area in south Greenland. An increase in grain size also results in an earlier start of the melt season and hence the earlier appearance of bare ice in the ablation region, leading to a  $\sim 10\%$  increase in melt in ablation areas.

Changing the maximum liquid water content in the snowpack, from 2% to a value determined by the scheme of *Coléou and Lesaffre* (1998) ('LWMAX' simulation in Table 4.2), hardly affects the total SMB, although individual SMB components show significant variations. The larger amount of liquid water allowed to be retained in the snowpack facilitates refreezing; this increases snow grain size, accompanied by a decrease in the albedo and resulting in  $\sim 9\%$  more snow melt, with locally an increase of up to 50% in the south (Figure 4.8b). Due to the larger retention capacity, a significant amount of liquid water is still present in the snowpack at the end of September ( $\sim 20$  Gt). So although the change in the snowpack physics does not alter the SMB directly, the extra snow melt and refreezing will cause the snowpack to warm and probably results in extra melt in the following year. The number of melt days also increases (Fig. 4.7d), but is still too small compared to the satellite data (Fig. 4.7a).

4. Sensitivity of Greenland ice sheet surface mass balance to surface albedo parameterization: a study with a regional climate model

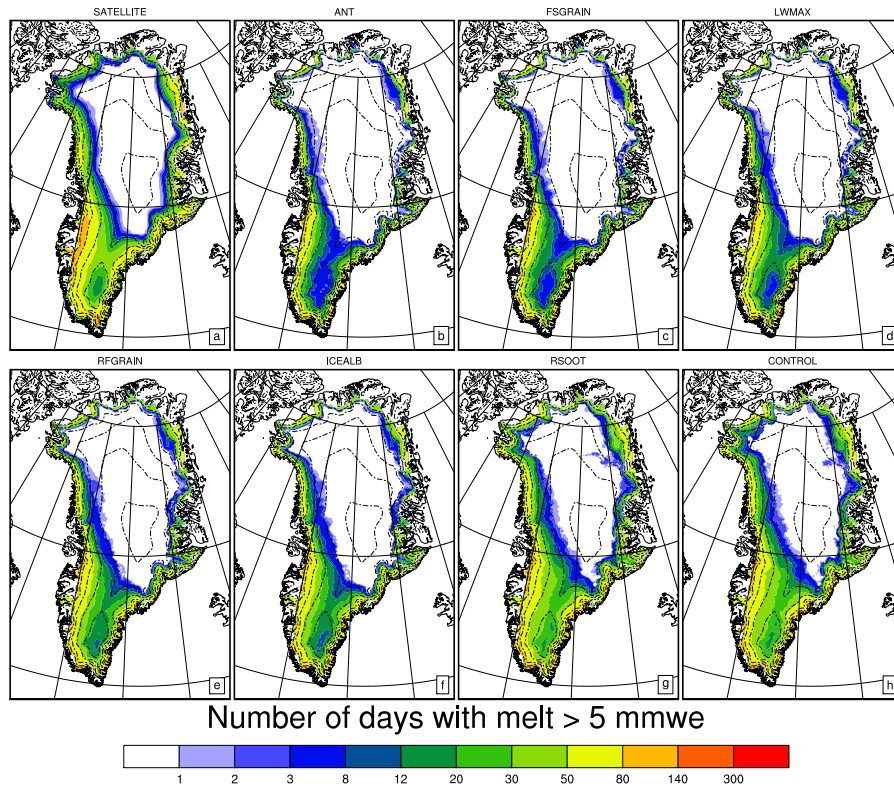


**Figure 4.7:** Number of days with melt according to SSM/I satellite data (a) and the number of days with more than 5 mm w.e. snowmelt in the different RACMO2 experiments (b-h). The individual simulations are listed in table 4.1 and explained in the text. The last column in table 4.2 lists the average melt area for the period May to August 2007.

Increasing the grain size of refrozen snow from 1 to 2 mm (RFRAIN) has a strong impact on the SMB (-48 Gt or -12%). Snowmelt increases by almost 20%, most of which runs off the ice sheet. In some areas the amount of snow melt more than doubles (Fig. 4.8c). It is interesting to note that changes in the refreezing parameters (LWMAX and RFRAIN) have most impact on melt in regions higher up the ice sheet and along the southeast coast, where precipitation rates are high, because in those regions the full refreezing capacity of the snowpack is not reached.

A decrease of the ice albedo from 0.5 to 0.45 ('ICEALB' simulation) is equivalent

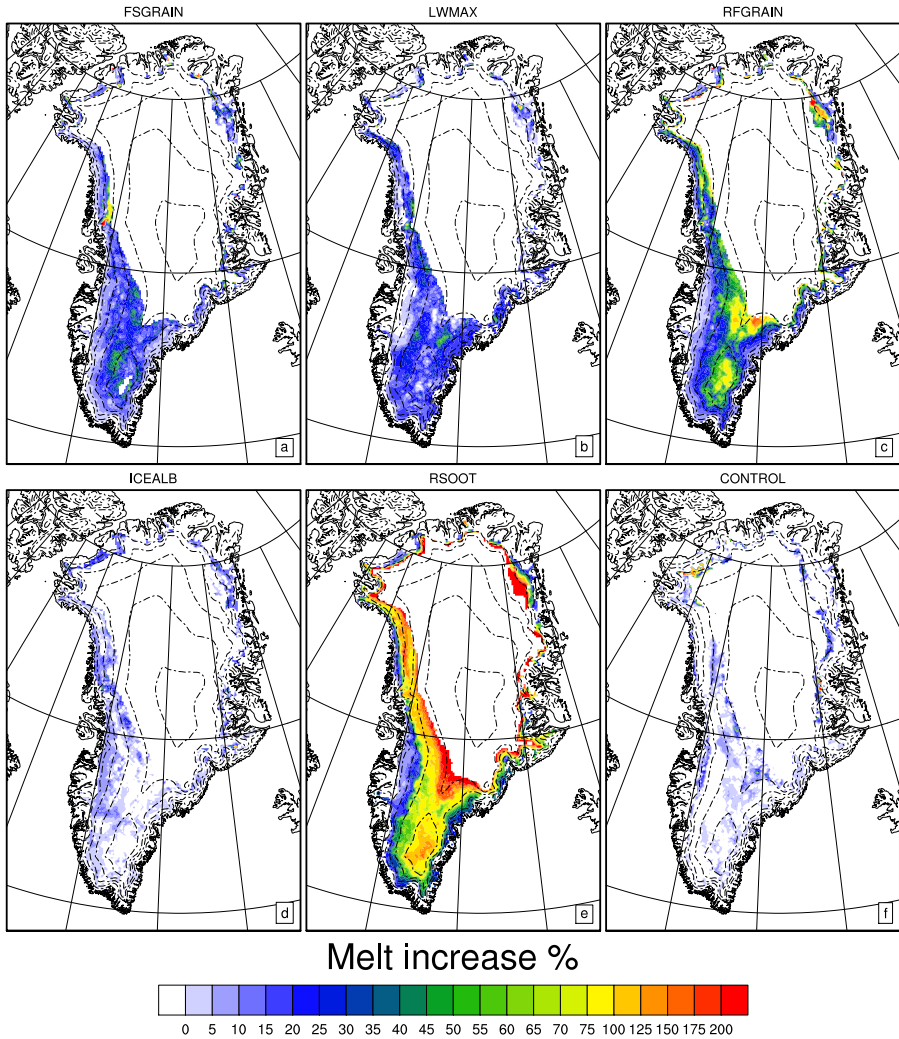


**Figure 4.8:** The relative increase in snowmelt energy compared to the preceding simulation in Table 4.1. Panel FSGRAIN (a) shows the increase in snowmelt compared to the ANT simulation. As threshold a minimum of 10 mm w.e. snow melt is used.

to an extra uptake of shortwave radiation by 10% if bare ice is present at the surface. This increases total melt by another 23 Gt or 5%. Since only areas are affected where bare ice is at the surface, runoff increases by the same amount. The 10% increase in melt (Fig. 4.8d) in regions with bare ice at the surface, equals the increase in net shortwave radiation, which is in agreement with *Van den Broeke et al. (2008a)*, who showed that temporal variability in melt in the western ablation region of the GrIS is mainly driven by variability in shortwave radiation. In the future it is expected that SMB sensitivity to the background ice albedo will increase, since on average a larger area of bare ice will be present at the surface for a longer period each year (*Fettweis et al., 2011*). The relatively small differences in the accumulation zone in Fig. 4.8d cancel out in the mean and are due to small changes in the snowfall pattern in the different simulations.

In RSOOT we added 0.1 ppmv of black carbon to the snowpack. The direct effect on albedo, as discussed in section 4.2.4, is displayed in Figure 4.4: the albedo of fresh snow is reduced by 0.02 and that of older snow by up to 0.07, equivalent to an extra uptake of shortwave radiation of 10% and 20% respectively. However, the increase in snowmelt is 48% (+239 Gt), indicating the importance of positive feedbacks. The increase in absorbed shortwave radiation heats the snowpack, resulting in larger snow grains, which in turn lowers the albedo and further enhances the absorption of shortwave radiation. The increase in runoff is larger than the increase in refrozen meltwater, owing to an earlier onset of melting as a result of which bare ice is exposed earlier in the season. The relative effect of black carbon on melt increases gradually with height (Figure 4.8e), from ~10% in the ablation region to over 200% in the higher accumulation regions. The number of melt days (Figure 4.7e) is now on average in good agreement with the satellite measurements (Table 4.2), although regional differences remain. This demonstrates that a nonzero soot concentration is required to obtain realistic snow albedos.

In the final simulation (CONTROL) the background ice albedo field is applied (see section 4.2.5). The total amount of melt is slightly reduced, because on average the BIA is 0.47, slightly higher than the value in the preceding simulation (0.45). However, since BIA varies between 0.3 and 0.55, regional changes are significant, e.g. a ~15% increase in melt in the dark band in the western ablation area (Figure 4.8f).

The experiments show that when varied within realistic parameter spaces, the albedo scheme introduces variations in total surface mass balance averaged over the GrIS between +177 and +444 Gt for the year 2007, equivalent to 25% and 62% of the total precipitation respectively. This underlines the strong sensitivity of Greenland SMB to surface albedo. It should be noted that the uncertainty in modeled Greenland

SMB is not equally large, because results of the CONTROL experiment are in much better agreement with in situ measurements and satellite observations compared to the other experiments. Furthermore it is difficult to assess the absolute value of SMB, because no direct measurements of meltwater runoff are available. Especially for future projections the changes in SMB components with respect to present day conditions will determine increases in sea level rise, therefore it is more important to simulate the inter-annual variability in SMB correctly than the absolute values (*Van den Broeke et al.*, 2009). Furthermore the inter-annual variability in SMB is more dependent on total accumulation and summer temperatures than on albedo (*Ettema et al.*, 2009).

### 4.3.3 SMB along the K-transect

Figure 4.9 compares the averaged observed surface mass balance along the K-transect for the period 1991 to 2010 with results of RACMO2 using the CONTROL settings. The observed SMB ranges from -4 m w.e. at an altitude of 500 m to +0.5 m w.e. at 2000 m. This gradient is well captured by RACMO2. Between 1000 and 1700 m elevation, the total SMB is still somewhat underestimated. This is probably not related to albedo, since the modeled albedo at station S9 (1500 m) is in good agreement to the observed albedo. *Ettema et al.* (2010a) demonstrated that the sensible heat flux is overestimated at S6 and S9. This problem is still present in the new RACMO2 simulation and presents a plausible explanation for the offset in SMB. As a result, the equilibrium line altitude in RACMO2 (around 1800 m in Figure 4.9) is simulated about 200 m too high.

Figure 4.10 shows strong spatial variability in SMB at a constant altitude. This is directly related to the background albedo field; the blue and green dots in Figure 4.10 can be easily linked to each other for the lower ablation region (<1200 m). As a first approximation, a decrease in background albedo of 0.07 is equivalent to a 0.5 m w.e. lower SMB. The use of a background ice albedo field thus improves the results in the lower ablation region.

## 4.4 Summary and Conclusions

We have used the regional atmospheric climate model RACMO2 to assess the sensitivity of the surface mass balance (SMB) of the GrIS to a new snow albedo parameterization. The snow albedo parameterization uses a prognostic snow grain size and introduces corrections for cloud cover, solar zenith angle and black carbon loading. We also applied a spatially variable background ice albedo field, based on 2000-2010 MODIS satellite retrievals. This affects especially regions with strong ice albedo

#### 4. Sensitivity of Greenland ice sheet surface mass balance to surface albedo parameterization: a study with a regional climate model

---

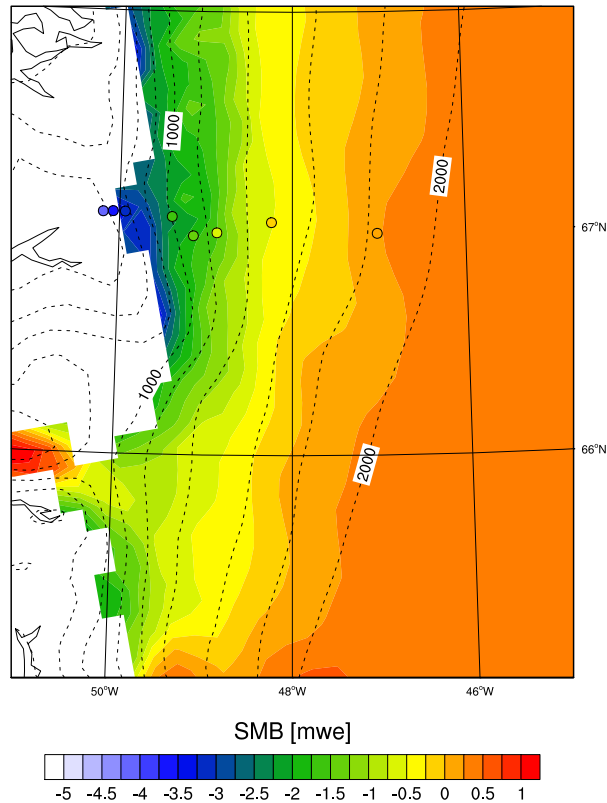


**Figure 4.9:** Average surface mass balance for the period 1991-2010 in the K-transect region. The dots represent stake measurements. Height contours every 200 m

variability, such as the dark band in the western ablation zone. In situ SMB observations and satellite derived melt duration have been used to evaluate RACMO2 including the new albedo scheme. With the new albedo parameterization, RACMO2 agrees better with albedo measurements at the K-transect in West Greenland. The steep SMB gradient in this region is now well represented compared to the previous, density-dependent albedo scheme.

A complicated and poorly understood process is the interaction between albedo and the refreezing and retention of meltwater. Although the direct effect of an increase in the maximum retention capacity of the snowpack on the SMB is small, the indirect effect could be significant, e.g. by warming the snowpack and further enhancement

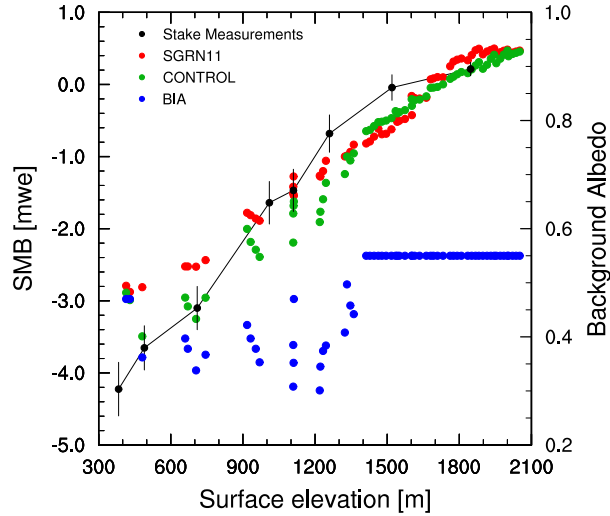


**Figure 4.10:** Observed SMB along the K-transect for the period 1991-2010 with standard deviation of annual values as error bars (black); RACMO2 simulated SMB as a function of height for grid points in the K-transect region for the previous (red, Ettema et al. (2009)) and new (green) albedo parameterization. Background ice albedo values (right axis) for the corresponding grid points are also shown (blue).

of melting. This process is particularly important in a non-steady warming climate, since it determines the capacity for refreezing of infiltrated meltwater within the firn column. To study this, a high-resolution climate scenario run will be carried out with RACMO2 for the GrIS. Using results from the present study, we expect to be able to provide a more detailed projection of Greenland mass loss and associated sea level rise with a better constrained uncertainty.

5





# Contemporary (1960-2012) evolution of the climate and surface mass balance of the Greenland ice sheet

---

We assess the contemporary (1960-2012) surface mass balance (SMB) of the Greenland ice sheet (GrIS), its individual components and trends. We use output of the high-resolution (11 km) regional atmospheric climate model (RACMO2), evaluated with automatic weather stations and GRACE data. A persistent negative North Atlantic Oscillation (NAO) index over the last six years resulted in the summertime advection of relatively warm continental air towards the GrIS. Added to the enhanced radiative forcing by increased CO<sub>2</sub> levels, this has resulted in an increase of near surface temperature of more than 2 K during 2007-2012 compared to 1960-90. The associated decrease in albedo led to an extra absorption of shortwave radiation of  $\sim 6 \text{ Wm}^{-2}$  (11%) in the summer months (JJA), which is the main driver of enhanced surface melting and runoff in recent years.

From 1990 onwards, we see a steady increase in meltwater runoff and an associated decrease of the SMB, accelerating after 2005, with the record low SMB year in 2010. Despite the fact that the GrIS was subject to the highest surface melt rates in 2012, relatively high accumulation rates prevented 2012 to set a record low SMB. In 2012, melt occurred relatively high on the ice sheet where meltwater refreezes in the porous firn layer. Up to 2005, increased runoff was partly offset by increased accumulation rates. Since then, accumulation rates have decreased, resulting in low SMB values. Other causes of decreased SMB are the loss of firn pore space, and decreasing refreezing rates in the higher ablation area. The GrIS has lost in total  $1800 \pm 300 \text{ Gt}$  of mass from surface processes alone since 1990 and about half of that in the last 6 years.

## 5.1 Introduction

Warming in the Arctic region over recent decades has been almost twice as strong as the global average (*Bekryaev et al.*, 2010; *Johannessen et al.*, 2004). This phenomenon, known as polar amplification, is driven by a shrinking snow and sea-ice cover and the associated melt-albedo feedback (*Flanner et al.*, 2011; *Screen and Simmonds*, 2010). At a regional scale, also ocean (*Chylek et al.*, 2009; *Mahajan et al.*, 2011) and atmospheric circulation (*Graversen et al.*, 2008) and cloud water content (*Francis and Hunter*, 2007) are suggested to contribute to the excessive warming at higher latitudes. The warming resulted in record minima september sea-ice extent in 2002, 2005, 2007 and again in 2012 (*Comiso*, 2012; *Stroeve et al.*, 2007, 2012).

A key player in the Arctic climate system is the Greenland ice sheet (GrIS). With an altitude up to 3200 m and located just north of the Atlantic storm track (Figure 5.1), it has a strong influence on the atmospheric circulation (*Petersen et al.*, 2004; *Van Angelen et al.*, 2011a) and meridional sea-ice transport (*Van Angelen et al.*, 2011b). The GrIS has the potential to raise global sea level by  $\sim 7$  m (*Bamber et al.*, 2001). The recent warming has resulted in accelerated mass loss from the GrIS (*Rignot et al.*, 2011; *Shepherd et al.*, 2012; *Van den Broeke et al.*, 2009), increased surface melting (*Fettweis et al.*, 2011; *Tedesco et al.*, 2011), a decreasing albedo (*Box et al.*, 2012a) and the acceleration of outlet glaciers (*Moon et al.*, 2012; *Nick et al.*, 2009). The exceptionally warm year 2012 saw strong and extended melt over the GrIS (*Tedesco et al.*, 2013). On the 12th of July, almost the entire ice sheet was subject to surface melting (*Nghiem et al.*, 2012). Through meltwater runoff to the base of the ice sheet and further into the ocean, rapid surface changes that take place on time scales of only several summer seasons may provoke changes ice dynamics and ocean circulation that have decadal to centennial horizons.

To understand the physical processes governing the interaction between atmospheric circulation, surface energy balance and surface mass balance, a high resolution regional atmospheric climate model coupled to a multi layer snow module can be a useful tool (*Cassano et al.*, 2001; *Ettema et al.*, 2009; *Fettweis et al.*, 2008). Here we use output of the Regional Atmospheric Climate Model (RACMO2) evaluated by automatic weather station (AWS) data and GRACE satellite retrievals (section 3) to assess and quantify the recent warming over Greenland (section 4). We discuss the implications for the surface energy balance (section 5) and surface mass balance of the ice sheet (section 6). The next section briefly describes RACMO2 and AWS-data as used in this study.

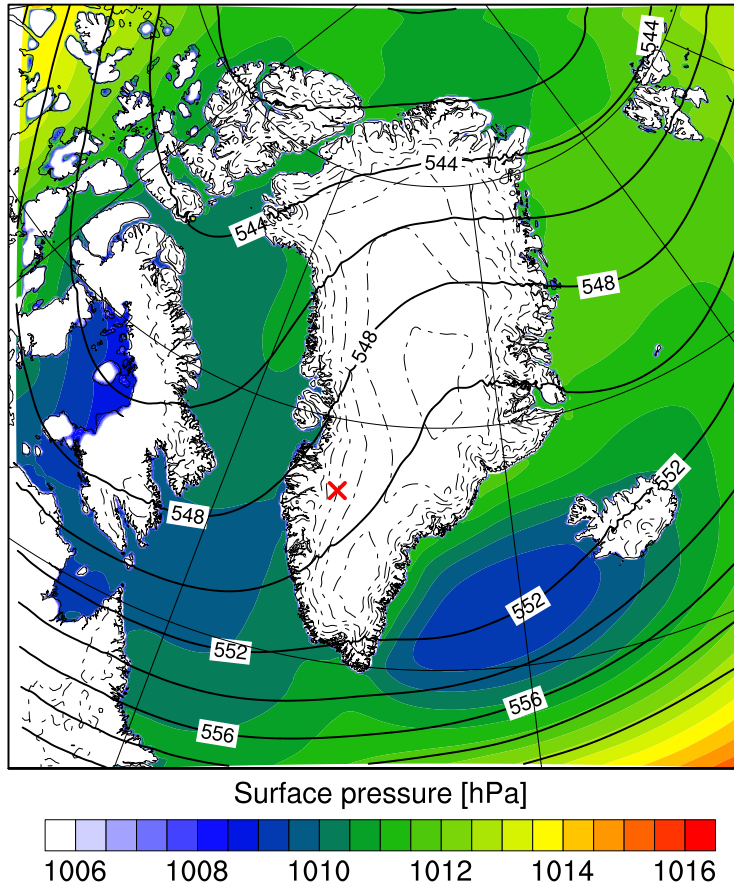


**Figure 5.1:** JJA surface pressure averaged over 1960-1990 (colors) and 500 hPa geopotential height (contours)

## 5.2 Data

### 5.2.1 Regional Atmospheric Climate Model (RACMO2)

For this study we use output of the regional atmospheric climate model RACMO2 for the period 1960-2012. RACMO2 was originally developed at the Royal Netherlands Meteorological Institute (KNMI) (Van Meijgaard *et al.*, 2008), based on the

physics package cycle 23r4 from ECMWF (White, 2004), which is implemented in the numerical weather prediction model HIRLAM 5.0.6 (Unden *et al.*, 2002). For a better representation of polar climates and a realistic description of processes that occur at glacier surfaces, RACMO2 is two-way coupled to a 100-layer snow model (Ettema *et al.*, 2010a). Recently RACMO2 is upgraded with a drifting snow scheme (Lenaerts *et al.*, 2012a) and a grain size dependent albedo scheme (Kuipers Munneke *et al.*, 2011; Van Angelen *et al.*, 2012). The latter is implemented for a better representation of changing surface snow characteristics in a warming climate.

The RACMO2 simulation used in this study is forced at the lateral boundaries by atmospheric profiles from a combination of ERA-40 (1960-1989, Uppala *et al.* (2005)) and ERA-Interim reanalysis data (1989 onwards, Simmons *et al.* (2007)). Sea surface temperature and sea ice concentration are also prescribed using the reanalysis data. The horizontal resolution is 11 km and RACMO2 has 40 sigma levels in the vertical. A ~260 km (24 grid points) relaxation zone is applied at the boundaries to convert the forcing fields to the RACMO2 grid; in the interior the model evolves freely. The full model domain covers Greenland, Iceland, Svalbard and the major ice sheets of the Canadian Arctic (Lenaerts *et al.* (2013), Figure 5.1).

Over the GrIS, RACMO2 has been extensively evaluated for temperature and wind (Ettema *et al.*, 2010a), albedo and melt extent (Fettweis *et al.*, 2011; Van Angelen *et al.*, 2012) and surface mass balance (Ettema *et al.*, 2009; Van den Broeke *et al.*, 2009). Here, in addition, we use de-trended GRACE mass retrievals to evaluate the seasonal cycle in modeled GrIS surface mass fluxes (next section).

## 5.2.2 Automatic Weather Station

Since 1990 the Institute for Marine and Atmospheric research Utrecht (IMAU) has performed stake surface mass balance measurements along a transect in the western ablation area of the GrIS near Kangerlussuaq at ~67°N (the K-transect, Van de Wal *et al.* (2012)). In 2003 three automatic weather stations (AWS) were set up along the transect (Van den Broeke *et al.*, 2008a) at approximately 5, 40 and 80 km from the ice sheet margin at altitudes of ~400, ~1000 and ~1500 m a.s.l. respectively. Here, we only use data from the highest AWS (S9), which experienced a shift from accumulation to ablation area in recent years.

## 5.2.3 GRACE

Observations of the time-variable part of the Earth's gravity field are being made by the Gravity Recovery and Climate Experiment (GRACE) since mid-2002. From these

observations, changes in the distribution of water masses at the Earth's surface can be deduced (Wahr *et al.*, 2004). In this study, we use the reprocessed Release 05 GRACE data from the Center for Space Research, available as spherical harmonics geoid coefficients up to degree and order 60 at a quasi-monthly frequency for 2003-2012. Due to the nature of the GRACE satellites orbit, the degree 1 coefficients are missing in these solutions and are taken from Swenson *et al.* (2008). The  $C_{20}$  coefficients, which are poorly observed by the GRACE satellites, are replaced by values from satellite laser ranging (Cheng and Tapley, 2004). To reduce noise in the GRACE data, we apply a Gaussian smoother with a halfwidth radius of 250 km. To retrieve the mass variations of the Greenland Ice Sheet from these data, the approach of Wouters *et al.* (2008) is used. This method minimizes the differences between mass anomalies in a model consisting of eight GrIS basins, each subdivided in a region below and above 2000 m, and the GRACE observations in an iterative way. After the final iteration, the total mass anomaly is then obtained by summing all GrIS basins. To remove potential biases from nearby areas, mass changes are simultaneously estimated in neighboring regions (e.g., the Canadian Arctic, Iceland, Svalbard). Tests with synthetic pseudo-observations show that the model retrieves the mass changes of the GrIS as a whole within a few Gt (Wouters, 2010)

### 5.3 Model evaluation using GRACE

Data of the Gravity Recovery and Climate Experiment (GRACE, Tapley *et al.* (2004)) have been used extensively to quantify the rate of mass loss from the Greenland ice sheet (Sasgen *et al.*, 2012; Schrama *et al.*, 2011). Here, we use de-trended time series of GrIS mass derived from monthly spherical harmonics as described in Wouters *et al.* (2008) to assess the seasonal cycle of mass on the GrIS as simulated by RACMO2 for the years 2003-2012. Figure 5.2a compares GRACE to data from ice sheet grid points in RACMO2, representing a total area of 1.71 million km<sup>2</sup>. The mass seen by GRACE is higher in spring and summer compared to RACMO2, indicative of a larger mass amplitude, i.e. more snow accumulation in winter and more meltwater runoff in summer. GRACE not only retrieves a mass signal from the ice sheet, but also from the accumulation and melting of seasonal snow on the surrounding tundra (an area of 0.45 million km<sup>2</sup>); including tundra processes, the agreement between RACMO2 and GRACE improves in spring (Figure 5.2b), but a bias remains in summer. This is most likely caused by the immediate runoff of meltwater in RACMO2 when it reaches the firn-ice horizon. In reality it takes considerable time for the meltwater to reach the ocean via the hydrological system of the ice sheet (supraglacial channels

## 5. Contemporary (1960-2012) evolution of the climate and surface mass balance of the Greenland ice sheet

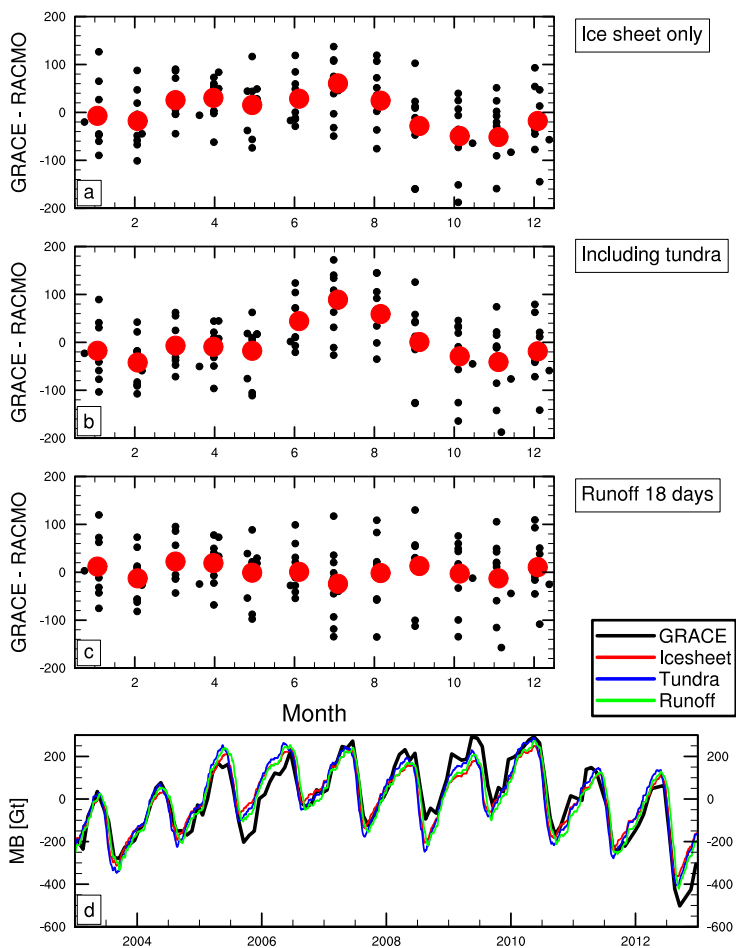


**Figure 5.2:** a-c: Monthly GrIS mass difference [Gt] (2003-2012) between RACMO2 and GRACE based on de-trended data for three different RACMO2 data sets. Red dots represent 10-yr mean. d: Time series of RACMO2 and GRACE mass estimates for 2003-2012.

and lakes, moulins and crevasses and subglacial channels) and crossing the tundra via meltwater rivers (Bartholomew *et al.*, 2011; Catania and Neumann, 2010). GRACE retrieves a mass signal from this liquid water as long as it is on land. If we delay the runoff in RACMO2 by 18 days we obtain the optimal correlation between GRACE

and RACMO2 ( $R^2 = 0.87$ ). This delay can be interpreted as a first order estimate of the meltwater residence time, i.e. the time it takes for glacial meltwater to reach the surrounding ocean. We also tested this method for smaller sized basins, but found that the noise in the GRACE retrievals became too strong, preventing convergence in some cases.

## 5.4 Atmospheric circulation and GrIS temperature

The 500 hPa height contours show a southwesterly flow over the GrIS in summertime (JJA) for the 1960-1990 reference period (Figure 5.1). At this level, a pressure ridge is present over the ice sheet interior as a result of the vertical compression of air flowing over a topographical barrier, leading to a south-southwesterly flow along the west coast, turning clockwise to a westerly flow over the northern half of the ice sheet. At the surface, the pressure field is characterized by the Icelandic Low and a strong pressure gradient along the south-east coast (*Van Angelen et al.*, 2011a). Another notable feature is the northerly flow over eastern Canadian Arctic.

During 1990-2006, the simulated upper air flow shows a similar pattern as for 1960-1990 and temperature anomalies at 500 hPa are limited to 1 K (Figure 5.3a). The near-surface temperature anomalies for 1991-2006 with respect to the 30 year reference period were also small (Figure 5.3d).

During 2007-2011 however, there was a clear shift in the dominant circulation pattern (*Overland et al.*, 2012). We find a weaker pressure gradient between the north and south of Greenland, due to relatively high pressure at the location of the climatological low pressure system near Iceland. As a result of the weaker pressure gradient, the strong west-east flow is easily disturbed resulting in a more meandering flow (Figure 5.3b), and advection of relatively warm air from continental Canada towards Greenland. At 500 hPa this results in a positive temperature anomaly along the east coast of Ellesmere and Baffin Islands of almost 3 K. The warm air is advected over the GrIS, resulting in positive near-surface temperature anomalies in excess of 2 K over almost the entire ice sheet (Figure 5.3e). This circulation pattern with warm air advection is even more pronounced in 2012 (Figures 5.3c and 5.3f), with southwesterly large scale flow and temperatures up to 4 K above the 1960-1990 climatological mean, both at the GrIS surface and at the 500 hPa level, with a maximum over Davis Strait.

To classify the circulation over the North Atlantic (including southern Greenland), the North-Atlantic Oscillation index is used. This index represents the pressure difference between and hence location of the climatological high pressure system near

5. Contemporary (1960-2012) evolution of the climate and surface mass balance of the Greenland ice sheet

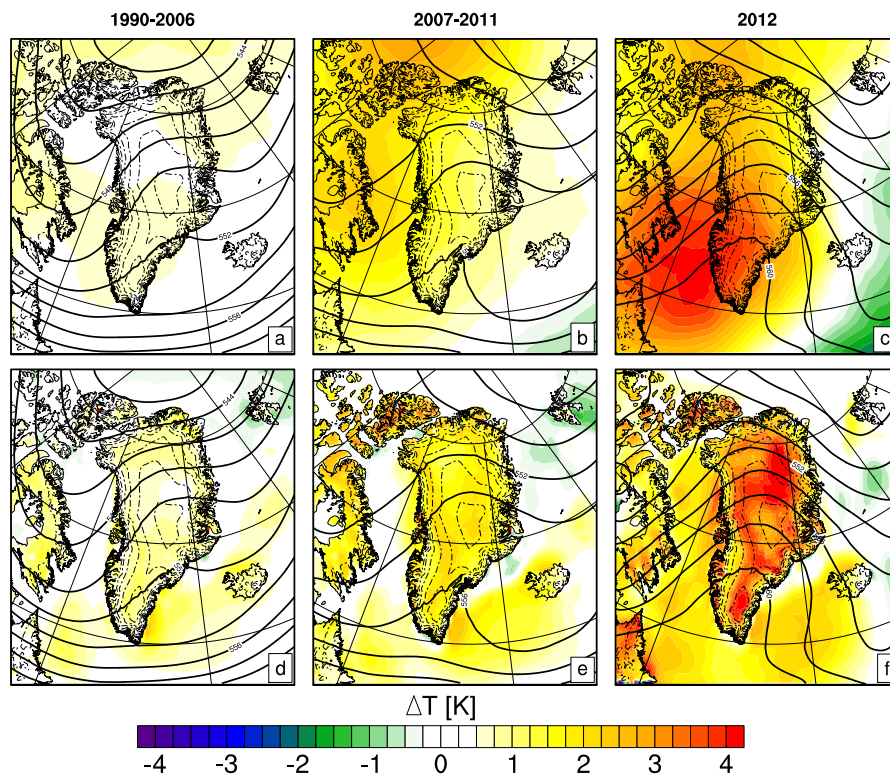


**Figure 5.3:** 500 hPa geopotential height (contours) and temperature anomalies at the 500 hPa level (a-c) and at 2 m (d-f), compared to the 1960-1990 reference period for 1990-2006 (left), 2007-2011 (middle) and 2012 (right)

the Azores and the low pressure system near Iceland (*Hurrell et al.*, 2003). Figure 5.4 shows averaged NAO-indices for the summer months back to 1960. A positive NAO-index implies stronger than normal zonally oriented (westerly) flow over the Atlantic Ocean south of Iceland, but also northwesterly flow over Arctic Canada. Following several decades during which the NAO-index switched between positive and negative values, over the last 6 years the summertime NAO-index has been persistently negative. Figure 5.4b and c shows the correlation between the NAO-index and 500 hPa height and temperature respectively. A strong negative correlation to the west of Greenland indicates high temperatures for that region during a negative NAO phase, caused by replacing the northwesterly by southwesterly flow, resulting in the earlier



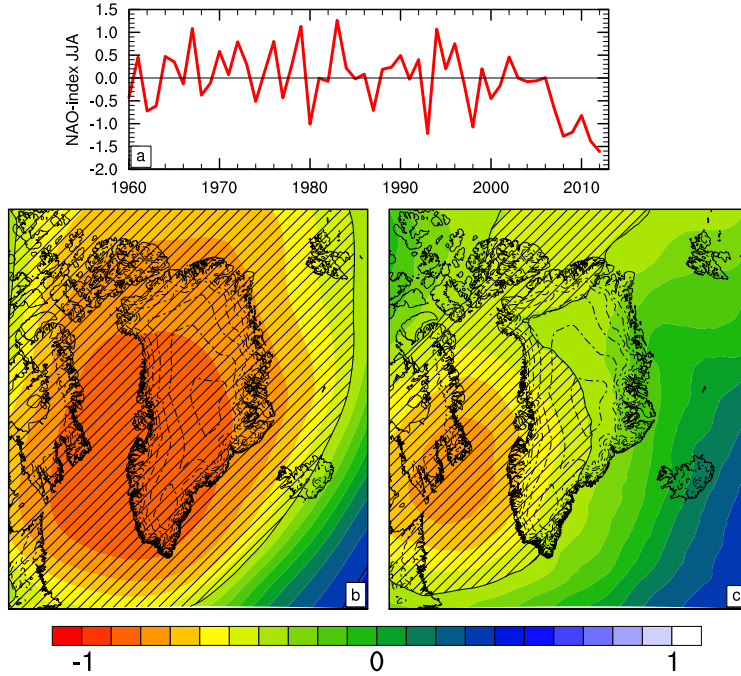


**Figure 5.4:** a) Averaged JJA index for the North-Atlantic Oscillation (data from NOAA). Correlation fields between the JJA NAO-index and the 500 hPa geopotential height (b) and temperature (c) from RACMO2 for 1960-2012; hatched area indicates the 99% confidence level.

described advection of relatively warmer air from southern latitudes to the GrIS, in turn leading to anomalously high surface temperatures (Fettweis *et al.*, 2012b).

This recent strong warming over the western part of the GrIS is also present in temperature data from the AWS at S9 at the K-transect. Figure 5.5 displays  $T_{2m}$  from 2004 to 2012 for the months May to September. 2012 and 2010 are the warmest years, with averaged JJA  $T_{2m}$  slightly above zero (Table 5.1). It is interesting to note that the positive temperature anomaly for 2012 is mainly caused by a warm June and July, whereas 2010 is characterized by anomalously high temperatures in May and in August, at the end of the melt season.

RACMO2 output (Figure 5.5b and Table 5.1: "R S9") puts the recent warming at S9 in a longer term perspective. RACMO2 is in good agreement with the AWS data for the years 2007-2012. The last decade of the 20th century shows the first

5. Contemporary (1960-2012) evolution of the climate and surface mass balance of the Greenland ice sheet

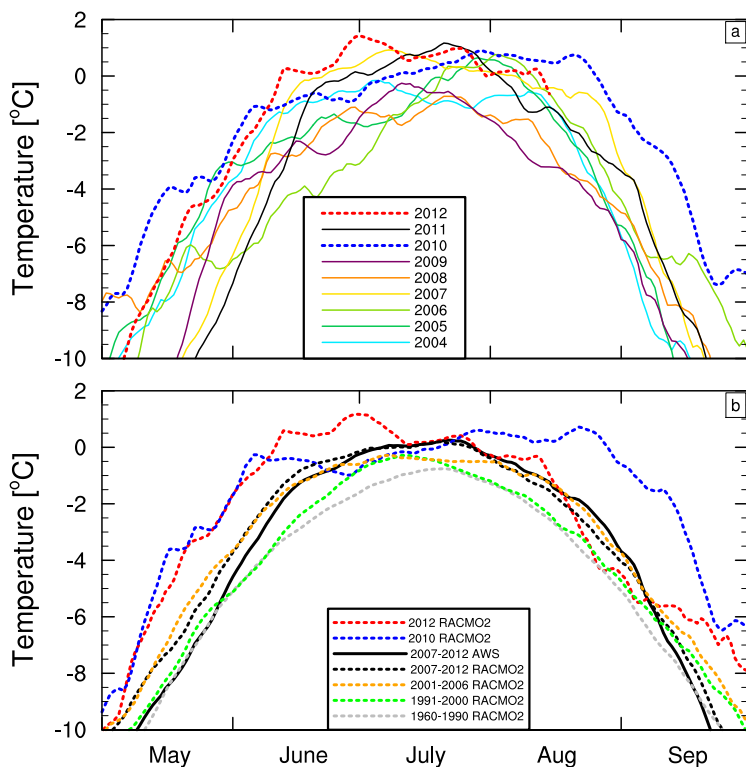


**Figure 5.5:** Measured (a)  $T_{2m}$  at AWS S9 for the years 2004-2012. Modeled (b)  $T_{2m}$  at location S9 for different time periods and the individual years 2010 and 2012. A 31 days running average is applied.

signals of warming of 0.3 K, mainly in June and July. This warming accelerates at the beginning of the 21st century (1.1 K for the years 2001-2006), increasing to up to 2.1 K for both the individual years 2010 and 2012 respectively. Averaged over the GrIS, the JJA  $T_{2m}$  increase over the last two decades is even stronger than at location S9 (Table 5.1). The reason is that the surface temperature in the ablation area, where S9 is located, is limited to the melting point, which limits the variability at 2 m. This effect is clearly visible in Figure 5.3. The recent warming over Greenland can not be explained by natural variability alone, because the 2012 summer temperature anomaly was 4.7 sigma with reference to the 1961-1990 mean.

**Table 5.1:** 2m-temperature, albedo and net shortwave radiation averaged over the months June, July and August for different time periods measured (S9) and modeled (R S9) along the K-transect and averaged over the entire ice sheet

Time	$T_{2m}$ [°C]			Albedo			$SW_{net}$ [ $Wm^{-2}$ ]		
	S9	R S9	GrIS	S9	R S9	GrIS	S9	R S9	GrIS
1960-1990	-	-2.16	-7.78	GrIS	0.71	0.793	-	81.0	58.5
1991-2000	-	-1.86	-7.40	GrIS	0.70	0.789	-	80.5	58.9
2001-2006	-	-1.03	-6.34	GrIS	0.68	0.780	-	87.0	61.4
2007-2012	-0.84	-0.83	-6.07	0.66	0.66	0.767	101.5	92.0	64.9
2010	0.0	-0.08	-5.28	0.60	0.62	0.767	119.4	100.2	64.7
2012	0.13	-0.05	-4.71	0.59	0.63	0.747	115.4	96.7	68.8

## 5.5 Surface Energy Balance

High snow temperature and melt accelerate snow grain growth, lowering the snow albedo and enhancing absorption of solar radiation (Box *et al.*, 2012a; Kuipers Munneke *et al.*, 2011; Tedesco *et al.*, 2013). This results in a more rapid removal of the winter snow layer in the ablation zone, and an early exposure of bare ice. At S9, both modeled and measured JJA-average albedo for the years 2007-2012 are 0.66 (Table 5.1), with record low values of 0.60 and 0.59 for the years 2010 and 2012 respectively. Figure 5.6 shows that episodically bare ice (albedo  $<0.5$ ) is present at the surface of S9 in 2010 and 2012, indicating that this location, at 1500 m, is gradually changing from accumulation to ablation area. In line with the  $T_{2m}$  anomalies (Figure 5.5), the melt season starts early in 2012 (halfway June), whereas 2010 is characterized by an extension of the melt season well into September. The lowering of summer albedo occurs ice sheet wide (Box *et al.*, 2012a), but is most pronounced in the ablation zone (Figure 5.7a). This reflects the increase in duration of bare ice exposure at the surface, which is significantly darker than (wet) snow. The sharp boundary in Figure 5.7a over the northern and western ice sheet reflects the location of the equilibrium line; above this altitude, the surface is continuously snow covered and absolute changes in albedo are weaker. The albedo decrease in southeast Greenland is limited for the same reason; abundant snowfall keeps the ice sheet snow covered throughout the melt season, even at lower elevations, resulting in a very narrow ablation zone ( $< 1$  grid point).

To quantify the impact of a decreasing albedo on the surface energy balance and melt, Figure 5.7b shows the absolute change in absorbed solar radiation ( $SW_{net}$ ) for the summer months of 2007-2012 with respect to 1960-1990. The increase in  $SW_{net}$  ( $> 20 Wm^{-2}$ ) is largest in regions with the strongest drop in albedo, i.e. the northern and western ablation areas. Averaged over the GrIS,  $SW_{net}$  increases

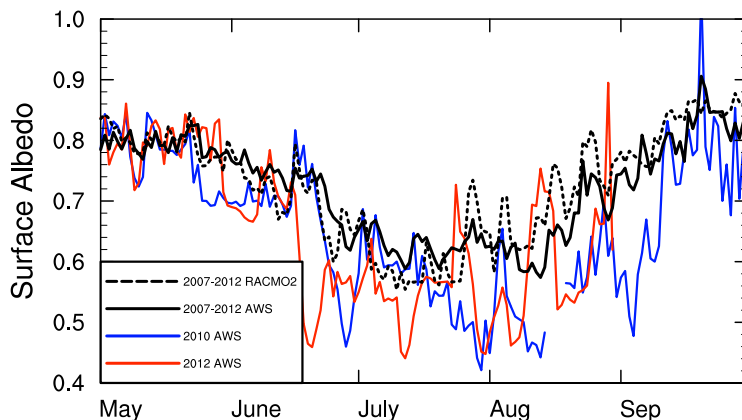


**Figure 5.6:** Modeled and measured albedo at station S9 averaged for 2007-2012 (black) and measured albedo for the years 2010 (blue) and 2012 (red).

from  $58.5$  to  $63.8 \text{ Wm}^{-2}$  (+9%, Table 5.1). At S9 the modeled increase in  $SW_{net}$  is  $11 \text{ Wm}^{-2}$  (+14%), with record values in 2010 and 2012 of  $+19 \text{ Wm}^{-2}$  and  $+16 \text{ Wm}^{-2}$ , respectively.

Figure 5.8 shows that the change in  $SW_{net}$  dominates over the other SEB components, stressing that the albedo-melt feedback is the most important driver of melt variability on the GrIS. The negative anomaly over the central area is due to an increase in simulated cloud cover, which is also reflected in the longwave radiation balance (Fig. 5.8b) that shows a positive change for the same region. The negative change in  $LW_{net}$  over the northwestern ice sheet indicates a decreased cloud optical thickness; this explains why the increase in  $SW_{net}$  is strongest over the northern ablation area. The sensible heat flux ( $SHF$ ) increased over the ablation areas by  $> 6 \text{ Wm}^{-2}$ : because the temperature of the melting ice surface remained constant, the increase of near surface air temperatures resulted in a larger temperature difference between the surface and the air above, and thus a larger transport of sensible heat towards the surface. The increase in cloud cover over the central ice sheet makes the radiative cooling of the surface less effective, which decreases the surface-to-air temperature difference, decreasing sensible heat transport towards the surface. The positive anomaly in the latent heat flux ( $LHF$ , Fig. 5.8d) over the western ablation area is also caused by the fixed surface temperature, resulting in less efficient evaporation/enhanced condensation over a melting surface. As long as the surface is not melting, the sublimation process will be more efficient for warmer conditions, leading

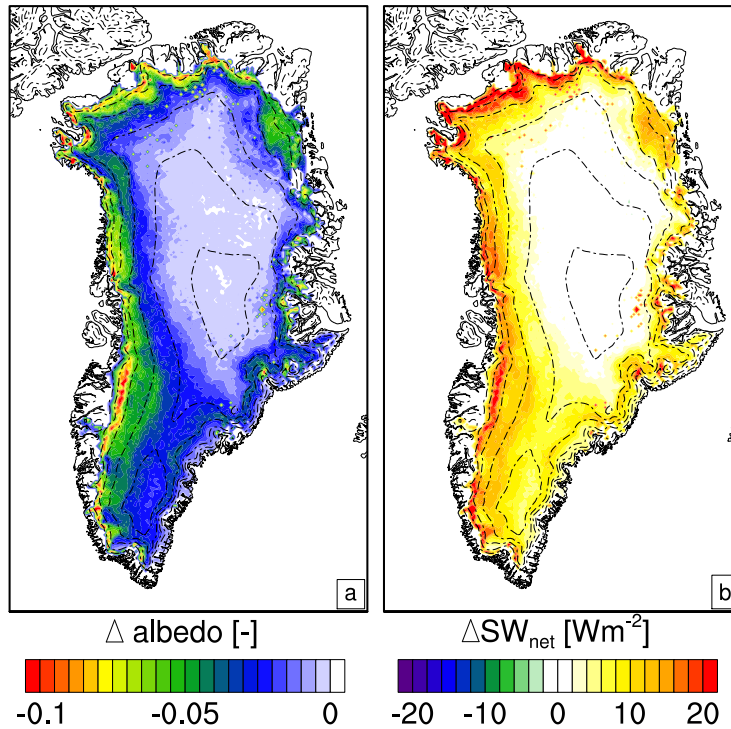


**Figure 5.7:** Difference fields between the summer months of 2007-2012 and 1960-1990 for albedo (a) and  $SW_{net}$  (b).

to a more negative  $LHF$  higher up the ice sheet.

To summarize, the surface of the GrIS has absorbed  $5.8 \text{ Wm}^{-2}$  more radiation in the summer months averaged over 2007-2012 compared to 1960-1990. The increase of  $SW_{net}$  ( $+5.5 \text{ Wm}^{-2}$ ) is clearly the dominant forcing, followed by  $LW_{net}$  ( $+0.5 \text{ Wm}^{-2}$ ) and  $SHF$  ( $+0.1 \text{ Wm}^{-2}$ ).  $LHF$  has a small cooling effect ( $-0.4 \text{ Wm}^{-2}$ ).

## 5.6 Surface mass balance

### 5.6.1 Melt duration

The extra flow of energy to the surface increases melting in terms of duration, intensity and extent. For the 1960-1990 reference period, no significant melt (more than

5. Contemporary (1960-2012) evolution of the climate and surface mass balance of the Greenland ice sheet

---

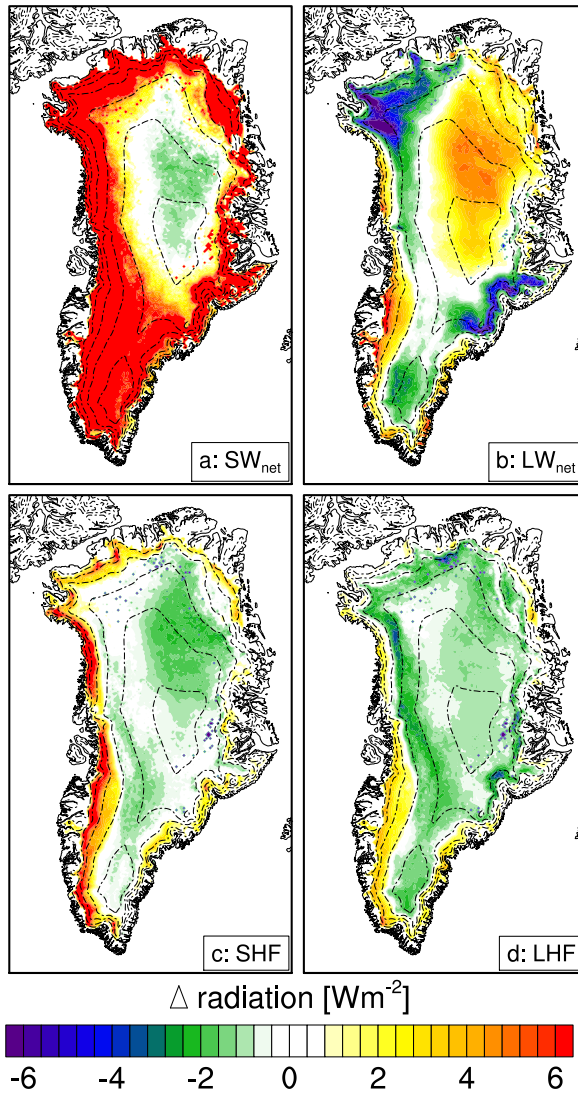


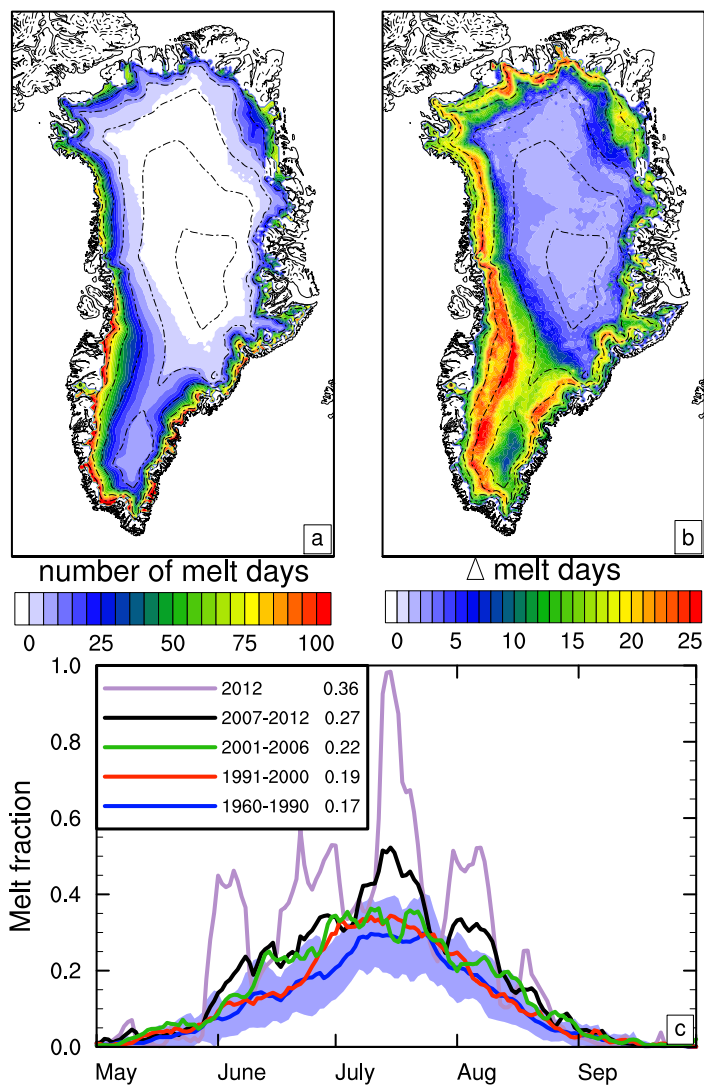
**Figure 5.8:** Difference fields between the summer months of 2007-2012 and 1960-1990 for  $SW_{net}$  (a),  $LW_{net}$  (b),  $SHF$  (c) and  $LHF$  (d). All fluxes are defined positive when directed towards the surface.

5 mm w.e. per day) is simulated by RACMO2 for a large area over the northern half of the GrIS (Fig. 5.9a). At South Dome, ~5 days experience melt, gradually increasing to more than 100 melt days along the western and southeastern ablation areas. This picture dramatically changes for the last 6 years of the simulation (Fig. 5.9b). Significant melt is present over almost the entire ice sheet, which can be ascribed to the warm summer of 2012 alone, when at the 12th of July 99% of the ice sheet was subject to surface melt according to satellite observations (Nghiem *et al.*, 2012) and also in RACMO2 (Figure 5.9c). Melt duration also strongly increased by up to 25 days in the far north and over the western slopes of the ice sheet. The largest increase in melt duration is found over the higher ablation area and the lower accumulation area in the southwest, but not at lower elevations. The reason is that at these lower elevations, the surface was already subject to melt for the entire summer season and extra melting days can only be gained in spring and autumn. The very strong seasonal cycle in temperature confines the melt season mainly to the summer months even in a warming climate. Therefore, the increase in melt duration is mainly caused by an increase of the melt extent in the summer months rather than an increase in the length of the melt season (Fig. 5.9c). Averaged over the summer months (JJA), the area of the GrIS that experiences melt has increased from 17% during 1960-1990 to 27% for 2007-2012 and 36% in the record melt year 2012.

## 5.6.2 Surface mass balance components

The increase in melt duration and extent does not necessarily imply that the GrIS has lost mass via surface meltwater runoff. This requires assessment of all the surface mass balance (SMB) components, because increased precipitation or refreezing of meltwater can partly offset the mass loss. Table 5.2 presents GrIS SMB and its components as simulated by RACMO2. Figure 5.10 displays annual SMB components for 1960-2012. During 1960-1990, the total SMB has been relatively constant, and variability mainly driven by precipitation anomalies. An increase in melt and runoff since 1990 is compensated by increased precipitation, keeping SMB rather constant at ~400 Gt yr<sup>-1</sup>. Since ~2000, the combination of precipitation rates returning to normal and increasing meltwater runoff has resulted in decreasing, with a record low value in 2010 (+102 Gt). The regime shift in the mid-to-late 1990s is clearly seen when SMB components are presented as cumulative anomalies with respect to 1960-1990 (Fig. 5.11). The cumulative melt anomaly reaches 3400 Gt in 2012, i.e. more than 4 times the annual accumulation rate. About 70% (~2200 Gt) has left the ice sheet as runoff, flowing into the surrounding oceans. The other 30% is refrozen in the firn pack. Compared to these values, the cumulative anomalies of snowfall and rain-

5. Contemporary (1960-2012) evolution of the climate and surface mass balance of the Greenland ice sheet

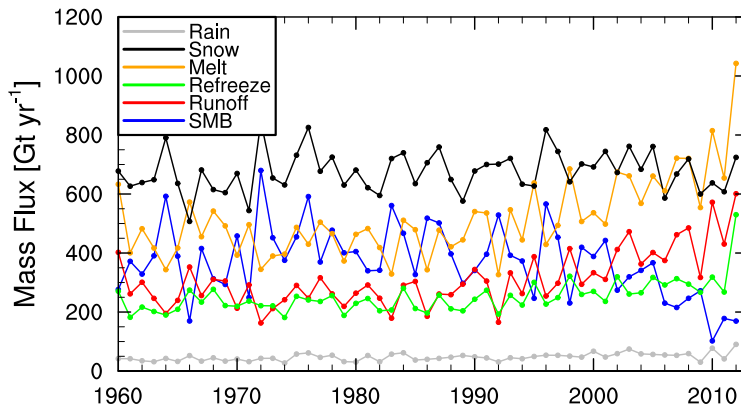


**Figure 5.9:** a) Days per year with more than 5 mm w.e. surface melt averaged over 1960-1990. b) Change of melting days for 2007-2012 with respect to 1960-1990. c) Fraction of the Greenland ice sheet with surface melt for different time windows. For 1960-1990 the light blue band gives the one standard deviation variability. The numbers in the legend indicate the average melt fraction for the summer months (JJA).



**Table 5.2:** Surface mass balance and its individual components for different time periods averaged over the entire Greenland ice sheet

Time	SMB	Precip	Rain	Melt	Runoff	Refreeze	$SU_{srf}$	$SU_{ds}$
1960-1990	406±110	712 ±79	43±10	450±71	266±53	227±28	15±1	24±3
1991-2000	400±106	747 ±79	48±9	514±102	305±70	258±37	16±3	25±4
2001-2006	330±74	761 ±72	59±9	612±68	389±54	282±33	19±2	22±3
2007-2012	197±61	718 ±71	59±22	751±16	478±102	331±99	18±2	23±1
2010	102	715	77	815	572	319	18±1	22±3
2012	169	814	90	1043	601	530	21	23

**Figure 5.10:** Annual surface mass balance components averaged over the Greenland ice sheet and the total surface mass balance

fall are small. The snowfall anomaly increases until 2005 and shows a small decline afterwards. The combination of these processes results in a cumulated surface mass loss of  $\sim 1800$  Gt, equivalent to  $\sim 5$  mm sea level rise.

Average fields of melt, runoff and refreezing for 1960-1990 and the anomalies for 2007-2011 and 2012 are presented in Figure 5.12. In the reference period, the highest melt rates occur over the (south) western ice sheet ( $\sim 3$  m w.e.), gradually decreasing with increasing elevation and latitude. Regions with melt rates  $> 1$  m w.e. are also present in the northeast at elevations below 1000 m. Melt occurs over the entire southern half of the ice sheet, but refreezing confines runoff to a narrow band, mostly below  $\sim 1500$  m.

During 2007-2011, melt has increased by almost 1 m w.e. (30%) over the western ablation area, but a major part of the ice sheet remains free of melt. The runoff line

5. Contemporary (1960-2012) evolution of the climate and surface mass balance of the Greenland ice sheet

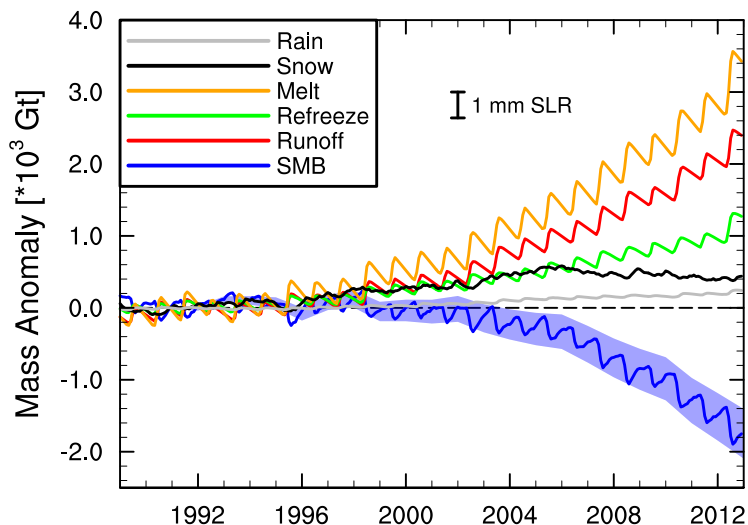


**Figure 5.11:** Cumulated anomaly of surface mass balance components with respect to the 1960-1990 averages. For SMB the light blue band gives the total uncertainty in mass loss based on a  $15 \text{ Gt yr}^{-1}$  uncertainty in SMB anomaly.

has shifted upward to  $\sim 2000 \text{ m}$  for the western ice sheet. For 2012, RACMO2 calculates melt over the entire ice sheet (Fig. 5.12g), in agreement with microwave satellite observations (Nghiem *et al.*, 2012). Not only the extent, but also the rate of melt was extreme in 2012; especially striking are the high melt rates over South Dome, up to  $800 \text{ mm w.e.}$  Because of the thick and porous firn layer higher up the ice sheet, melt water at South Dome is refrozen in the snow pack. However, refreezing rapidly densifies the snow pack, and the significant widening of the runoff zone in Figure 5.12i demonstrates that this buffering effect of the firn layer is limited. The northern parts of the ice sheet also experienced strongly enhanced runoff in 2012, with values of  $\sim 1 \text{ m w.e.}$  at  $1500 \text{ m.a.s.l.}$  Since precipitation rates in the north are relatively small, this region is more vulnerable to a warming climate. Indeed, accelerated surface lowering above  $1200 \text{ m}$  has already been observed in northwestern Greenland (Kjeldsen *et al.*, 2012).

Figure 5.13 presents SMB anomaly fields for 1991-2006, 2007-2011 and 2012 with respect to 1960-1990. During 1991-2006, we see that the negative SMB anomaly of up to  $\sim 200 \text{ mm w.e.}$  is confined to the ablation area, indicative of additional ice melt and runoff. Part of this mass loss is compensated by increased accumulation

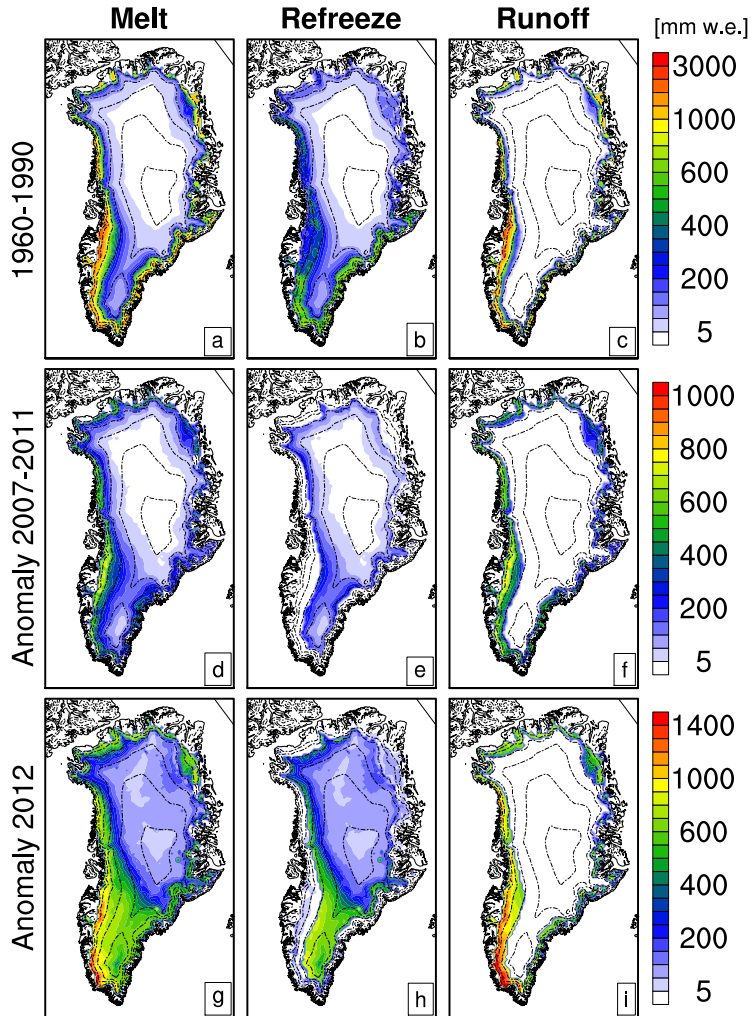


**Figure 5.12:** Averaged annual melt (a), refreeze (b) and runoff (c) for 1960-1990 [mm w.e.] and the anomaly for these components for 2007-2011 (d,e,f) and 2012 (g,h,i). Note the different scales.

## 5. Contemporary (1960-2012) evolution of the climate and surface mass balance of the Greenland ice sheet

---

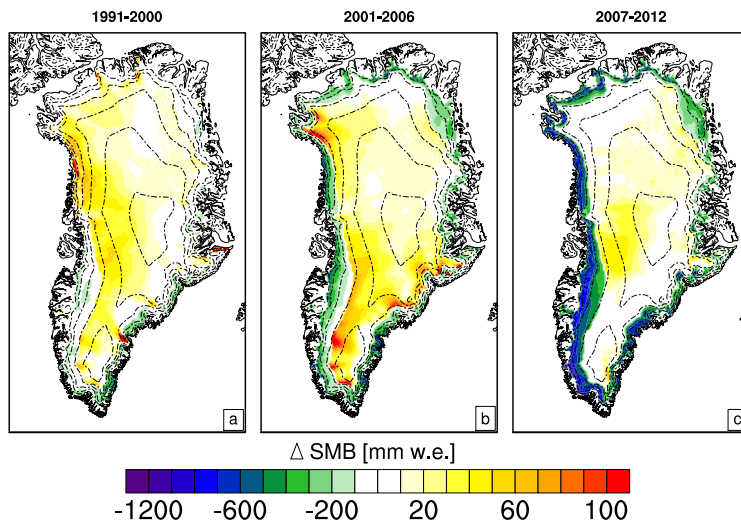


**Figure 5.13:** SMB anomaly fields [mm w.e.] with respect to 1960-1990 for 1991-2006 (a), 2007-2011 (b) and 2012 (c)

(snowfall) over the ice sheet interior. For 2007-2011, melt and runoff anomalies in the ablation area have increased, resulting in extra mass loss up to  $\sim 800$  mm w.e. The positive accumulation anomaly in the interior is no longer present, resulting in the low SMB values for that period. Finally, 2012 returns to the pattern of 1991-2006, with large melt/runoff anomalies in the ablation area and large positive accumulation anomalies on the higher parts, especially for the western half of the ice sheet. This combination has regionally resulted in record melt extent and duration, but due to the relatively high accumulation rates, 2012 does not have the lowest surface mass balance since 1960, at least according to RACMO2.

## 5.7 Conclusions

For the last 7 years, the integrated surface mass balance over the Greenland ice sheet belonged to the 10 lowest values since 1960. Three main causes can be identified. First, the atmospheric circulation has been characterized by a persistently negative NAO-index since 2006. This resulted in an anomalously warm upper air to the west of Greenland, which is then advected to the ice sheet, leading to high surface temperatures and extensive melting. Secondly, the albedo-melt feedback, resulted in 11%

more absorbed shortwave radiation. Finally, the last couple of years, with the exception of 2012, are characterized by relatively low accumulation rates, in contrast to 1991-2006.

Presently there is no leading explanation for the persistently negative summertime NAO-index. If in the coming years the NAO switches back to positive values in summer, the SMB of the GrIS could (partly) recover. In future scenario's, none of the CMIP5 models projects an atmospheric pressure distribution resembling a negative NAO-index. If, on the other hand, during the summer months the warm air advection towards Greenland persists, new record low SMB for the ice sheet can be expected. An important hysteresis effect is introduced by the large amount of water that has in recent years been refrozen in the firn layer. This has significantly increased firn temperatures and reduced porosity. If strong melting persists, the firn layer will first become temperate and then saturated, even at higher elevations, which accelerates runoff.

To better understand and assess the impact of refreezing and retention processes on the SMB of the GrIS, we will continue this research in the near future using a high resolution firn densification model in which also heterogeneous infiltration and horizontal transport of meltwater will be included.

6



# Rapid loss of firn pore space accelerates 21st century Greenland mass loss

---

*Mass loss from the two major ice sheets and their contribution to global sea level rise is accelerating. In Antarctica, mass loss is dominated by increased flow velocities of outlet glaciers, following the thinning or disintegration of coastal ice shelves into which they flow. In contrast, ~55% of post-1992 Greenland ice sheet (GrIS) mass loss is accounted for by surface processes, notably increased meltwater runoff. A subtle process in the surface mass balance of the GrIS is the retention and refreezing of meltwater, currently preventing ~40% of the meltwater to reach the ocean. Here we force a high-resolution atmosphere/snow model with a mid-range warming scenario (RCP4.5, 1970-2100), to show that rapid loss of firn pore space, by >50% at the end of the 21st century, quickly reduces this refreezing buffer. As a result, GrIS surface mass loss accelerates throughout the 21st century and its contribution to global sea level rise increases to  $1.7 \pm 0.5 \text{ mm yr}^{-1}$ , more than four times the current value.*

## 6.1 Introduction

Arctic glaciers, ice caps and ice sheets are melting at an alarming rate (*Hanna et al.*, 2008; *Lenaerts et al.*, 2013; *Rignot et al.*, 2011; *Van den Broeke et al.*, 2009; *Zwally et al.*, 2011). Especially notable is the demise of the Greenland ice sheet (GrIS), which lost an estimated 1000 Gt in the warm summers of 2010 and 2011 alone and contributed ~15% to 1992-2011 global sea level rise (*Rignot et al.*, 2011; *Shepherd et al.*, 2012). In Antarctica, mass loss is primarily caused by the acceleration of outlet glaciers in the Antarctic Peninsula and the Amundsen Sea sector of West Antarctica (*Pritchard et al.*, 2012; *Rignot et al.*, 2008b), after thinning or disintegration of the ice shelves into which they flow. In contrast, glacier acceleration (i.e. ice discharge by calving) and meltwater runoff are about equally important in explaining post-1992 GrIS mass loss (*Van den Broeke et al.*, 2009). In the future, when the ice sheet retreats on land and loses contact with the ocean, runoff will become the dominant process of GrIS mass loss (*Goelzer et al.*, 2012).

The surface mass balance (SMB) of an ice sheet represents the complex balance between mass gain by accumulation (mainly snowfall) and mass loss by ablation (sublimation, runoff). Runoff is governed by the liquid water balance, the sum of water sources (rainfall and melt) and sinks (retention and refreezing). A key process for GrIS mass balance is meltwater retention and refreezing in the firn layer (*Harper et al.*, 2012), currently preventing  $42 \pm 4\%$  of the rain and meltwater from reaching the ocean (*Van Angelen et al.*, 2012). Retention and refreezing are determined by the available pore space and temperature of the firn, the layer of compressed snow that covers the GrIS accumulation zone, representing ~90% of the ice sheet surface (*Etema et al.*, 2009). In the absence of suitable remote-sensing techniques, quantifying these processes requires the use of a coupled atmosphere/snow model (*Reijmer et al.*, 2012).

## 6.2 Methods

### 6.2.1 21st century scenario

Here we use the regional atmospheric climate model RACMO2 (*Van Meijgaard et al.*, 2008), interactively coupled to a multilayer snow model that explicitly treats the above processes and includes a prognostic albedo scheme based on snow grain size evolution (*Kuipers Munneke et al.*, 2011; *Van Angelen et al.*, 2012). All model simulations are fully transient, which is important because of the long memory of up



to several decades of the Greenland firn. When forced at the lateral boundaries and sea surface temperature by global reanalysis of the European Centre for Medium-range Weather Forecasts (ECMWF, ERA-40 from 1958-1978 and ERA-Interim from 1979-present), RACMO2-fERA (RACMO2 forced by ERA), realistically reproduces the contemporary climate and SMB of the GrIS (Ettema *et al.*, 2010a), including post-2002 mass loss as measured by the twin satellites of the Gravity Recovery And Climate Experiment (GRACE, Rignot *et al.* (2011); Van den Broeke *et al.* (2009); Fig. 6.1). The independent evaluation of GrIS accumulation (Ettema *et al.*, 2009), melt (satellite, Fettweis *et al.* (2011)) and SMB (GRACE, Van den Broeke *et al.* (2009)) also provides robust support for the modeled retention and refreezing.

For the contemporary and future climate (1971-2100), RACMO2 was forced with output of the HadGEM2-ES (Bellouin *et al.*, 2011; Jones *et al.*, 2011) general circulation model (GCM) (RACMO2-fHadGEM2). Out of the 27 GCMs used in the fifth Coupled Model Intercomparison Project (CMIP5), in the framework of the World Climate Research Programme (Taylor *et al.*, 2007), HadGEM2-ES most realistically represents the present-day atmospheric circulation over the GrIS (Fettweis *et al.*, 2012a). This is also valid for RACMO2-fHadGEM2 including precipitation distribution, seasonal cycle of  $T_{2m}$  and SMB components.

To assess 21st century changes in GrIS SMB, we selected the Intergovernmental Panel for Climate Change (IPCC) RCP4.5 scenario; in this mid-range scenario, the global mean  $CO_2$  concentration stabilizes at 650 ppm towards the end of the century resulting in an excess radiative forcing of  $4.5 \text{ W m}^{-2}$  relative to pre-industrial values (Moss *et al.*, 2010). Averaged over the 27 CMIP5 GCMs (Taylor *et al.*, 2007), this scenario results in a  $2.5 \pm 0.8 \text{ K}$  increase in GrIS-average summer (JJA) 2 m temperature ( $T_{2m}$ ) in 2079-98 compared to 1992-2011 (Fig. 6.2a). Note that the 21st century  $T_{2m}$  change in HadGEM2-ES is very close to the ensemble mean. In RACMO2-fHadGEM2, the  $T_{2m}$  increase (2.6 K, Fig. 6.2a) and especially its inter-annual variability (0.8 vs. 0.3 K, Fig. 6.2b) are significantly larger than in the host model. This arises from a better resolved surface layer and a more realistic representation of snow albedo in RACMO2, which reacts sensitively to snow metamorphism at higher temperatures, introducing a positive feedback in the response of  $T_{2m}$  over snow (Van Angelen *et al.*, 2012), leading to larger variability. The importance of a realistic representation of (near-)surface processes is further underlined by the weak correlation ( $r^2 = 0.15$ ) between de-trended annual mean  $T_{2m}$  in HadGEM2-ES and RACMO2-fHadGEM2 averaged over the GrIS (Fig. 6.2c).

## 6. Rapid loss of firn pore space accelerates 21st century Greenland mass loss

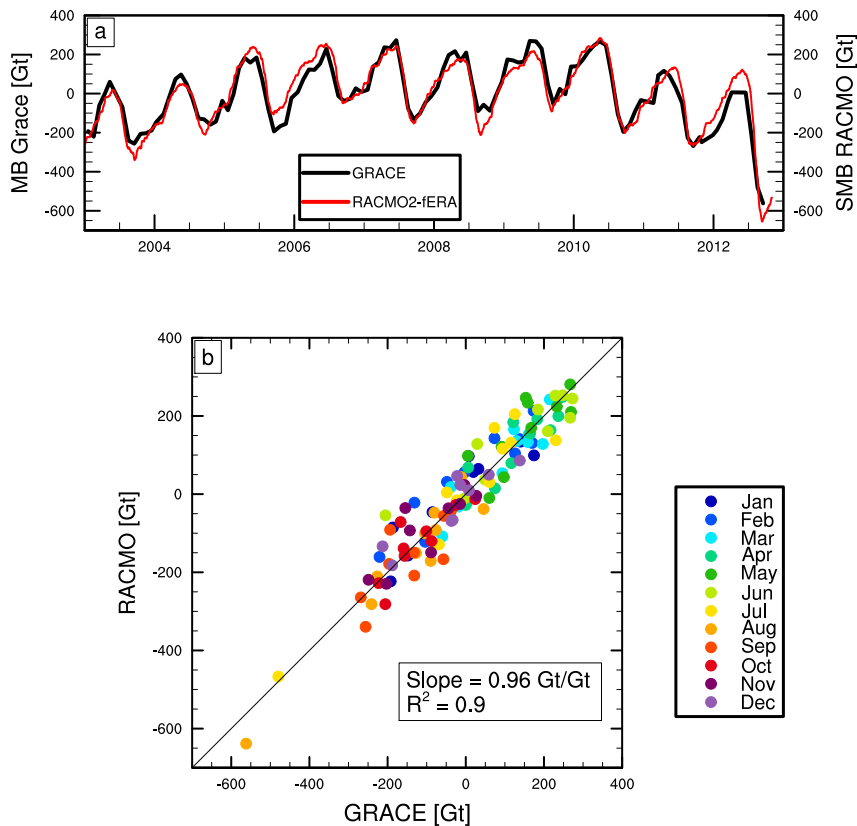


**Figure 6.1:** a) Time series of de-trended mass balance observations from GRACE (black) and daily cumulative SMB calculations from RACMO2 (red). b) Monthly mass balance for GRACE vs RACMO2-fERA.

### 6.2.2 Regional atmospheric climate model RACMO2

For this study we use output of the regional atmospheric climate model RACMO2, originally developed at the Royal Netherlands Meteorological Institute (KNMI, *Van Meijgaard et al. (2008)*). The model is extended with a multi-layer (100) two-way coupled snow routine (*Ettema et al., 2010a*) and a drifting snow scheme (*Lenaerts et al., 2012b*) to better represent conditions in the polar regions. Surface meltwater is allowed to penetrate to deeper layers, where it can be retained or refrozen as de-

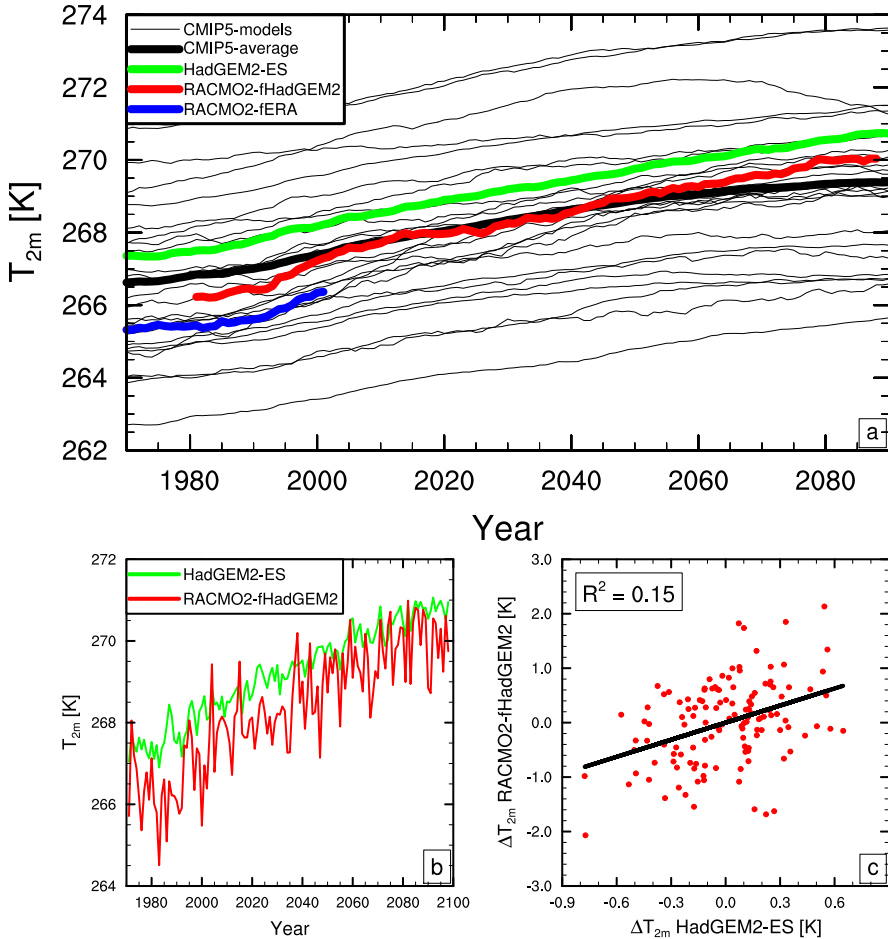


**Figure 6.2:** a) 21 year running mean 2 m summer (JJA) temperature averaged over the Greenland ice sheet (GrIS) for all CMIP5 (Taylor et al., 2007) members, with HadGEM2-ES (green); RACMO2-fHadGEM2 (red) and RACMO2-fERA (blue). b) RACMO2-fHadGEM2 (red) and HadGEM2-ES (green) 2 m temperature averaged over the GrIS. c) De-trended correlation for  $T_{2m}$  averaged over the GrIS between HadGEM2-ES and RACMO2-fHadGEM2.

scribed in *Bougamont and Bamber (2005)*. As soon as all the layers have reached their maximum retention capacity, runoff initiates. Although meltwater penetration is a highly heterogeneous process (piping, horizontal and vertical transport *Parry et al. (2007)*), at an 11 km resolution a homogeneous description, including the formation of ice lenses, is acceptable. Recently, a grain size dependent albedo scheme has been implemented in RACMO2 (*Kuipers Munneke et al., 2011*) for a better simulation of the transition from accumulation to ablation conditions on ice sheets in a warming climate (*Van Angelen et al., 2012*).

The good agreement between RACMO2 and GRACE (Fig. 6.1), including the strong mass loss in the summer of 2012, underlines the capability of RACMO2 to correctly simulate the SMB of the Greenland ice sheet in a warming climate. Figure 6.1 can be used as validation for the retention/refreezing scheme in RACMO2. Since model accumulation is well-evaluated (*Ettema et al., 2009*), as is melt extent (*Fettweis et al., 2011*), refreezing/retention is the only remaining unknown. Refreezing and retention in an absolute sense are very sensitive to small changes in the refreezing scheme due to the albedo-feedback (*Van Angelen et al., 2012*). However, a recent study in the framework of the new IPCC report demonstrated that the uncertainty in retention/refreezing among different regional climate models is estimated at  $40 \text{ Gt yr}^{-1}$ , or 20% of the average refreezing. The uncertainty in year to year variability is much smaller, i.e.  $4 \text{ Gt yr}^{-1}$ . This demonstrates that uncertainty in the retention scheme has a relatively small impact on the final results.

The RACMO2 domain covers Greenland, its surrounding oceans including Iceland and Svalbard and the Canadian Arctic Archipelago. The model resolution is 11 km horizontally and there are 40 levels in the vertical. At the boundary, a relaxation zone of 32 grid points (350 km) is used for the relaxation from the GCM forcing fields to the RACMO2 interior grid.

For the initialization of the snow pack, output for September 1989, (i.e. before Greenland warming started), of a previous RACMO2 simulation over Greenland (*Ettema et al., 2010a*) is used for both the RACMO2-fERA and the RACMO2-fHadGEM2 simulations. Analysis of snow density and temperature profiles show that the top 20 m of the snow pack adjust within a few years to the climate conditions of the specific forcing. This adjustment is clearly visible in Figure 6.12c, where the total amount of pore space in the top 20 m shows a drop after the model start-up, and becomes constant until warming begins in the 1990's. The 20 years (1970-1989) used here are thus sufficient for the snow pack to adjust to the HadGEM2 forcing.

Forcing fields from the HadGEM2-ES scenario run used in this study were available until November 2099. Therefore, 2098 is the last complete year in the RACMO2-fHadGEM2 simulation and we use the 20-yr period 2079-2098 in our analysis.

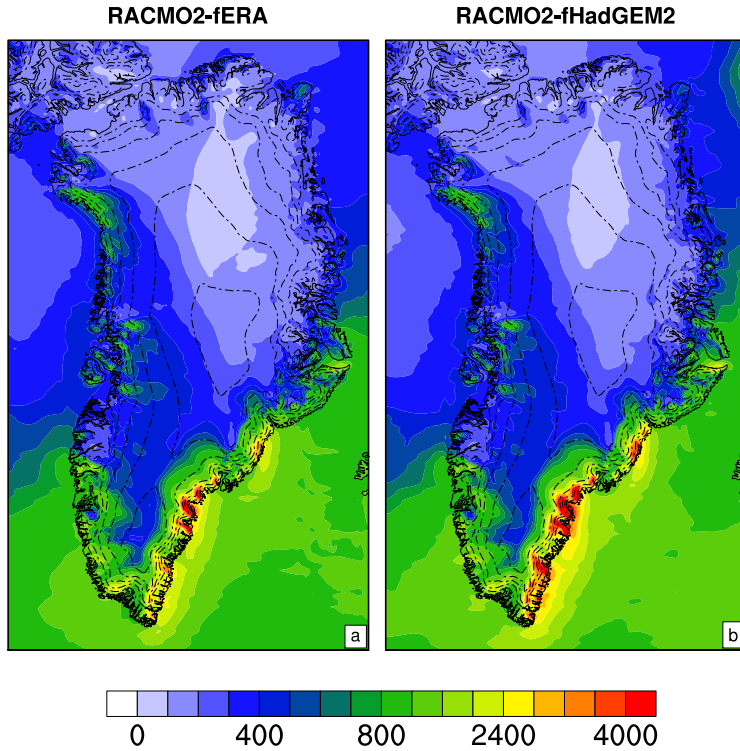


**Figure 6.3:** Yearly averaged precipitation (mm w.e.) for the period 1992-2011 for RACMO2-fERA (a) and RACMO2-fHadGEM2 (b). Dashed contours are 500 m elevation intervals.

## 6.3 Model evaluation

For the 20 year period 1992-2011 there is a 1.0 K warm bias in  $T_{2m}$  for the summer months (JJA) averaged over the GrIS for the RACMO2-fHadGEM2 simulation compared to RACMO2-fERA (Table 6.1). The discrepancy is largest over the northern part of the ice sheet ( $\sim 1.5$  K) and smallest over the central dome and the south-western ablation area ( $< 0.5$  K). Considering precipitation, RACMO2-fHadGEM2 is  $\sim 6\%$  wetter and the patterns are in very good agreement (Fig. 6.3). Also the seasonal cycle for temperature, melt-extent and precipitation are in good agreement for the two simulations (Fig. 6.4). Due to the warm summer bias, the surface mass balance in

6. Rapid loss of firn pore space accelerates 21st century Greenland mass loss

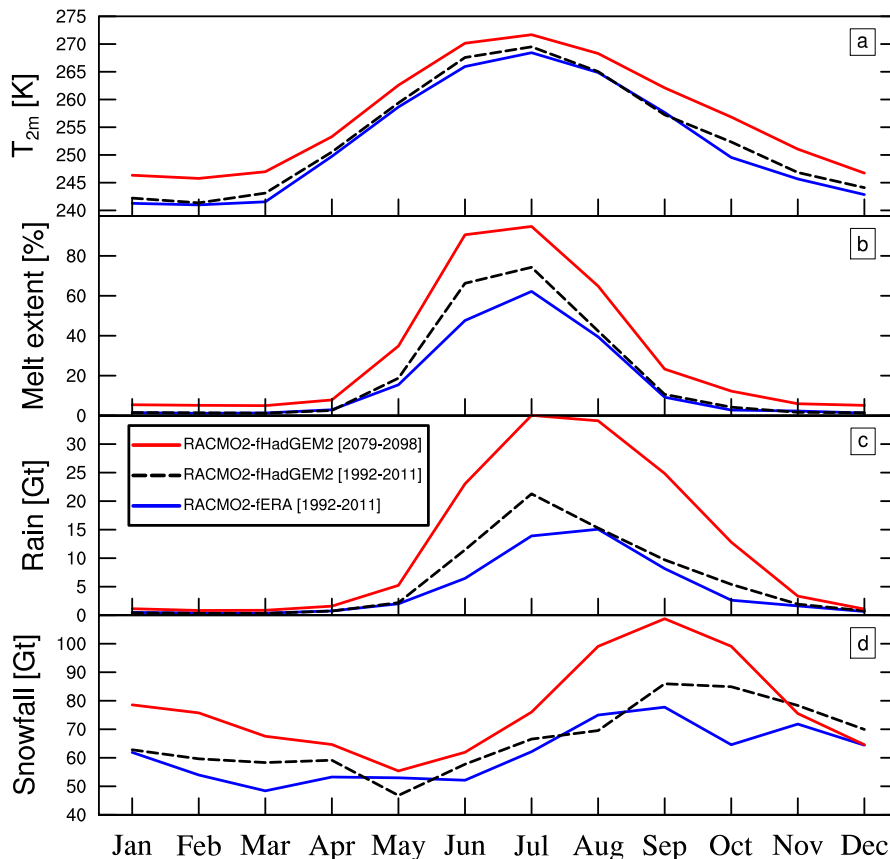


**Figure 6.4:** Seasonality in 2 m temperature (a), melt-extent (b), rainfall (c) and snowfall (d) for RACMO2-fERA (1992-2011) and RACMO2-fHadGEM2 (1992-2011 and 2079-2098).

RACMO2-fHadGEM2 shows a wider ablation area along the south-west and north of the GrIS compared to RACMO2-fERA, but once more the patterns are very similar (Fig. 6.5).

Averaged over the GrIS, the total SMB for the 1992-2011 period is 104 Gt lower for the RACMO2-fHadGEM2 simulation. The standard deviation of annual SMB values for the HadGEM2 simulation (144 Gt) is larger than the difference between the two simulations, so we conclude that the GrIS is in the same climate regime in

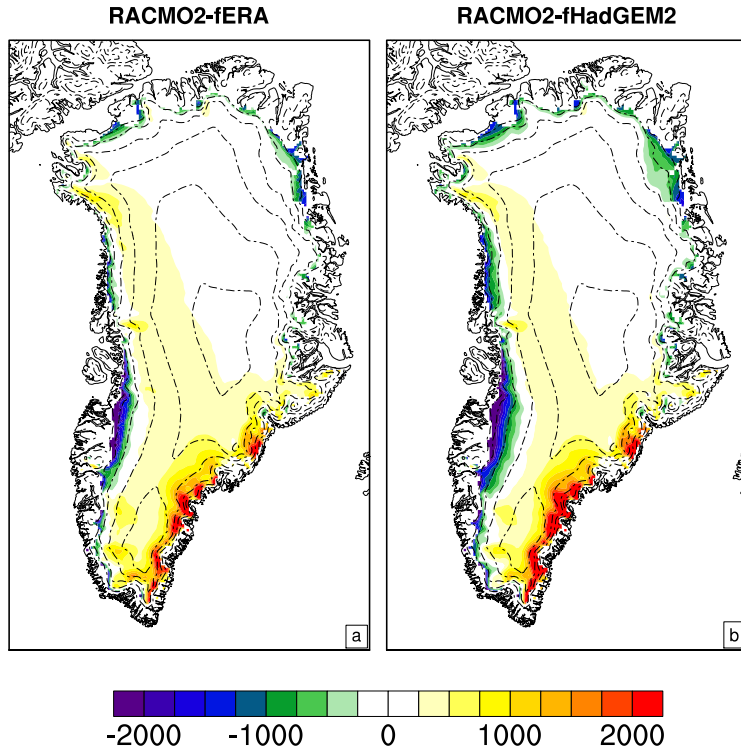


**Figure 6.5:** Yearly averaged SMB (mm w.e.) for the period 1992-2011 for RACMO2-fERA (a) and RACMO2-fHadGEM2 (b). Dashed contours are 500 m elevation intervals.

both simulations. This is further illustrated in Fig. 6.6 where the correlation between summer temperature (JJA) and SMB is shown for both climate realizations. The linear dependency of SMB on temperature is close to  $-100 \text{ Gt K}^{-1}$  and similar for both simulations. For the present day climate, anomalies of the individual surface mass balance components show very good agreement (inset Fig. 6.15). This supports the assumption that anomalies can be used to assess 21st century GrIS mass loss.

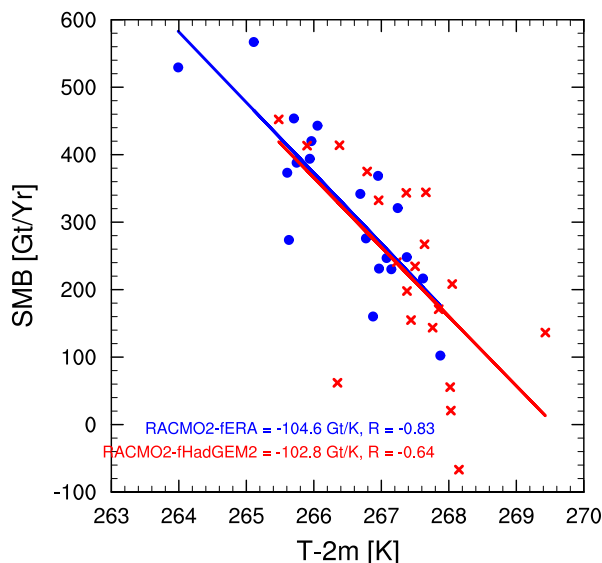


**Figure 6.6:** SMB as function of JJA 2 m temperature for the 1992-2011 period for RACMO2-fERA (blue) and RACMO2-fHadGEM2 (red).

## 6.4 Results

### 6.4.1 Temperature and circulation

Fig. 6.7a shows  $T_{2m}$  and 500 hPa height contours for the RACMO2-fHadGEM2 simulation for 1992-2011. The characteristic southwesterly flow over the ice sheet is present and does hardly change towards the end of the century (Fig. 6.7b). For the summer months (JJA), near-surface temperatures are at or close to the melting point over low lying areas of the ice sheet (<1500 m) and gradually decreasing with elevation. At the end of the century (2079-2098) upper air temperatures show a smooth increase varying between 2.5 and 3.5 K (Fig. 6.7b). Strongest increase is simulated to the northeast of the ice sheet. Near-surface warming shows more spatial variability (Fig. 6.7c). Strongest increase in summer temperatures are present over the central part of the GrIS (>4 K), because temperature rise is not yet limited by the melting surface. The latter process causes the rather weak temperature rise over the low lying regions. Over the ocean, near surface temperatures increase on average by  $\sim 1$  K, stressing the large heat capacity and relatively slow warming of oceans com-



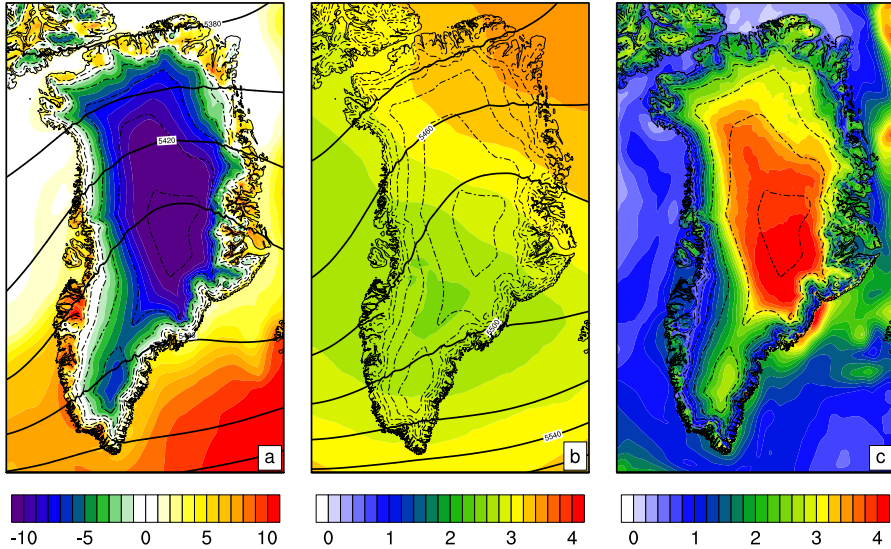


**Figure 6.7:** Averaged JJA RACMO2-fHadGEM2 a)  $T_{2m}$  [ $^{\circ}$ C] and 500 hPa geopotential height [gpm] (1992-2011), b) 500 hPa temperature change for 2079-2098 compared to 1992-2011 and geopotential height (2079-2098), c)  $\Delta T_{2m}$  for 2079-2098 compared to 1992-2011

pared to land areas. It should be noted that ocean temperatures are used as forcing in RACMO2 and not calculated explicitly.

## 6.4.2 Surface energy balance

Averaged over the entire ice sheet, simulated JJA albedo for 2079-2098 compared to 1992-2011 decreases from 0.763 to 0.721. Strongest decrease is found over the northern edge of the ice sheet (Fig. 6.8a). This relatively dry region is most sensitive to climate change, because of the strong impact melt has on the top layer of the snowpack. In other regions, especially southeast Greenland, with high accumulation rates, the surface albedo is hardly affected by increased melting. The spatial increase in  $S W_{net}$  (Fig. 6.8b) is strongly correlated to decreased albedos. Averaged over the ice sheet  $7.2 \text{ Wm}^{-2}$  extra solar radiation is absorbed at the surface (+11%). The increase in absorption of shortwave radiation is suppressed by a reduction of incoming radiation at the surface ( $-15 \text{ Wm}^{-2}$  or 5.5%). This is caused by an increase in cloud cover.

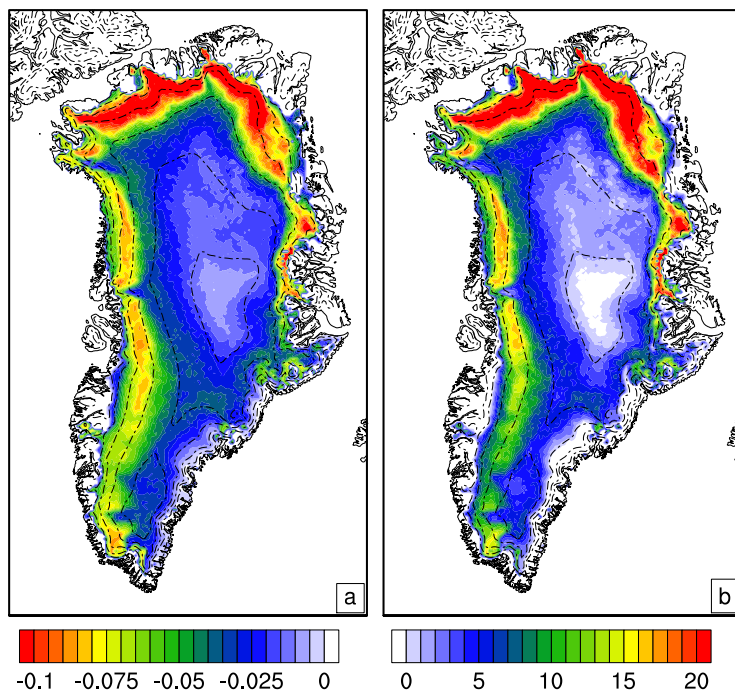


**Figure 6.8:** JJA albedo (a) and  $SW_{net}$  [ $Wm^{-2}$ ] (b) change for the RACMO2-fHadGEM2 simulation between 2078-2098 and 1992-2011.

The increased cloud cover is also reflected in the long wave radiation balance (Fig. 6.9b).  $LW_{net}$  increases with  $6.6 Wm^{-2}$ , only slightly more than the increase in  $SW_{net}$ . The spatial variability in increase of  $LW_{net}$  is small. The strongest increase is found over the southeastern ice sheet, where surface temperatures and thus  $LW_{out}$  remains constant towards the end of the century. Averaged over the GrIS, changes in the sensible and latent heat fluxes are small,  $+0.1 Wm^{-2}$  and  $+0.6 Wm^{-2}$  respectively. The larger temperature difference between the surface and the boundary layer for areas of the GrIS subject to melt, are reflected in a positive anomaly of for both SHF and LHF. Over the interior of the ice sheet the surface warms more compared to the boundary layer, implying a decrease in the heat fluxes.

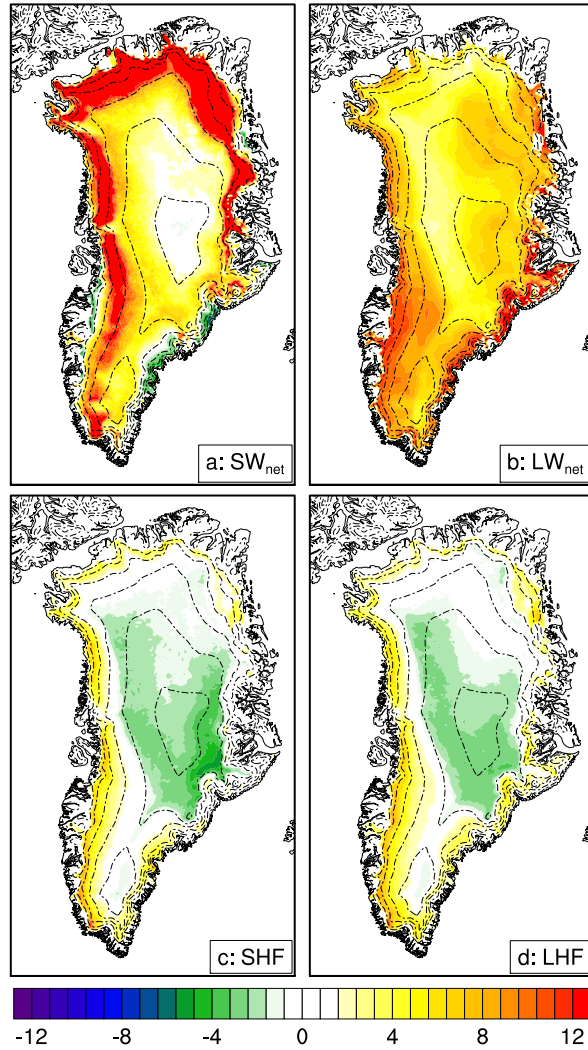


**Figure 6.9:** RACMO2-fHadGEM2 difference fields between the summer months of 2079-2098 and 1992-2011 for  $SW_{net}$  (a),  $LW_{net}$  (b),  $SHF$  (c) and  $LHF$  (d) [ $Wm^{-2}$ ]. All fluxes are defined positive when directed towards the surface.

## 6. Rapid loss of firn pore space accelerates 21st century Greenland mass loss

**Table 6.1:** SMB components [ $Gt\ yr^{-1}$ ] and 2 m temperature [K] for the RACMO2-fERA (1992-2011), RACMO2-fHadGEM2 (1992-2011 and 2079-2098) and differences between the two RACMO2-fHadGEM2 periods.

	RACMO2-fERA (1992-2011)	RACMO2-fHadGEM2 (1992-2011)	RACMO2-fHadGEM2 (2079-2098)	Difference
$T_{2m}$	252.3±1.1	253.3±1.3	256.8±0.6	+3.5
$T_{2m\ JJA}$	266.4±1.0	267.4±1.0	270.0±0.7	+2.6
<i>SMB</i>	329±121	225±144	-233±179	-458
<i>Snowfall</i>	686±62	731±77	783±56	+53
<i>Rain</i>	53±12	70±18	144±35	+74
<i>Melt</i>	586±118	791±147	1439±212	+648
<i>Runoff</i>	368±95	531±107	1120±177	+589
<i>Refreeze</i>	271±37	329±53	462±62	+133
<i>Sublimation</i>	41±4	44±4	40±4	-3
<i>Refreeze cap.[%]</i>	42±4	38±4	29±2	-9

### 6.4.3 Surface mass balance

In this combination of scenario and models, 10-yr running average GrIS SMB turns negative around 2070 (Fig. 6.10). Because solid ice discharge (iceberg calving) is a definite negative term in the ice sheet mass balance,  $SMB = 0$  is sometimes interpreted as a tipping point beyond which an ice sheet cannot recover. The reason that this threshold is reached so soon is that the increase in snowfall on the GrIS (+53  $Gt\ yr^{-1}$  in 2100, Table 6.1) is by far insufficient to compensate the simultaneous increase in runoff (+589  $Gt\ yr^{-1}$ ). In the current climate, the refreezing capacity of the GrIS is  $42 \pm 4\%$  in RACMO2-fERA ( $38 \pm 4\%$  in RACMO2-fHadGEM2), indicating that 42% of the total liquid water flux (rain plus melt, Fig. 6.11a) is refrozen in the firn, the layer of compressed snow that covers the accumulation area of the ice sheet (Fig. 6.11b). This efficient refreezing of meltwater confines runoff to a narrow band along the ice sheet margin (Fig. 6.11c). In the current climate, runoff above 1500 m is only found in the southwest and to a lesser extent in the northeast GrIS; these are dry and sunny regions with relatively high summer melt rates, where the cold content of the shallow winter snowpack is quickly removed in spring.

At the end of the 21st century, the full ice sheet experiences melt on a seasonal basis (Fig. 6.11d, note that rain is confined to elevations < 2000 m). By that time, runoff is only significantly suppressed by refreezing at the highest elevations (Fig. 6.11e) and the runoff zone has expanded far into the ice sheet interior, reaching elevations above 2500 m asl in the south, even crossing the ice divide (Fig. 6.11f). Total liq-

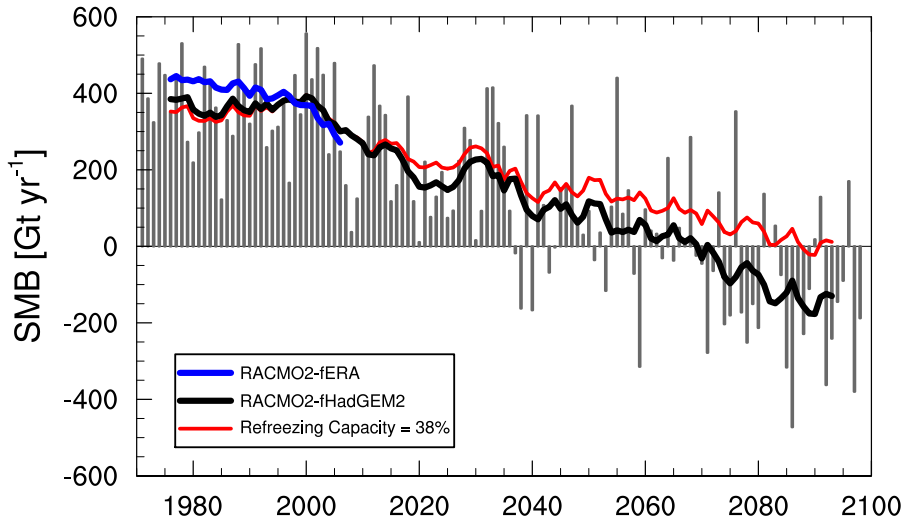


**Figure 6.10:** Annual SMB for RACMO2-fHadGEM2 (grey bars), with 11-year running average SMB for RACMO2-fERA (blue), RACMO2-fHadGEM2 (black) and RACMO2-fHadGEM2, assuming the refreezing capacity remains constant at 38% throughout the 21<sup>st</sup> century (red). 104 Gt is added to the RACMO2-fHadGEM2 SMB to correct for the SMB bias between the two simulations for the present day (1992-2011) (Table 6.1).

uid water production increases strongly (rain and melt, +722 Gt yr<sup>-1</sup>), yet refreezing only modestly increases in comparison (+133 Gt yr<sup>-1</sup>). In the RACMO2-fHadGEM2 simulation the refreezing capacity is reduced from 38% to 29% at the end of the 21<sup>st</sup> century (Fig. 6.12c, blue line). This represents a 24% decrease in refreezing capacity in less than a century's time. The loss of refreezing capacity is concentrated in the lower accumulation area, and marks the transformation of accumulation zone, with net annual surface mass gain, to ablation zone, where surface mass is lost on an annual basis. To demonstrate the impact of the reduction in refreezing capacity, we added to Fig. 6.10 the hypothetical situation in which the refreezing capacity of the GrIS were to remain constant throughout the 21<sup>st</sup> century. In that scenario, the SMB would remain positive for several decades longer.

The reason for this loss of refreezing capacity is twofold. Upon refreezing in the cold firn sections of the ice sheet, the massive release of latent heat causes average firn temperature to increase by 4-5 K towards the end of this century. Locally this firn warming is projected to be as large as 18 K (Fig. 6.13) at locations where refreezing and thus latent heat release increase most significantly (Fig. 6.11e). More

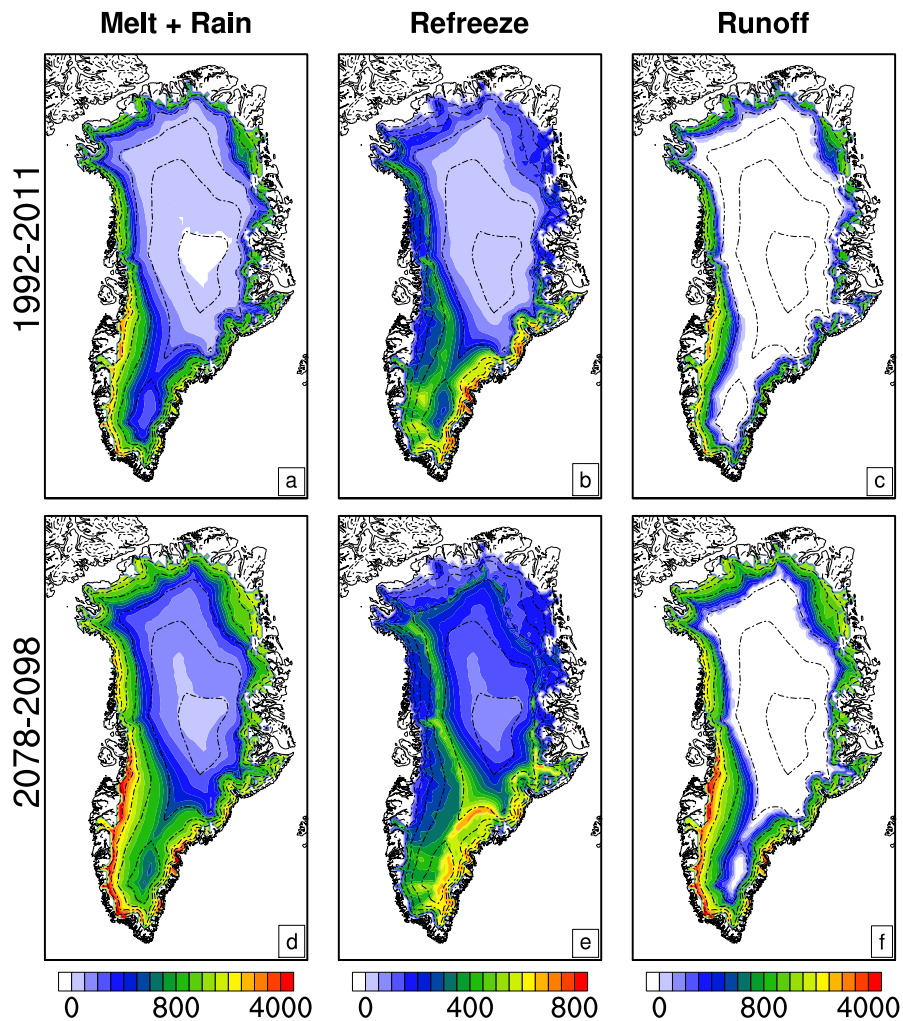


**Figure 6.11:** Yearly averaged melt + rain (left), refreezing (middle) and runoff (right) (mm w.e.) for 1992-2011 (top) and 2079-2098 (bottom) according to the RACMO2-fHadGEM2 simulation. Note the different scales. Dashed contours are 500 m elevation intervals.

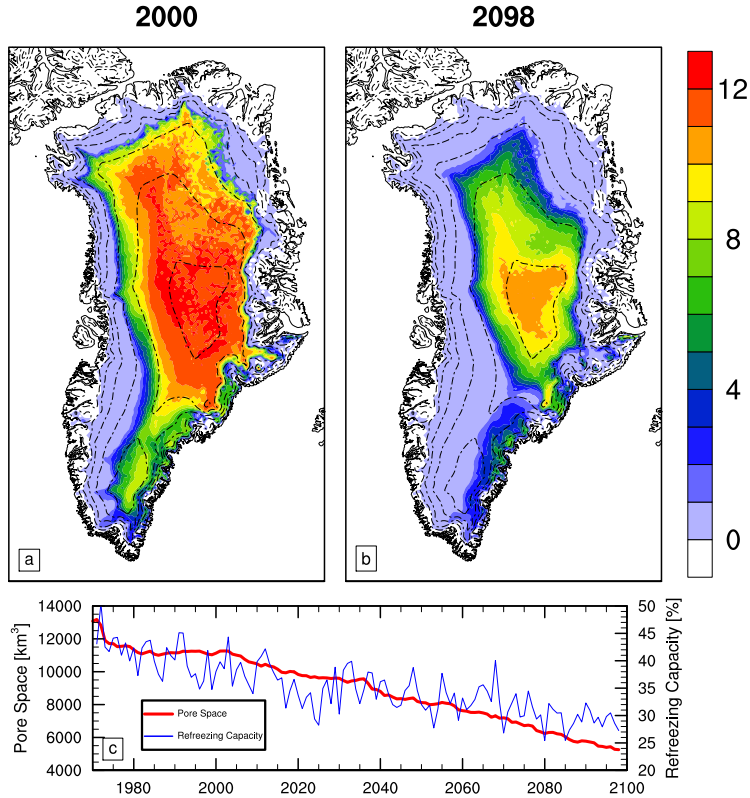


**Figure 6.12:** Vertically integrated pore space [ $m$  air], RACMO2-fHadGEM2) over the top 20 m of the snow pack averaged for the years 2000 (a) and 2098 (b). Dashed contours are 500 m elevation intervals. c) Total GrIS pore space in the top 20 m of the snow pack (red, left axis) and refreezing capacity (percentage of rain and meltwater that refreezes, blue, right axis).

importantly, refreezing enhances firm densification by replacing air in the firm (pore space) with ice. The associated reduction of pore space prevents liquid water from being retained and refrozen when the winter cold wave penetrates downwards into the firm. Fig. 6.14 demonstrates that pore space availability is the main limiting factor for refreezing; moreover, the temporary damping effect on mass loss of increased refreezing when melt and rain increase (Harper *et al.*, 2012), is only short-lived. For north-east Greenland, the transition of the firm layer to ice takes approximately 2

decades, for regions with higher precipitation and melt rates, the process is even faster ( $\sim 10$  years). From Fig. 6.14 it can be deduced that approximately 80% of the initial pore space is used by additional refreezing. Fig. 6.12 illustrates the dramatic loss (50 %) of pore space, in the top 20 m of the firn layer, towards the end of the century. During the last 20 years of the simulation, when the atmospheric warming ceases, the amount of pore space in the firn layer continues to decrease. This illustrates that the snowpack is still adjusting to the new climate, particularly in the colder and drier (northern and most elevated) parts of the ice sheet. The firn layer is thermally active for approximately the upper 10 m of the firn pack, on average. Therefore, as a safe limit, we included the top 20 m of the snow pack in our analysis. We also tested whether the inclusion of deeper layers would alter the results, but this was not the case.

The increasing temperature and decreasing pore space in the upper (active) part of the firn layer, both caused by enhanced liquid water penetration, force a rapid decline of the refreezing capacity of the GrIS. As a result, projected GrIS runoff continues to accelerate during the 21st century (Fig. 6.15, blue line), despite stabilizing temperatures. The cumulative runoff anomaly reaches  $30 \pm 4 \cdot 10^3$  Gt in 2100. The projected increase in snowfall compensates less than 10% of this, resulting in a projected end-of-century GrIS additional mass loss of  $24 \pm 5 \cdot 10^3$  Gt, equivalent to  $7 \pm 1$  cm of eustatic sea level rise. The annual mass loss rate is  $1.2 \text{ mm yr}^{-1}$  at the end of the century; because we consider anomalies with respect to 1992-2011, this must be added to the current GrIS sea level rise contribution ( $\sim 0.4 \text{ mm yr}^{-1}$ ) (Shepherd *et al.*, 2012; Van den Broeke *et al.*, 2011), leading to an annual rate of  $1.7 \text{ mm yr}^{-1}$ , more than four times the current value.

## 6.5 Conclusions

We applied for the first time a fully transient high-resolution simulation of a coupled atmosphere-snow model to the end of this century to assess the state of the Greenland firn and the feedback it has on the surface mass balance. The rapid loss of firn pore space in a warmer climate deteriorates the refreezing capacity of the GrIS; the refreezing buffer of the firn is removed after just several decades of enhanced melt. Although only one warming scenario (RCP 4.5) and one CMIP5 model is applied in this study, the results demonstrate the vulnerability of the Greenland ice sheet under this mid-range warming scenario in the 21st century. A more rapid warming (i.e. RCP 8.5) would result in even faster loss of pore space in the Greenland firn. The increase in contribution from the GrIS to sea level rise as determined in this study is



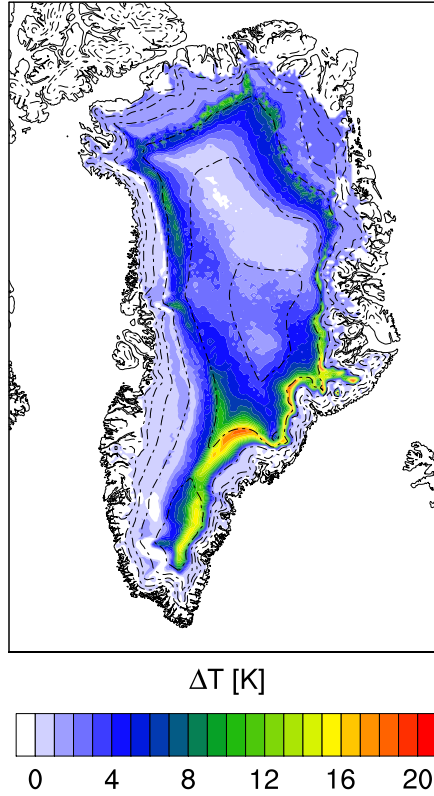


**Figure 6.13:** Temperature change averaged over the top 20 m of snow for the RACMO2-fHadGEM2 simulation between 2078-2098 and 1992-2011. Dashed contours are 500 m elevation intervals.

from surface processes alone, i.e. excluding ice dynamical changes. Moreover, the selected climate scenario is mid-range and the elevation-melt feedback has not been taken into account, the latter becomes more important the longer the projection and will be incorporated in future work. As a result, this estimate of surface mass loss from the GrIS is deemed conservative.

6. Rapid loss of firn pore space accelerates 21st century Greenland mass loss

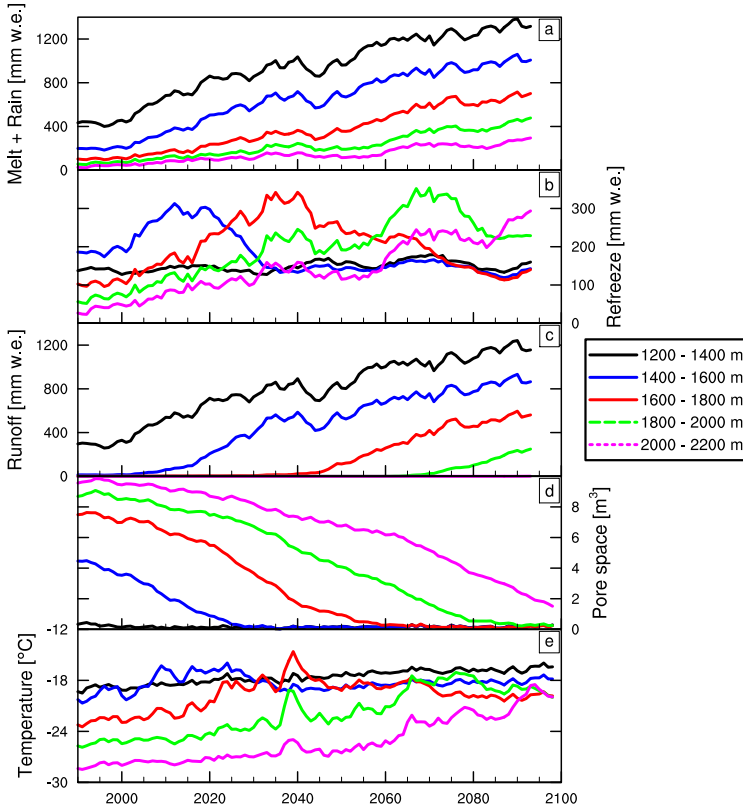


**Figure 6.14:** Melt and rain (a), refreezing (b), runoff (c), pore space (d) and temperature (e) in the top 20 m of the snow pack for northeast Greenland binned in 200 m elevation intervals. For melt and rain, refreezing and runoff, an 11-year running average is applied. Throughout the 21st century the production of liquid water (melt + rain) steadily increases. In the first several decades, this liquid water penetrates into the still porous firn and efficiently refreezes, reducing the pore space and heating the snow pack by latent heat release. When pore space in the firn is zero, refreezing is reduced to the amount that can be accommodated by the cold content of the winter snow layer, and runoff is initiated. The fact that runoff starts before all pore space is removed, is the result of averaging over a 200 m elevation bin; at lower altitudes, pore space has disappeared and runoff has started, whereas higher on the ice sheet pore space is still available.

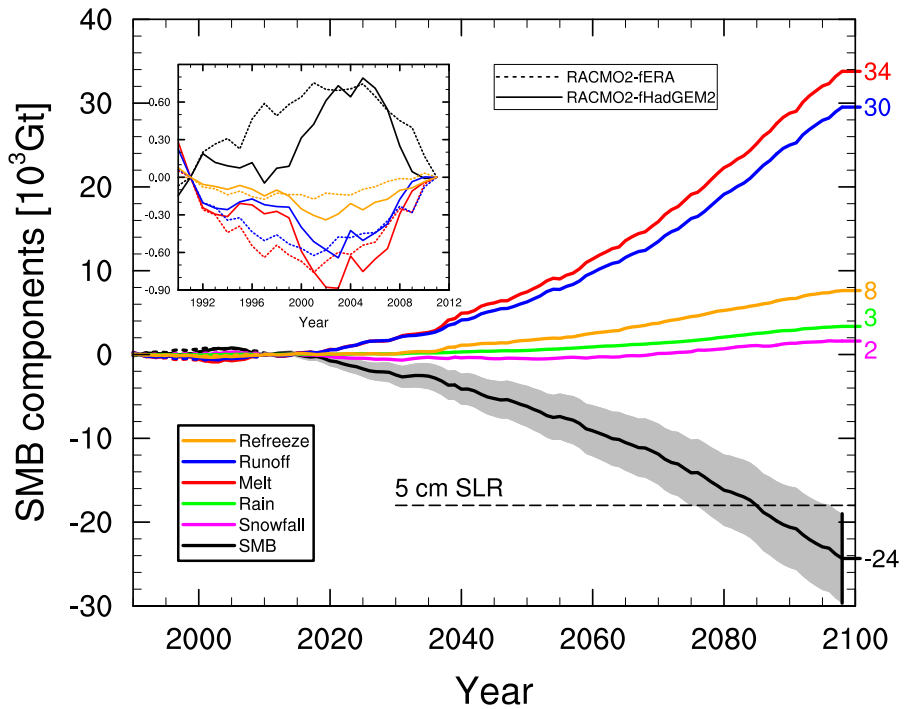


**Figure 6.15:** Cumulative SMB anomalies (black) and individual SMB components with respect to the 1992-2011 reference period for RACMO2 forced by HadGEM2-ES. The uncertainty is based on the present day uncertainty in GrIS SMB (i.e.  $\pm 60$  Gt). The inset expands the period 1992-2011 and compares RACMO2-fHadGEM2 to RACMO2-fERA. Note that  $3.6 \times 10^3$  Gt is approximately equivalent to 1 cm of eustatic sea level rise.

7



## Conclusions, ongoing and future work

---

*The first section of this final chapter summarizes the main results of Chapters 2-6. Secondly I present results of ongoing work with RACMO2, in this case as supporting tool to interpret results from a field project in southeast Greenland where liquid water was unexpectedly encountered in the firn layer in early April, well before the onset of the melt season. We show how output of RACMO2 contributes to the understanding of the formation and maintenance of this perennial liquid water body. The final section presents ongoing work and suggestions and opportunities for future research concerning Greenland climate studies and applications of RACMO2.*

## 7.1 General conclusions

The Greenland ice sheet is losing mass at an accelerating pace. All recent predictions of total mass loss at the end of the 21st century are close to or above the high-end scenario of the 4th Assessment Report of the International Panel on Climate Change in 2007 (IPCC AR4). The reason for this upscaling is twofold. First, there has been an acceleration in mass loss both from solid ice discharge and surface mass balance related processes. Secondly, positive feedback mechanisms (e.g. albedo-melt, meltwater-ice dynamics) are now better understood and incorporated in scenario model simulations and thus in the mass loss predictions.

This thesis contributes to Greenland climate and mass balance research by assessing several physical interactions between the atmosphere and the GrIS, using output of RACMO2, a regional atmospheric climate model adapted to simulate the climate in polar regions and over ice sheets. Insight is gained in the atmospheric circulation over and in the vicinity of the GrIS, such as the variability in strength of the katabatic wind. We discuss the interaction of the katabatic wind with large scale forcing, and how that leads to strong southerly winds over western Greenland. The thermally induced wind forcing that results from the strong temperature gradient between the cold ice sheet and the relatively warm open ocean water is quantified and shown to be strongly correlated to sea ice export through Fram Strait.

The grain size dependent albedo scheme has strongly improved the physical representation of snow in RACMO2, leading to a better agreement between observations and model output. We tested the sensitivity of surface mass balance components to settings in this albedo scheme. Because no direct observations of refreezing are available, the spread in realistic parameter settings for this process is large, giving it the greatest uncertainty and sensitivity in the scheme. However, indirect observations, such as melt extent, greatly reduce the final uncertainty.

Using the upgraded RACMO2 model (i.e. the new albedo scheme and including snowdrift processes), a transient model simulation from 1960-2012 was performed. With respect to the 1960-90 period, total surface mass balance has more than halved over the last two decades, from  $406 \text{ Gt yr}^{-1}$  to  $197 \text{ Gt yr}^{-1}$  averaged over 2007-2012, mainly induced by a more than 2 K near surface temperature increase in summer over the GrIS. The strong warming is not only caused by global warming, but also due to a persistent atmospheric circulation pattern in which from the southwest relatively warm air is advected towards the GrIS. Also relatively low accumulation rates in recent years, with the exception of 2012, enhances the recent low SMB years.

The ability of RACMO2 to realistically simulate contemporary climate and surface mass balance over Greenland, gives confidence to perform a scenario simulation

for the 21st century. RACMO2 was forced with the HadGEM2 GCM for a mid-range warming scenario (RCP4.5) for 1970-2098. For this scenario and combination of models, a 2.6 K increase in summer 2 m temperature is simulated, accompanied by a reduction in SMB of  $460 \text{ Gt yr}^{-1}$  averaged over 2079-2098 compared to 1992-2011. An important reason for the acceleration in mass loss is the reduction of the refreezing capacity of the firn layer covering the GrIS (i.e. the percentage of melt water and rain that is refrozen) from 38% to 29%. Main cause is the strong reduction by more than  $\sim 50\%$  of pore space in the top 20 m of the snow pack, following enhanced refreezing.

## 7.2 Case study: the Greenland firn aquifer

As an example of ongoing work with RACMO2 on GrIS, here we briefly discuss perennial liquid water in the firn covering the ice sheet. During the Arctic Circle Traverse expedition, in April 2011, the traverse team unexpectedly encountered liquid water in the firn covering the GrIS in the southeast, while drilling a core for accumulation measurements. The liquid water was found well before the onset of the melt season, with surface temperatures far below the melting point. At another core site, 3 km to the west at higher elevation, liquid water was found as well. A ground penetrating radar (GPR) profile was made in the vicinity of the core sites, revealing a strong return horizon at depths between 10 and 25 m. At the two core sites the depth of the liquid water table coincides with the strong return signal of the GPR (Fig. 7.1), indicating that the signal is indeed caused by liquid water.

In April 2011, NASA Operation Ice Bridge accumulation radar (AR) completed over 40,000 km of flight lines over the GrIS. Along these flight lines, 843 km were identified to have liquid water in the firn, mostly in southeast Greenland and some patchy regions in the southwest (Fig. 7.2). The liquid water was found at depths between 5 and 50 m, with largest depths in the southeast.

Interestingly, also in the RACMO2 model simulation, liquid water remains present in the snow scheme during the entire winter. Fig. 7.2 displays both the locations of the liquid water as deduced from the AR flight lines as well as in RACMO2. The two independent products are in very good agreement, with even correctly simulated liquid water at the few locations in southwest Greenland. The locations in southeast Greenland where the AR did not retrieve a liquid water layer, but RACMO2 does simulate it, are highly crevassed such that the water easily finds its way through the ice sheet, processes not simulated in RACMO2. From the radar profiles only the depth to the top of the layer can be deduced, whereas RACMO2 also gives a volume; up to

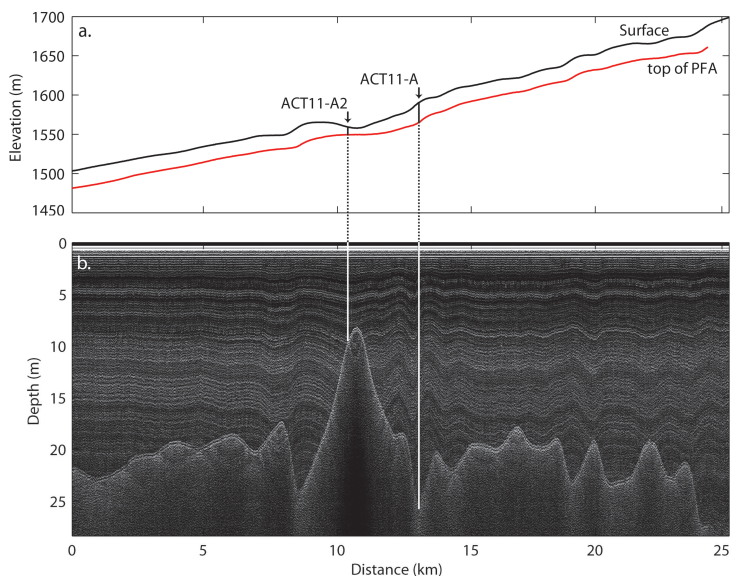


**Figure 7.1:** Profile of the top of the PFA from ground penetrating radar along ACT-11 traverse including PFA firn-core locations (ACT11-A and ACT11-A2). a) Surface elevation profile from simultaneously acquired GPS and topographically corrected GPR PFA top horizon. This indicates the depth to top of the firm aquifer is influenced by the local topographic slope. b) GPR echogram with the top of the firm aquifer as the bright contiguous horizon cutting the numerous internal firm reflecting horizons. (Figure from Forster et al. (2013)),

600 mm w.e. of liquid water is modeled in the firn column locally.

The good agreement between the AR and RACMO2 implies that we can use RACMO2 to analyze the formation and maintenance of this perennial firn aquifer. A simple parameterization indicates that liquid water is found at locations with both high melt and accumulation rates ( $> 700 \text{ mm w.e. yr}^{-1}$ , Fig. 7.3). In summer, during the melt season, the firn layer gets saturated with liquid water, but is not completely melted. In fall, fresh snowfall quickly isolates the wet firn layer from the cold atmosphere. As a result, although part of the liquid water refreezes, not enough heat can be released from the saturated firn layer to refreeze all liquid water resulting in the perennial firn aquifer. From RACMO2 the areal coverage of the perennial liquid water is estimated at  $70 \pm 10 \times 10^3 \text{ km}^2$ . The minimum liquid water volume is reached just before the onset of the new melt season in late April, and equals  $15 \pm 8 \text{ km}^3$  or



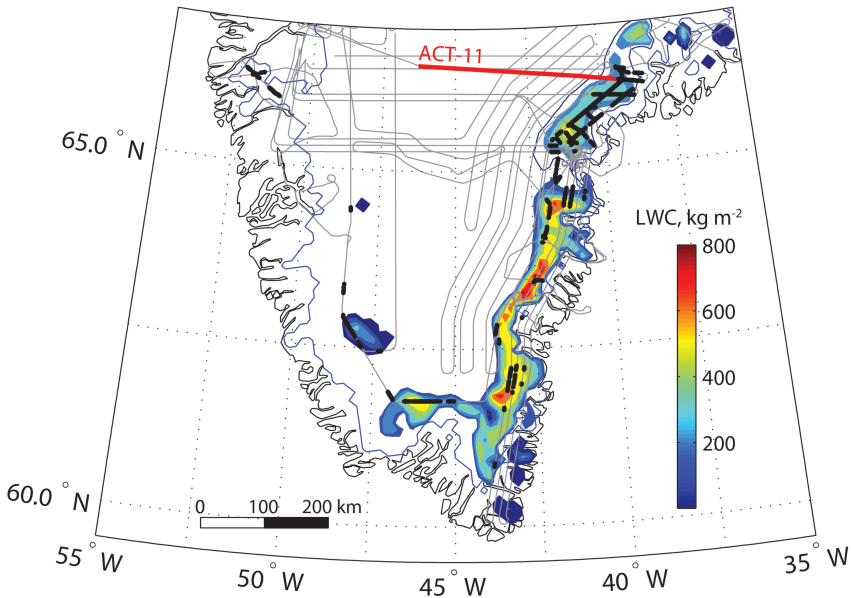


**Figure 7.2:** Modeled liquid water content (LWC, colors) in the firn and detected PFA from airborne radar (black dots). The simulation of LWC is from RACMO2/GR for April 2011. OIB flight lines (gray), ACT-11 traverse (red) in April 2011 (Figure from Forster *et al.* (2013)).

$4 \pm 2\%$  of mean annual runoff for 2001-2010.

On average, the depth to the top of the liquid water layer is shallower in RACMO2 compared to the AR observations. This may be related to the lack of horizontal transport of water in RACMO2 and the lack of vertical penetration of liquid water via crevasses and (on a smaller scale) piping, transporting the water deeper into the ice sheet. Fig. 7.1 underlines the strong correlation between the surface topography and the depth of the liquid water table at a small scale, which is not resolved at the 11 km horizontal resolution of RACMO2. Nevertheless, in first order, RACMO2 is capable to realistically simulate the formation and location of the perennial firn aquifer.

The perennial liquid water forms a new glacier facies for the GrIS. The differences with respect to other areas of the ice sheet is reflected in the absence of supra-glacial lakes in that region, since melt water is retained in the thick firn layer. As a result the

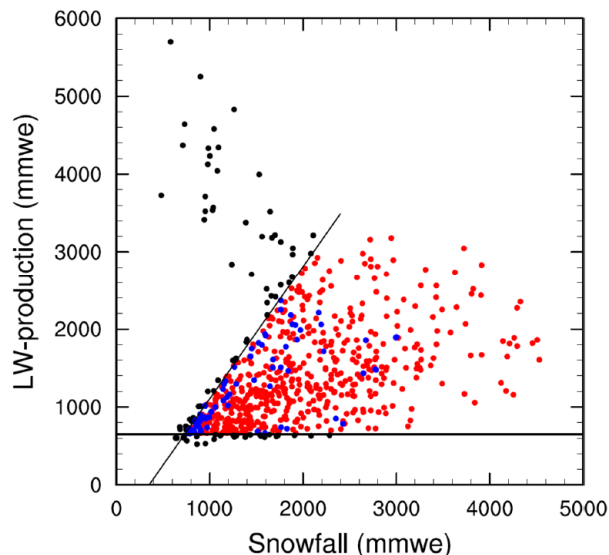


**Figure 7.3:** Scatter plot of RACMO2 SMB components for grid cells which had at least one year with liquid water in the snow pack in April during the period 2001-2010. Snow fall is total solid precipitation during the year and liquid water production is melt water plus rain. The results of this two component parameterization, with the bounds shown, to predict the location of modeled PFA are shown as: red, correctly predicts, blue: predicts but not modeled, and black: does not predict but is modeled.

impact of liquid water on ice sheet dynamics and infiltration to the bed will probably be different in southeast Greenland, and should be taken into account in ice dynamical studies.

### 7.3 Future work

Although over the recent years our understanding of many processes involved in the interaction between the GrIS and the atmosphere has improved, several outstanding questions remain. For example, the rapid warming over Greenland in summer since  $\sim 2005$  is strongly related to changes in the large scale atmospheric circulation, but whether this reflects natural variability or is a sign of global warming (e.g. less sea ice cover, changing ocean circulations) is unclear. A step forward in this understanding would be the analysis of the heat budget over Greenland both close to the surface as

well as the advection of heat towards the ice sheet at higher altitude.

At present a new version of RACMO is tested over Greenland and Antarctica. Changes (improvements) in the radiation scheme and the vertical resolution in the atmospheric part of the model should improve the underestimated downwelling long wave radiation. Furthermore, a more sophisticated snow scheme is implemented for seasonal snow over tundra. This is an important component of the climate of Greenland, because of the rapid warming of the near surface as soon as the winter snow pack has melted.

Concerning surface mass balance processes, the largest challenge remains for the treatment of melt water and rain in the snow/firn layer over the ice sheet. In Chapter 4 we have demonstrated the strong sensitivity of SMB components to small changes in the refreezing scheme. Since direct observations of refreezing and penetration of liquid water are scarce or non-existent, a direct validation of these processes is difficult. Firn/ice cores can be used to evaluate the density profiles as calculated in the snow model. The next step will be made by using RACMO precipitation, temperature and surface energy balance output to force a stand alone high-resolution firn densification model. By using a stand alone firn-model, a higher vertical resolution can be used and it is less expensive to perform multiple simulations to test the sensitivity for certain parameter settings. These experiments will also be carried out for southeast Greenland to get a better understanding of the formation of the perennial firn aquifer.

With ever increasing computer power, in the near future coupled global climate model (GCM) simulations will be carried out at higher horizontal resolution (~25 km). These higher resolutions will result in a better representation of important smaller scale processes, i.e. the steep SMB gradients in the GrIS ablation zone. These model simulations will answer questions such as the impact of a sea ice free Arctic Ocean in summer on GrIS mass and energy balance. Nevertheless, since all interactions between ocean, atmosphere, land and ice surfaces are incorporated in these models the uncertainties in model output will remain large. Therefore, regional climate models there will remain playing a major role in the coming decade. Especially in forcing ice dynamical models, of which the results rely for an important part on the quality of surface mass balance and melt energy input, the output of RCM's at high resolution will remain essential.



# Bibliography

---

- Abdalati, W., and K. Steffen (1997), Snowmelt on the Greenland ice sheet as derived from passive microwave satellite data, *Journal of Climate*, *10*, 165–175, doi:10.1175/1520-0442(1997).
- Abdalati, W., and K. Steffen (2001), Greenland ice sheet melt extent: 1979–1999, *Journal of Geophysical Research*, *106*, 33,983–33,988, doi:10.1029/2001JD900181.
- Armstrong, R., and M. Brodzik (1995), An earth-gridded ssm/i data set for cryospheric studies and global change monitoring, *Advances in Space Research*, *16*(10), 155–163, doi:10.1016/0273-1177(95)00397-W.
- Ball, F. (1956), The theory of strong katabatic winds, *Australian journal of physics*, *9*, 373.
- Bamber, J., R. Layberry, and S. Gogineni (2001), A new ice thickness and bed data set for the Greenland ice sheet 1. measurement, data reduction, and errors, *Journal of Geophysical Research*, *106*, 33,773–33,780.
- Bartholomew, I., P. Nienow, A. Sole, D. Mair, et al. (2011), Supraglacial forcing of subglacial drainage in the ablation zone of the Greenland ice sheet, *Geophysical Research Letters*, *38*, L08,502, doi:10.1029/2011GL047063.
- Bekryaev, R., I. Polyakov, and V. Alexeev (2010), Role of polar amplification in long-term surface air temperature variations and modern Arctic warming, *Journal of Climate*, *23*, 3888–3906, doi:10.1175/2010JCLI3297.1.
- Bellouin, N., et al. (2011), The HadGEM2 family of Met Office Unified Model climate configurations, *Geoscience Model Development*, *4*(3), 723–757, doi:10.5194/gmd-4-723-2011.
- Boggild, C., R. Brandt, K. Brown, and S. Warren (2010), The ablation zone in northeast Greenland: ice types, albedos and impurities, *Journal of Glaciology*, *56*(195), 101–113, doi:10.3189/002214310791190776.
- Bougamont, M., and J. Bamber (2005), A surface mass balance model for the Greenland ice sheet, *Journal of Geophysical Research*, *110*, F04,018, doi:10.1029/2005JF000348.
- Bougamont, M., J. Bamber, J. Ridley, R. Gladston, W. Greuell, E. Hanna, A. Payne, and I. Rutt (2007), Impact of model physics on estimating the surface mass balance of the Greenland ice sheet, *Geophysical Research Letters*, *34*, L17,501, doi:10.1029/2007GL030700.
- Box, J., X. Fettweis, J. Stroeve, M. Tedesco, D. Hall, and K. Steffen (2012a), Greenland ice sheet albedo feedback: thermodynamics and atmospheric drivers, *The Cryosphere*, *6*(4), 821–839, doi:10.5194/tc-6-821-2012.
- Box, J., X. Fettweis, J. Stroeve, M. Tedesco, D. Hall, and K. Steffen (2012b), Greenland ice sheet albedo feedback: thermodynamics and atmospheric drivers, *The Cryosphere Discuss.*, *6*(1), 593–634, doi:10.5194/tcd-6-593-2012.
- Box, J., et al. (2013), Greenland ice sheet mass balance reconstruction. part i: net snow accumulation (1600–2009), *Journal of Climate*, *26*(11), 3919–3934, doi:10.1175/JCLI-D-12-00373.1.
- Bromwich, D., Y. Du, and K. Hines (1996), Wintertime surface winds over the Greenland ice sheet, *Monthly Weather Review*, *124*(9), 1941–1947.

## Bibliography

---

- Brümmer, B., G. Müller, B. Affeld, R. Gerdes, M. Karcher, and F. Kauker (2001), Cyclones over Fram Strait: impact on sea ice and variability, *Polar Research*, 20(2), 147–152.
- Brümmer, B., G. Müller, and H. Hoerber (2003), A Fram Strait cyclone: Properties and impact on ice drift as measured by aircraft and buoys, *Journal of Geophysical Research*, 108, D7, 4217, doi:10.1029/2002JD002638.
- Brun, E., E. Martin, V. Simon, and C. Gendre (1989), An energy and mass model of snow cover suitable for operational avalanche forecasting, *Journal of Glaciology*, 35(121), 333–342.
- Cassano, J., J. Box, D. Bromwich, L. Li, and K. Steffen (2001), Evaluation of Polar MM5 simulations of Greenland's atmospheric circulation, *Journal of Geophysical Research*, 106(D24), 33,867.
- Catania, G., and T. Neumann (2010), Persistent englacial drainage features in the Greenland ice sheet, *Geophysical Research Letters*, 320, 778, doi:10.1126/science.1153360.
- Chen, J., C. Wilson, and B. Tapley (2013), Contribution of ice sheet and mountain glacier melt to recent sea level rise, *Nature Geoscience*, 6(6), 1–4, doi:10.1038/ngeo1829.
- Cheng, M., and B. Tapley (2004), Variations in the Earth's oblateness during the past 28 years, *Journal of Geophysical Research: Solid Earth*, 109, B09,402, doi:10.1029/2004JB003028.
- Chylek, P., C. Folland, G. Lesins, M. Dubey, et al. (2009), Arctic air temperature change amplification and the Atlantic Multidecadal Oscillation, *Geophysical Research Letters*, 36, L14,801, doi:10.1029/2009GL038777.
- Coléou, C., and B. Lesaffre (1998), Irreducible water saturation in snow: experimental results in a cold laboratory, *Annals of Glaciology*, 26, 64–68.
- Comiso, J. (2006), Abrupt decline in the Arctic winter sea ice cover, *Geophysical Research Letters*, 33, L18,504, doi:10.1029/2006GL027341.
- Comiso, J. (2012), Large decadal decline of the Arctic multiyear ice cover, *Journal of Climate*, 25(4), 1176–1193, doi:10.1175/JCLI-D-11-00113.1.
- Comiso, J., C. Parkinson, R. Gersten, and L. Stock (2008), Accelerated decline in the Arctic sea ice cover, *Geophysical Research Letters*, 35(1), L01,703, doi:10.1029/2007GL031972.
- Davis, C. (2005), Snowfall-driven growth in East Antarctic ice sheet mitigates recent sea-level rise, *Science*, 308(5730), 1898–1901, doi:10.1126/science.1110662.
- Dickson, B., I. Yashayaev, J. Meincke, B. Turrell, S. Dye, et al. (2002), Rapid freshening of the deep North Atlantic Ocean over the past four decades, *Nature*, 416, 832–837.
- Doyle, J., and M. Shapiro (1999), Flow response to large-scale topography: the Greenland tip jet, *Tellus A*, 51(5), 728–748.
- Ettema, J., M. van den Broeke, E. van Meijgaard, W. van de Berg, J. Bamber, J. Box, and R. Bales (2009), Higher surface mass balance of the Greenland ice sheet revealed by high-resolution climate modeling, *Geophysical Research Letters*, 36, L12,501, doi:10.1029/2009GL038110.
- Ettema, J., M. van den Broeke, E. van Meijgaard, and W. van de Berg (2010a), Climate of the Greenland ice sheet using a high-resolution climate model, part 1: Evaluation, *The Cryosphere*, 4, 561–602.
- Ettema, J., M. van den Broeke, E. van Meijgaard, and W. van de Berg (2010b), Climate of the Greenland ice sheet using a high-resolution climate model, part 2: Near-surface climate and energy balance, *The Cryosphere*, 4, 603–639.
- Fettweis, X., E. Hanna, H. Gallée, P. Huybrechts, et al. (2008), Estimation of the Greenland ice sheet surface mass balance for the 20th and 21st centuries, *The Cryosphere*, 2, 117–129.
- Fettweis, X., M. Tedesco, M. van den Broeke, and J. Ettema (2011), Melting trends over the Greenland ice sheet (1958–2009) from spaceborne microwave data and regional climate models, *The Cryosphere*, 5, 359–375, doi:10.5194/tc-5-359-2011.
- Fettweis, X., B. Franco, M. Tedesco, J. van Angelen, J. Lenaerts, M. van den Broeke, and H. Gallée (2012a), Estimating Greenland ice sheet surface mass balance contribution to future sea level

- rise using the regional atmospheric climate model MAR, *The Cryosphere*, 6(4), 3101–3147, doi:10.5194/tc-6-3101-2012.
- Fettweis, X., E. Hanna, C. Lang, A. Belleflamme, M. Erpicum, and H. Gallée (2012b), Important role of the mid-tropospheric atmospheric circulation in the recent surface melt increase over the Greenland ice sheet, *The Cryosphere*, 7, 241–248, doi:10.5194/tc-7-241-2013.
- Fitzgerald, P., J. Bamber, J. Ridley, and J. Rougier (2012), Exploration of parametric uncertainty in a surface mass balance model applied to the Greenland ice sheet, *Journal of Geophysical Research*, 117(F1), F01,021, doi:10.1029/2011JF002067.
- Flanner, M., and C. Zender (2006), Linking snowpack microphysics and albedo evolution, *Journal of Geophysical Research*, 111(D12), D12,208, doi:10.1029/2005JD006834.
- Flanner, M., C. Zender, J. Randerson, and P. Rasch (2007), Present-day climate forcing and response from black carbon in snow, *Journal of Geophysical Research*, 112, D11,202, doi:10.1029/2006JD008003.
- Flanner, M., K. Shell, M. Barlage, D. Perovich, and M. Tschudi (2011), Radiative forcing and albedo feedback from the northern hemisphere cryosphere between 1979 and 2008, *Nature Geoscience*, 4(3), 151, doi:10.1038/ngeo1062.
- Forster, R. R., et al. (2013), Perennial liquid water discovered in Greenland firn layer, *Nature Geoscience*, in review.
- Francis, J., and E. Hunter (2007), Changes in the fabric of the Arctic's greenhouse blanket, *Environmental Research Letters*, 2, 045,011, doi:10.1088/1748-9326/2/4/045011.
- Gardner, A., and M. Sharp (2010), A review of snow and ice albedo and the development of a new physically based broadband albedo parameterization, *Journal of Geophysical Research*, 115, F01,009, doi:10.1029/2009JF001444.
- Goelzer, H., P. Huybrechts, S. Raper, M. Loutre, H. Goosse, and T. Fichefet (2012), Millennial total sea-level commitments projected with the earth system model of intermediate complexity LOVECLIM, *Environmental Research Letters*, 7(4), 045,401, doi:10.1088/1748-9326/7/4/045401.
- Graversen, R., T. Mauritsen, M. Tjernström, E. Källén, et al. (2008), Vertical structure of recent Arctic warming, *Nature*, 451, 53–56, doi:10.1038/nature06502.
- Grenfell, T., S. Warren, and P. Mullen (1994), Reflection of solar radiation by the Antarctic snow surface at ultraviolet, visible and near-infrared wavelengths, *Journal of Geophysical Research*, 99(D9), 18,669–18,684, doi:10.1029/94JD01484.
- Greuell, W., and T. Konzmann (1994), Numerical modeling of the energy balance and the englacial temperature of the Greenland ice sheet. calculations for the ETH-Camp location (west Greenland, 1155 m a.s.l.), *Global and Planetary Change*, 9, 91–114, doi:10.1016/0921-8181(94)90010-8.
- Hanna, E., P. Huybrechts, and K. Steffen (2008), Increased runoff from melt from the Greenland ice sheet: a response to global warming, *Journal of Climate*, 21, 331–341, doi:10.1175/2007JCLI1964.1.
- Hanna, E., et al. (2013), Ice-sheet mass balance and climate change, *Nature*, 498(7452), 51–59, doi:10.1038/nature12238.
- Hansen, J., and L. Nazarenko (2004), Soot climate forcing via snow and ice albedos, *Proceedings of the National Academy of Sciences USA*, 101(2), 423–428, doi:10.1073/pnas.2237157100.
- Harper, J., N. Humphrey, W. Pfeffer, J. Brown, and X. Fettweis (2012), Greenland ice-sheet contribution to sea-level rise buffered by meltwater storage in firn, *Nature*, 491(7423), 240–243, doi:10.1038/nature11566.
- Hatun, H. (2005), Influence of the Atlantic subpolar gyre on the thermohaline circulation, *Science*, 309(5742), 1841–1844, doi:10.1126/science.1114777.
- Heinemann, G. (1999), The KABEG-97 field experiment: An aircraft-based study of katabatic wind dynamics over the Greenland ice sheet, *Boundary-Layer Meteorology*, 93(1), 75–116.
- Heinemann, G., and T. Klein (2002), Modelling and observations of the katabatic flow dynamics over

## Bibliography

---

- Greenland, *Tellus A*, 54(5), 542–554.
- Hilmer, M., M. Harder, and P. Lemke (1998), Sea ice transport: a highly variable link between Arctic and North Atlantic, *Geophysical Research Letters*, 25, 3359–3362, doi:10.1029/98GL52360.
- Hurrell, J., Y. Kushnir, G. Ottersen, and M. Visbeck (2003), An overview of the North Atlantic Oscillation, *Geophysical Monograph Series*, 134, 279, doi:10.1029/GM134.
- Johannessen, O., et al. (2004), Arctic climate change: observed and modelled temperature and sea ice variability, *Tellus A*, 56, 328–341, doi:10.1111/j.1600-0870.2004.00060.
- Jones, C., et al. (2011), The HadGEM2-ES implementation of CMIP5 centennial simulations, *Geoscience Model Development*, 4(3), 543–570, doi:10.5194/gmd-4-543-2011.
- Joughin, I., and D. Winebrenner (1995), Observations of ice sheet motion in Greenland using satellite radar interferometry, *Geophysical Research Letters*, 22(5), 571–574, doi:10.1029/95GL00264.
- Jung, T., and M. Hilmer (2001), The link between the North Atlantic Oscillation and Arctic sea ice export through Fram Strait, *Journal of Climate*, 14, 3932–3943, doi:10.1175/1520-0442(2001)014.
- Kjeldsen, K., et al. (2012), Improved ice loss estimate of the northwestern Greenland ice sheet, *Journal of Geophysical Research*, 118, 698–708, doi:10.1029/2012JB009684.
- Klein, T., and G. Heinemann (2002), Interaction of katabatic winds and mesocyclones near the eastern coast of Greenland, *Meteorological Applications*, 9(4), 407–422.
- Koenigk, T., U. Mikolajewicz, H. Haak, and J. Jungclaus (2006), Variability of Fram Strait sea ice export: causes, impacts and feedbacks in a coupled climate model, *Climate dynamics*, 26, 17–34, doi:10.1007/s00382-005-0060-1.
- Kuipers Munneke, P., M. van den Broeke, J. Lenaerts, M. Flanner, A. Gardner, and W. van de Berg (2011), A new albedo parameterization for use in climate models over the Antarctic ice sheet, *Journal of Geophysical Research*, 116, D05,114, doi:10.1029/2010JD015113.
- Kurtz, N., T. Markus, S. Farrell, D. Worthen, and L. Boisvert (2011), Observations of recent Arctic sea ice volume loss and its impact on ocean-atmosphere energy exchange and ice production, *Journal of Geophysical Research*, 116(C4), C04,015, doi:10.1029/2010JC006235.
- Kwok, R. (2009), Outflow of Arctic ocean sea ice into the Greenland and Barents Seas: 1979–2007, *Journal of Climate*, 22, 2438–2457, doi:10.1175/2008JCLI2819.1.
- Kwok, R., and G. Cunningham (2010), Contribution of melt in the Beaufort Sea to the decline in Arctic multiyear sea ice coverage: 1993–2009, *Geophysical Research Letters*, 37, L20,501, doi:10.1029/2010GL044678.
- Kwok, R., and D. Rothrock (2009), Decline in Arctic sea ice thickness from submarine and ICESat records: 1958–2008, *Geophysical Research Letters*, 36, L15,501, doi:10.1029/2009GL039035.
- Kwok, R., G. Cunningham, and S. Pang (2004), Fram Strait sea ice outflow, *Journal of Geophysical Research*, 109, c09,009–c01,029.
- Kwok, R., G. Spreen, and S. Pang (2013), Arctic sea ice circulation and drift speed: Decadal trends and ocean currents, *Journal of Geophysical Research Oceans*, pp. n/a–n/a, doi:10.1002/jgrc.20191.
- Lemke, P., and M. Hilmer (1998), Simulation of sea ice transport through Fram Strait: Natural variability and sensitivity to forcing, *Journal of Geophysical Research*.
- Lenaerts, J., M. van den Broeke, S. Déry, G. König-langlo, J. Ettema, and P. Kuipers Munneke (2010), Modeling snowdrift sublimation on an Antarctic shelf, *The Cryosphere*, 4, 179–190, doi:10.5194/tc-4-179-2010.
- Lenaerts, J., M. van den Broeke, J. van Angelen, E. van Meijgaard, and S. Déry (2012a), Drifting snow climate of the Greenland ice sheet: a study with a regional climate model, *The Cryosphere*, 6(4), 891–899, doi:10.5194/tc-6-891-2012.
- Lenaerts, J., M. van den Broeke, S. Déry, E. van Meijgaard, W. van de Berg, S. Palm, and J. Sanz Rodrigo (2012b), Modeling drifting snow in Antarctica with a regional climate model: 1. methods and model



- evaluation, *Journal of Geophysical Research*, 117(D5), D05,108, doi:10.1029/2011JD016145.
- Lenaerts, J., J. van Angelen, M. van den Broeke, A. Gardner, B. Wouters, and E. van Meijgaard (2013), Irreversible mass loss of Canadian Arctic Archipelago glaciers, *Geophysical Research Letters*, 40, 1–5, doi:10.1002/grl.50214.
- Mahajan, S., R. Zhang, and T. Delworth (2011), Impact of the Atlantic Meridional Overturning Circulation (AMOC) on Arctic surface air temperature and sea ice variability, *Journal of Climate*, 24, 6573–6581, doi:10.1175/2011JCLI4002.1.
- Mahrt, L. (1982), Momentum balance of gravity flows., *Journal of Atmospheric Sciences*, 39, 2701–2711.
- Moon, T., I. Joughin, B. Smith, and I. Howat (2012), 21st-century evolution of Greenland outlet glacier velocities, *Science*, 336(6081), 576–578, doi:10.1126/science.1219985.
- Moore, G. (2003), Gale force winds over the Irminger Sea to the east of Cape Farewell, Greenland, *Geophysical Research Letters*, 30(17), 1894.
- Moore, G., and I. Renfrew (2005), Tip jets and barrier winds: A QuikSCAT climatology of high wind speed events around Greenland, *Journal of Climate*, 18(18), 3713–3725.
- Moss, R., et al. (2010), The next generation of scenarios for climate change research and assessment, *Nature*, 463(7282), 747–756, doi:10.1038/nature08823.
- Nghiem, S., D. Hall, T. Mote, M. Tedesco, M. Albert, K. Keegan, C. Shuman, N. DiGirolamo, and G. Neumann (2012), The extreme melt across the Greenland ice sheet in 2012, *Geophysical Research Letters*, 39, L20,502, doi:10.1029/2012GL053611.
- Nick, F., A. Vieli, I. Howat, and I. Joughin (2009), Large-scale changes in Greenland outlet glacier dynamics triggered at the terminus, *Nature Geoscience*, 2, 110–114, doi:DOI:10.1038/NGEO394.
- Overland, J., J. Francis, E. Hanna, and M. Wang (2012), The recent shift in early summer Arctic atmospheric circulation, *Geophysical Research Letters*, 39(19), L19,804, doi:10.1029/2012GL053268.
- Parkinson, C., and D. Cavalieri (2008), Arctic sea ice variability and trends, 1979–2006, *Journal of Geophysical Research*.
- Parkinson, C., and J. Comiso (2013), On the 2012 record low Arctic sea ice cover: Combined impact of preconditioning and an august storm, *Geophysical Research Letters*, 40(7), 1356–1361, doi:10.1002/grl.50349.
- Parry, V., P. Nienow, D. Mair, J. Scott, B. Hubbard, K. Steffen, and D. Wingham (2007), Investigations of meltwater refreezing and density variations in the snowpack and firn within the percolation zone of the Greenland ice sheet, *Annals of Glaciology*, 46, 61–68, doi:10.3189/172756407782871332.
- Petersen, G., J. Kristjansson, and H. Olafsson (2004), Numerical simulations of Greenland's impact on the northern hemisphere winter circulation, *Tellus A*, 56(2), 102–111.
- Petersen, G., I. Renfrew, and G. Moore (2009), An overview of barrier winds off southeastern Greenland during the Greenland flow distortion experiment, *Quarterly Journal of the Royal Meteorological Society*, 135(645), 1950–1967.
- Pritchard, H., S. Ligtenberg, H. Fricker, D. Vaughan, M. van den Broeke, and L. Padman (2012), Antarctic ice-sheet loss driven by basal melting of ice shelves, *Nature*, 484(7395), 502–505, doi:10.1038/nature10968.
- Rahmstorf, S., and A. Ganopolski (1999), Long-term global warming scenarios computed with an efficient coupled climate model, *Climatic Change*, 43, 353–367.
- Reijmer, C., E. van Meijgaard, and M. van den Broeke (2004), Numerical studies with a regional atmospheric climate model based on changes in the roughness length for momentum and heat over Antarctica, *Boundary-Layer Meteorology*, 111(2), 313–337.
- Reijmer, C., M. van den Broeke, X. Fettweis, J. Ettema, and L. Stap (2012), Refreezing on the Greenland ice sheet: A comparison of parameterizations, *The Cryosphere*, 6(4), 743–762, doi:10.5194/tc-6-743-2012.

## Bibliography

---

- Renfrew, I., et al. (2008), The Greenland flow distortion experiment, *Bulletin of the American Meteorological Society*, 89(9), 1307–1324.
- Renfrew, I., G. Petersen, D. Sproson, G. Moore, H. Adiwidjaja, S. Zhang, and R. North (2009), A comparison of aircraft-based surface-layer observations over Denmark Strait and the Irminger Sea with meteorological analyses and QuikSCAT winds, *Quarterly Journal of the Royal Meteorological Society*, 135(645), 2046–2066.
- Rignot, E. (2006), Changes in the velocity structure of the Greenland ice sheet, *Science*, 311(5763), 986–990, doi:10.1126/science.1121381.
- Rignot, E., J. Box, E. Burgess, and E. Hanna (2008a), Mass balance of the Greenland ice sheet from 1958 to 2007, *Geophysical Research Letters*, 35(20), L20,502, doi:10.1029/2008GL035417.
- Rignot, E., J. Bamber, M. van den Broeke, C. Davis, Y. Li, W. van de Berg, and E. van Meijgaard (2008b), Recent Antarctic ice mass loss from radar interferometry and regional climate modelling, *Nature Geoscience*, 1(2), 106–110, doi:10.1038/ngeo102.
- Rignot, E., I. Velicogna, M. van den Broeke, A. Monaghan, and J. Lenaerts (2011), Acceleration of the contribution of the Greenland and Antarctic ice sheets to sea level rise, *Geophysical Research Letters*, 38(5), L05,503, doi:10.1029/2011GL046583.
- Rigor, I., J. Wallace, and R. Colony (2002), Response of sea ice to the Arctic Oscillation, *Journal of Climate*, 15, 2648–2663.
- Sasgen, I., M. van den Broeke, J. L. Bamber, E. Rignot, L. S. Sørensen, B. Wouters, Z. Martinec, I. Velicogna, and S. B. Simonsen (2012), Timing and origin of recent regional ice-mass loss in Greenland, *Earth and Planetary Science Letters*, 333–334(C), 293–303, doi:10.1016/j.epsl.2012.03.033.
- Schrama, E., B. Wouters, and B. Vermeersen (2011), Present day regional mass loss of Greenland observed with satellite gravimetry, *Surveys in Geophysics*, doi:10.1038/NGEO938.
- Scorer, R. (1988), Sunny Greenland, *Quarterly Journal of the Royal Meteorological Society*, 114(479), 3–29.
- Screen, J., and I. Simmonds (2010), The central role of diminishing sea ice in recent Arctic temperature amplification, *Nature*, 464, 1334–1337, doi:10.1038/nature09051.
- Shepherd, A., E. Ivins, et al. (2012), A reconciled estimate of ice-sheet mass balance, *Science*, 338(6111), 1183–1189, doi:10.1126/science.1228102.
- Simmons, A., S. Uppala, D. Dee, and S. K. (2007) (2007), ERA-Interim: New ECMWF reanalysis products from 1989 onwards, *ECMWF Newsletter*, 110, 29–35.
- Soja, A., N. Tchebakova, N. French, et al. (2007), Climate-induced boreal forest change: predictions versus current observations, *Global and Planetary Change*, 56, 274–296, doi:10.1016/j.gloplacha.2006.07.028.
- Steele, M., W. Ermold, and J. Zhang (2008), Arctic ocean surface warming trends over the past 100 years, *Geophysical Research Letters*, 35, L02,614, doi:10.1029/2007GL031651.
- Steffen, K., and J. Box (2001), Surface climatology of the Greenland ice sheet: Greenland climate network 1995–1999, *Journal of Geophysical Research*, 106(D24), 33,951.
- Stroeve, J. (2007), Assessment of Greenland albedo variability from the advanced very high resolution radiometer polar pathfinder data set, *Journal of Geophysical Research*, 106(D24), 33,989–34,006, doi:10.1029/2001JD900072.
- Stroeve, J., J. Box, F. Gao, S. Liang, A. Nolin, and C. Schaaf (2005), Accuracy assessment of the modis 16-day albedo product for snow: comparisons with Greenland in situ measurements, *Remote sensing of environment*, 94, 46–60, doi:10.1016/j.rse.2004.09.001.
- Stroeve, J., M. Holland, and W. Meier (2007), Arctic sea ice decline: Faster than forecast, *Geophysical Research Letters*, 34, L09,501, doi:10.1029/2007GL029703.
- Stroeve, J., V. Kattsov, A. Barrett, et al. (2012), Trends in Arctic sea ice extent from CMIP5, CMIP3 and

- observations, *Geophysical Research Letters*, 39, L16,502, doi:10.1029/2012GL052676.
- Swenson, S., D. Chambers, and J. Wahr (2008), Estimating geocenter variations from a combination of GRACE and ocean model output, *Journal of Geophysical Research: Solid Earth*, 113, B08,410, doi: 10.1029/2007JB005338.
- Tapley, B., S. Bettadpur, M. Watkins, and C. Reigber (2004), The gravity recovery and climate experiment: Mission overview and early results, *Geophysical Research Letters*, 31, L09,607, doi: 10.1029/2004GL019920.
- Taylor, K., R. Stouffer, and G. Meehl (2007), A summary of the CMIP5 experiment design, *World*, 4, 1–33.
- Tedesco, M., X. Fettweis, M. van den Broeke, R. van de Wal, C. Smeets, W. van de Berg, M. Serreze, and J. Box (2011), The role of albedo and accumulation in the 2010 melting record in Greenland, *Environmental Research Letters*, 6, 014,005, doi:doi:10.1088/1748-9326/6/1/014005.
- Tedesco, M., X. Fettweis, T. Mote, J. Wahr, P. Alexander, J. Box, and B. Wouters (2013), Evidence and analysis of 2012 Greenland records from spaceborne observations, a regional climate model and reanalysis data, *The Cryosphere*, 7, 615–630, doi:10.5194/tc-7-615-2013.
- Thompson, D., and J. Wallace (1998), The Arctic Oscillation signature in the wintertime geopotential height and temperature fields, *Geophysical Research Letters*, 25, 1297–1300.
- Tsukernik, M., D. Kindig, and M. Serreze (2007), Characteristics of winter cyclone activity in the northern North Atlantic: Insights from observations and regional modeling, *Journal of Geophysical Research*, 112(D3), D03,101, doi:10.1029/2006JD007184.
- Tsukernik, M., C. Deser, M. Alexander, and R. Tomas (2009), Atmospheric forcing of Fram Strait sea ice export: a closer look, *Climate Dynamics*, 35, 1349–1360, doi:10.1007/s00382-009-0647.
- Uden, P., L. Rontu, H. Järvinen, P. Lynch, J. Calvo, G. Cats, J. Cuhart, K. Eerola, et al. (2002), *HIRLAM-5 Scientific Documentation: December 2002, Tech. rep.*, Swed. Meteorol. and Hydrol. Inst, Norrköpping, Sweden.
- Uppala, S., P. Kållberg, et al. (2005), The ERA-40 re-analysis, *Quarterly Journal of the Royal Meteorological Society*, 131(612), 2961–3012, doi:10.1256/qj.04.176.
- Vage, K., T. Spengler, H. Davies, and R. Pickart (2009), Multi-event analysis of the westerly Greenland tip jet based upon 45 winters in ERA-40, *Quarterly Journal of the Royal Meteorological Society*, 135(645), 1999–2011.
- Van Angelen, J., M. van den Broeke, and W. van de Berg (2011a), Momentum budget of the atmospheric boundary layer over the Greenland ice sheet and its surrounding seas, *Journal of Geophysical Research*, 116, D10,101, doi:10.1029/2010JD015485.
- Van Angelen, J., M. van den Broeke, and R. Kwok (2011b), The Greenland sea jet: A mechanism for wind-driven sea ice export through Fram Strait, *Geophysical Research Letters*, 38, L12,805, doi:doi: 10.1029/2011GL047837.
- Van Angelen, J., J. Lenaerts, S. Lhermitte, X. Fettweis, P. Kuipers Munneke, M. van den Broeke, E. van Meijgaard, and C. Smeets (2012), Sensitivity of Greenland ice sheet surface mass balance to surface albedo parameterization: a study with a regional climate model, *The Cryosphere*, 6(5), 1175–1186, doi:10.5194/tc-6-1175-2012.
- Van Angelen, J., J. Lenaerts, B. Wouters, and M. van den Broeke (2013), Contemporary (1960–2012) evolution of the climate and surface mass balance of the Greenland ice sheet, *Surveys in Geophysics*, pp. 1175–1186.
- Van de Berg, W., M. van den Broeke, C. Reijmer, and E. van Meijgaard (2006), Reassessment of the Antarctic surface mass balance using calibrated output of a regional atmospheric climate model, *Journal of Geophysical Research*, 111, 90–180.
- Van de Berg, W., M. van den Broeke, and E. van Meijgaard (2008), Spatial structures in the heat budget of the Antarctic atmospheric boundary layer, *The Cryosphere*, 2, 1–12.

## Bibliography

---

- Van de Wal, R., W. Greuell, M. van den Broeke, C. Reijmer, and J. Oerlemans (2005), Surface mass-balance observations and automatic weather station data along a transect near Kangerlussuaq, west Greenland, *Annals of Glaciology*, 42(1), 311–316, doi:10.3189/172756405781812529.
- Van de Wal, R., W. Boot, C. Smeets, H. Snellen, M. van den Broeke, and J. Oerlemans (2012), Twenty-one years of mass balance observations along the k-transect, west Greenland, *Earth System Science Data*, 4, 31–35, doi:10.5194/essd-4-31-2012.
- Van den Broeke, M., and H. Gallée (1996), Observation and simulation of barrier winds at the western margin of the Greenland ice sheet, *Quarterly Journal of the Royal Meteorological Society*, 122(534), 1365–1383.
- Van den Broeke, M., and N. van Lipzig (2003), Factors controlling the near-surface wind field in Antarctica, *Monthly Weather Review*, 131, 733–743.
- Van den Broeke, M., P. Duynkerke, and J. Oerlemans (1994), The observed katabatic flow at the edge of the Greenland ice sheet during GIMEX-91, *Global and Planetary Change*, 9(1-2), 3–15.
- Van den Broeke, M., N. van Lipzig, and E. van Meijgaard (2002), Momentum budget of the East Antarctic-atmospheric boundary layer: results of a regional climate model, *Journal of the Atmospheric Sciences*, 59, 3117–3129.
- Van den Broeke, M., C. Smeets, J. Ettema, et al. (2008a), Partitioning of melt energy and meltwater fluxes in the ablation zone of the west Greenland ice sheet, *The Cryosphere*, 2, 179–189.
- Van den Broeke, M., C. Smeets, J. Ettema, and P. Kuipers Munneke (2008b), Surface radiation balance in the ablation zone of the west Greenland ice sheet, *Journal of Geophysical Research*, 113, D13,105, doi:10.1029/2007JD009283.
- Van den Broeke, M., J. Bamber, J. Ettema, E. Rignot, E. Schrama, W. van de Berg, E. van Meijgaard, I. Velicogna, and B. Wouters (2009), Partitioning recent Greenland mass loss, *Science*, 326(5955), 984, doi:10.1126/science.1178176.
- Van den Broeke, M., J. Bamber, J. Lenaerts, and E. Rignot (2011), Ice sheets and sea level: Thinking outside the box, *Surveys in Geophysics*, pp. 1–11, doi:10.1007/s10712-011-9137-z.
- Van Meijgaard, E., L. van Uft, W. van de Berg, F. Bosveld, B. van den Hurk, G. Lenderink, and A. Siebesma (2008), *The KNMI regional atmospheric climate model RACMO version 2.1*, Tech. Rep. 302.
- Vinje, T. (2001), Fram Strait ice fluxes and atmospheric circulation: 1950–2000, *journals.ametsoc.org*.
- Wahr, J., S. Swenson, V. Zlotnicki, and I. Velicogna (2004), Time variable gravity from GRACE: First results, *Geophysical Research Letters*, 31, L11,501, doi:10.1029/2004GL019779.
- Warren, S., and A. Clarke (1990), Soot in the atmosphere and snow surface of Antarctica, *Journal of Geophysical Research*, 95(D2), 1811–1816, doi:10.1029/JD095iD02p01811.
- White, P. (2004), Ifs documentation cy23r4: Part iv physical processes.
- Wientjes, I., R. van de Wal, G. Reichert, A. Sluijs, and J. Oerlemans (2011), Dust from the dark region in the western ablation zone of the Greenland ice sheet, *The Cryosphere*, 5, 589–601, doi:10.5194/tc-5-589-2011.
- Wiscombe, W., and S. Warren (1980), A model for the spectral albedo of snow. i: Pure snow, *Journal of Atmospheric Sciences*, 37, 2712–2745.
- Wouters, B. (2010), Identification and modeling of sea level change contributors – On GRACE satellite gravity data and their application to climate monitoring, Ph.D. thesis, Delft University of Technology.
- Wouters, B., D. Chambers, and E. Schrama (2008), GRACE observes small-scale mass loss in Greenland, *Geophysical Research Letters*, 35, L20,501, doi:10.1029/2008GL034816.
- Wu, B., J. Wang, and J. Walsh (2006), Dipole anomaly in the winter Arctic atmosphere and its association with sea ice motion, *Journal of Climate*.
- Zwally, H., and L. Jun (2002), Seasonal and interannual variations of firn densification and ice

sheet surface elevation at Greenland summit, *Journal of Glaciology*, 48, 199—207, doi:10.3189/172756502781831403.

Zwally, H., et al. (2011), Greenland ice sheet mass balance: distribution of increased mass loss with climate warming; 2003-07 versus 1992-2002, *Journal of Glaciology*, 57(201), 88–102.



# Publications

---

## First author

- Van Angelen, J.H., M.R. van den Broeke and W.J. van de Berg (2011), Momentum Budget of the atmospheric boundary layer over the Greenland ice sheet and its surrounding seas, *Journal of Geophysical Research*, 115, D10101, doi:10.1029/2010JD015485. [Chapter 2]
- Van Angelen, J.H., M.R. van den Broeke and R. Kwok, The Greenland Sea Jet: A mechanism for wind-driven sea ice export through Fram Strait, *Geophysical Research Letters*, 38, L12805, doi:10.1029/2011GL047837. [Chapter 3]
- Van Angelen, J.H., J.T.M. Lenaerts, S. Lhermitte, X. Fettweis, P. Kuipers Munneke, M.R. van den Broeke and E. van Meijgaard: Sensitivity of Greenland ice sheet surface mass balance to surface albedo parameterization: a study with a regional climate model. *The Cryosphere*, 6, 1175-1186, doi:10.5194/tc-6-1175-2012. [Chapter 4]
- Van Angelen, J.H., J.T.M. Lenaerts, M.R. van den Broeke, X. Fettweis, and E. van Meijgaard, Rapid loss of firn pore space accelerates 21st century Greenland mass loss, *Geophysical Research Letters*., 40, doi:10.1002/grl.50490. [Chapter 6]
- Van Angelen, J.H., J.T.M. Lenaerts, M.R. van den Broeke and B. Wouters, Contemporary (1960-2012) evolution of the climate and surface mass balance of the Greenland ice sheet, *Surveys in Geophysics*, accepted. [Chapter 5]

## Co-author

- Van Pelt, W.J.J., J. Oerlemans, C.H. Reijmer, V.A. Pohjola, R. Pettersson and J.H. van Angelen, Simulating melt, runoff and refreezing on Nordenskjöldbreen Svalbard, using a coupled snow and energy balance model, *The Cryosphere*, 6, 641-659, doi:10.5194/tc-6-641-2012.
- Shepherd, A. and IMBIE participants: A reconciled estimate of ice sheet mass balance. *Science*, 338, 1183-1189, doi: 10.1126/science.1228102.
- Lenaerts, J.T.M., M.R. van den Broeke, J.H. van Angelen, E. van Meijgaard and S.J. Déry, Drifting snow climate of the Greenland ice sheet: a study with a regional

- climate model, *The Cryosphere*, 6, 891-899, doi:10.5194/tc-6-891-2012.
- Christoffersen, P., M. O'Leary, J.H. van Angelen and M.R. van den Broeke, Partitioning effects from ocean and atmosphere on the calving stability of Kangerdlugssuaq Glacier, East Greenland, *Annals of Glaciology*, 53, 249-256, doi:10.3189/2012AoG60A087.
- Howat, I.M., S. de la Pena, J.H. van Angelen, J. T. M. Lenaerts and M. R. van den Broeke, 2012: Brief Communication: Expansion of meltwater lakes on the Greenland ice sheet. *The Cryosphere*, 7, 201-204, doi:10.5194/tc-7-201-2013.
- Machguth, H., P. Rastner, T. Bolch, N. Mölg, L. Sandberg Sørensen, G. Aðalgeirsdóttir, J.H. van Angelen, M.R. van den Broeke and X Fettweis, *Environmental Research Letters* 8 025005, doi:10.1088/1748-9326/8/2/025005.
- Lenaerts, J.T.M., J.H. van Angelen, M.R. van den Broeke, A.S. Gardner, B. Wouters and E. van Meijgaard, 2013. Irreversible mass loss of Canadian Arctic Archipelago glaciers. *Geophysical Research Letters*, 40, doi:10.1002/grl.50214.
- Fettweis, X., B. Franco, M. Tedesco, J.H. van Angelen, J.T.M. Lenaerts, M.R. van den Broeke and H. Gallée, 2013. Estimating the Greenland ice sheet surface mass balance contribution to future sea level rise using the regional atmospheric climate model MAR. *The Cryosphere*, 7, 469-489, doi:10.5194/tc-7-469-2013.
- Kjeldsen, K.K., S.A. Khan, J. Wahr, N.J. Korsgaard, K.H. Kjær, A.A. Bjørk, R. Hurkmans, M.R. van den Broeke, J.L. Bamber, and J.H. van Angelen, 2013. Improved ice loss estimate of the northwestern Greenland ice sheet. *Journal of Geophysical Research* 118, doi:10.1029/2012JB009684.
- Box, J.E., N. Cressie, D.H. Bromwich, J. Jung, M.R. van den Broeke, J. H. van Angelen, R.R. Forster, C. Miège, E. Mosley-Thompson, B. Vinther and J.R. McConnell, Greenland Ice Sheet Mass Balance Reconstruction. Part I: Net Snow Accumulation (1600–2009). *Journal of Climate*, 26, 3919-3934, doi: 10.1175/JCLI-D-12-00373.1.
- Vizcaíno, M., W.H. Lipscomb, W.J. Sacks, J.H. van Angelen, B. Wouters and M.R. van den Broeke, Greenland Surface Mass Balance as Simulated by the Community Earth System Model. Part I: Model Evaluation and 1850-2005 Results, doi:10.1175/JCLI-D-12-00615.1
- Wahr, J., S.A. Khan, T. van Dam, L. Liu, J.H. van Angelen, M.R. van den Broeke, and C.M. Meertens, The use of GPS horizontals for loading studies, with applications to northern California and southeast Greenland, *Journal of Geophysical Research Solid Earth*, 118, 1795-1806, doi:10.1002/jgrb.50104.
- Sundal, A.V., A. Shepherd, M.r. van den Broeke, J.H. van Angelen, N. Gourmelen and J. Park, Controls on short-term variations in Greenland glacier dynamics, *Journal of Glaciology*, 59, 883-892, doi:10.3189/2013JoG13J019.



- Joughin, I., S.B. Das, G.E. Flowers, M.D. Behn, R.B. Alley, M.A. King, B.E. Smith, J. Bamber, M.R. van den Broeke and J.H. van Angelen, Influence of ice-sheet geometry and supraglacial lakes on seasonal ice-flow variability, *The Cryosphere*, 7, 1185-1192, doi:10.5194/tc-7-1185-2013.
- Gorter, W., J.H. van Angelen, J.T.M. Lenaerts and M.R. van den Broeke: Present-day Greenland ice sheet wind climate and future changes from regional climate modelling, *Climate Dynamics*, doi:10.1007/s00382-013-1861-2

### Submitted

- Forster, R.R., J.E. Box, M.R. van den Broeke, C. Miège, E.W. Burgess, J.H. van Angelen, J.T.M. Lenaerts, L.S. Koenig, J. Paden, C. Lewis, S.P. Gogineni, Carl Leuschen and J.R. McConnell, Perennial Liquid Water Discovered in Greenland Firn Layer.
- Van As, D., M.L. Andersen, D. Petersen, X. Fettweis, J.H. van Angelen, J.T.M. Lenaerts, M.R. van den Broeke, J.M. Lea, C.E. Bøggild, A.P. Ahlstrøm and K. Steffen, Increasing meltwater discharge from the Nuuk region of the Greenland ice sheet and implications for mass balance (1989-2012).
- Csatho, B.M., A.F. Schenk, G.S. Babonis, C.J. van der Veen, M.R. van den Broeke, J.H. van Angelen, S. Nagarajan, S. Rezvanbehbahani and S.B. Simonsen, Laser altimetry reveals complex pattern of Greenland ice sheet dynamics.
- Enderlin, E.M., I.M. Howat, J.H. van Angelen, M.R. van den Broeke, M. Noh and S. Jeong, An improved mass budget for the Greenland ice sheet.
- Seo, K., D.E. Waliser, C. Lee, B. Tian, T. Scambos, B. Kim, J.H. van Angelen and M.R. van den Broeke, Accelerated mass loss for the Greenland ice sheet: links to atmospheric circulation change in the Arctic.
- Haumann, F.A., J.H. van Angelen, J.T.M. Lenaerts and M.R. van den Broeke, Dynamical causes of recent Antarctic sea-ice changes.
- M.I. van Angelen, J.H. van Angelen en R.H. Zegers, Dreigende blindheid veroorzaakt door spelen op de saxofoon, *Nederlands Tijdschrift voor Geneeskunde*.



# Dankwoord

---

Promoveren is net een ontdekkingsreis, waarbij gedurende vier jaar via onverwachte en zeker niet de kortste routes naar de voltooiing van een proefschrift wordt gewerkt. Onderweg dienen de nodige tegenslagen verwerkt te worden, maar er zijn ook zeker successen te vieren. Dankzij de ondersteuning van collega's, vrienden en familie is mijn reis zeker geen eenzame zoektocht geweest. Mijn dank gaat allereerst uit naar mijn promotor Michiel van den Broeke, wiens enthousiasme en passie voor het vakgebied aanstekelijk is en een onuitputtelijke bron voor nieuwe inzichten vormt. Geweldig dat je deur altijd open staat en ik je 'even' kan storen om een figuur te laten zien waar we vervolgens een hele middag over konden filosoferen. Je hebt me veel vrijheid gegeven, maar stuurde me op de juiste momenten in de goede richting, hetgeen mij een betere onderzoeker gemaakt heeft. En dankzij de vele versies van mijn artikelen die je van rode inkt hebt voorzien is mijn schrijfstijl op een academisch waardig niveau gekomen. Maar niet alleen op wetenschappelijk, ook op sociaal gebied toonde je altijd je interesse en was je betrokken, hetgeen onze samenwerking zeker ten goede is gekomen.

Mijn dank gaat tevens uit naar Willem Jan van de Berg (co-promotor) en Janneke Ettema. Dankzij jullie kennis, vaardigheden, ideeën en behulpzaamheid ben ik snel wegwijs geraakt met RACMO. Met name jullie vele handige scriptjes hebben mij enorm geholpen gedurende mijn hele traject.

Aan het begin van dit millennium was er het eerste contact met het IMAU. Onder supervisie van Huib de Swart, één van de meest inspirerende docenten, heb ik een natuurkunde project in de krochten van het BBL uitgevoerd. De afgelopen jaren heb ik met hem mogen samenwerken bij de colleges geofysische stromingsleer.

Mijn ontdekkingsreis heeft me langs internationale conferenties in Wenen, Boston, Fairbanks, San Francisco en Davos gevoerd, maar het veldwerk naar Groenland heeft de diepste indruk achtergelaten. Daadwerkelijk ervaren hoe immens de ijskap is en met eigen ogen te mogen aanschouwen wat er in een zomer kan wegsmelten. Henk Snellen, dank voor je aangename gezelschap, goede samenwerking en mooie verhalen die je met mij gedeeld hebt onder het genot van een muskusos-pizza op deze onvergetelijke trip.

Jan ‘De Belg’ Lenaerts, als collega en kamergenoot heb ik op wetenschappelijk gebied uitstekend met je kunnen samenwerken. Daarnaast ben ik je dankbaar voor je aangename gezelschap op de al-dan-niet werk gerelateerde uitstapjes naar de Lakanuki, de Galgenwaard, Rotliechtli, de Swetser en de Vessel. Ik hoop dat we veelvuldig kunnen blijven strijden op de flanken van de Ruiterberg, de Flüelapas of de Triple Mur de Monty.

Roderic Bosboom, na onze reizen door Australië en Zuid-Amerika hebben we ook deze reis samen mogen doorlopen. Dank voor de mooie verhalen die we uitgewisseld hebben en de goede gesprekken die we onder het genot van een lekker biertje op het Ledig Erf gehad hebben en nog vaak mogen hebben.

Ward van Pelt, een belangrijke basis van mijn proefschrift is gelegd tijdens onze NFS en UT inspireersessies op kamer 662. Michiel, Paul, Stefan, Aimée, Malou, Bas, Melchior, Lennert, Abdel en alle andere IMAU-collega’s, dank voor de vele gezellige HOEMBA-vergaderingen, werkbesprekingen, koffiepauzes, fietstochten, lunchwandelingen en vrijdagmiddagborrels. Ward en Alex, het was voor mij een waar genoegen om jullie te mogen begeleiden met jullie afstudeerproject. Wanda, Yvonne en Sandra, dank dat ik altijd binnen kon lopen voor een praatje en dat jullie ervoor gezorgd hebben dat ik netjes de bureaucratische paden bij het promoveren gevolgd heb.

De vrijheid van het promoveren en met name de flexibele werkuren stelden mij in de gelegenheid om op alle mogelijke tijdstippen te tennissen, te fietsen, een elfstedentocht te rijden, een spelletjesavond te doen of op vakantie te gaan. Rens, als geen ander kan ik met jou de belangrijkste zaken van het leven evalueren. Merijn en Tim, er komt een dag dat ik jullie versla op de Amerongse Berg. Jesper, heerlijk om toch nog even een keer die laatste te nemen. Folkert en Thomas, dat er nog vele boeruh-aangelegenheden mogen volgen. Ties, Ted, Aron en Frits, dank voor de gezellige avonden en jullie voorwerk in LaTeX.

Ik ben tennisvereniging Meijenhagen dankbaar voor de kans die ik gekregen heb om als voorzitter mijn persoonlijke vaardigheden op andere vlakken te ontwikkelen. In het bijzonder wil ik mijn bestuursgenoten Hans Erik, Gert, Geertjan, Karin, Ilse en Henk danken voor hetgeen zij mij op organisatorisch en bestuurlijk gebied hebben bijgebracht en voor de inspirerende en leuke vergaderingen. Els, Eelco, Laura, Joris en Rianne, het is elk jaar weer een groot plezier om samen met jullie van het open jeugdtoernooi de gezelligste week van het jaar op Meijenhagen te maken. Michiel, dank voor onze uitstekende samenwerking op en naast de baan. Sjoerd, Jolanda, Henriëtte, Lars, Frauke en alle andere Meijenhagers: bedankt voor de leuke trainingen, spannende wedstrijden, fantastische feestjes en mooie competitiezondagen. Anne, dank voor je emotionele en redigerende ondersteuning bij de laatste loodjes van mijn

boekje.

Dit proefschrift had er ook niet gelegen zonder mijn naaste familie. Annelies, Hans en Myrthe, dank voor jullie interesse in mijn werk. Martine, wat is het fijn om in dezelfde straat als je kleine zusje te wonen. Als personal shopping coach zorg je ervoor dat ik er bij alle officiële en minder officiële gelegenheden fatsoenlijk bij loop. Lieve Cor en Albi, ik ben jullie eeuwig dankbaar voor de onvoorwaardelijke steun bij alles wat ik doe en de keuzes die ik maak. Zonder jullie was ik nooit zo ver gekomen.



# Curriculum vitae

---

Jan van Angelen was born on May 15th, 1983 in Utrecht. His fascination for meteorology originates from a young age, especially for winter weather and ice skating opportunities. After he finished his pre-university education (VWO) at St. Bonifatius College, Utrecht in 2001, he packed his backpack and roamed around Australia and New Zealand for half a year. Refueled, he started a bachelor in physics at Utrecht University, which he almost completed after three years of hard working. Still restless to explore the world, he dusted off his backpack for another adventure in South America. Back in Utrecht, he finished his bachelors and meanwhile started the master Meteorology, Physical Oceanography and Climate, which he successfully completed in 2009, with a thesis on the impact of melt on the surface albedo of Antarctica. For his masters program, he attended some courses at the School of Meteorology at the University of Oklahoma, which he combined with several storm chasing adventures. Graduated, he got the opportunity from Michiel van den Broeke to pursue a PhD at the Institute for Marine and Atmospheric research in Utrecht (IMAU), with this thesis as final result.

